

# **Deformable Image Registration in the Analysis of Multiple Sclerosis**

by

Min Chen

A dissertation submitted to The Johns Hopkins University in conformity with the requirements for the degree of Doctor of Philosophy.

Baltimore, Maryland

January, 2015

© Min Chen 2015

All rights reserved

# Abstract

In medical image analysis, image registration is the task of finding corresponding features in two or more images, and using them to solve for the transformation that best aligns the images. Knowing the alignment allows information, such as landmarks and functional metrics, to be easily transferred between images, and allows them to be analyzed together.

This dissertation focuses on the development of deformable image registration techniques for the analysis of multiple sclerosis (MS), a neurodegenerative disease that damages the myelin sheath of nervous tissue. MS is known to affect the entire central nervous system (CNS), and can result in the loss of sensorimotor control, cognition, and vision. Hence, the four primary contributions of this dissertation are on the development and application of deformable image registration in the three areas of the CNS that are most currently studied for MS – the spinal cord, the retina, and the brain.

First, for spinal cord magnetic resonance imaging (MRI), an approach is presented that uses deformable registration to provide atlas priors for automatic topology-preserving segmentation of the spinal cord and cerebrospinal fluid. The method shows high accuracy and robustness when compared to manual raters, and allows spinal cord atrophy to be analyzed on large datasets without manual segmentations. Second, for spinal cord diffusion tensor imaging, a pipeline is presented that uses deformable registration to correct for susceptibility distortions in the images. The pipeline allows for accurate computation of spinal cord diffusion metrics, which are shown to be significantly correlated with clinical measures of sensorimotor function and disability levels. Third, for optical coherence tomography (OCT) of the retina, a deformable registration technique is presented that constrains the transformation to follow the OCT acquisition

geometry. 3D voxel-based analysis using the algorithm found significant differences between healthy and MS cohorts in regions of the retina that is consistent with previous findings using 2D analysis. Lastly, for brain MRI, a multi-channel registration framework is presented that can use distance transforms and image synthesis to improve registration accuracy. Together, these techniques have enabled several types of analysis that were previously unavailable for the study of MS.

**Dissertation Committee:**

Dr. Jerry L. Prince (Advisor)

Dr. Trac D. Tran (Second Reader)

Dr. Gerard G. L. Meyer

Dr. Daniel S. Reich

# Acknowledgements

I would like to thank my advisor, Dr. Jerry Prince, for guiding and mentoring me the past 6 years. In many ways he has transformed the way I think about and approach different problems. I have learned many lessons from him that I hope to carry forward with me in life.

I would like to thank Dr. Trac Tran, Dr. Gerard Meyer, and Dr. Daniel Reich for being part of my dissertation committee and reviewing my dissertation. In particular, I would like to thank Dr. Reich for his support and guidance over the years. From him I have learned how to see my work from a clinical perspective, which has provided the direction and motivation for much of my work. I would also like to thank the many colleagues and collaborators that I have had the pleasure of working with during my time at JHU. I have benefited tremendously from their knowledge and expertise. In particular, I would like to thank Dr. Dzung Pham, Dr. Pierre-Louis Bazin, and Dr. Jiwon Oh, for their feedback and assistance on the work presented in this dissertation.

I would like to thank those in my lab, especially Aaron Carass, John Bogovic, Andrew Lang, Amod Jog, for being great friends and being constantly willing to listen and suggest ideas whenever I am stuck on a problem. I would particularly like to thank Aaron, who's friendship and advice have helped me greatly during my time as a student, both inside and outside of the lab.

Lastly, I would like to thank my family and friends for their constant support, and their uncanny ability to know when I need a break from the work. I owe them much of my sanity. Most importantly, I would like to thank my parents, Dong Chen and Ninglin Yin, for their unyielding support and belief in my abilities. It is hard to imagine where I would be today without their guidance.

# Contents

<b>Abstract</b>	<b>ii</b>
<b>Acknowledgements</b>	<b>iv</b>
<b>Abbreviations and Symbols</b>	<b>viii</b>
<b>List of Figures</b>	<b>ix</b>
<b>List of Tables</b>	<b>xii</b>
<b>1 Introduction</b>	<b>1</b>
1.1 Image Registration and Multiple Sclerosis . . . . .	1
1.2 Dissertation Overview . . . . .	3
1.2.1 Contributions . . . . .	3
1.2.2 Organization . . . . .	5
<b>2 Background</b>	<b>7</b>
2.1 Introduction . . . . .	7
2.2 Basics of Image Registration . . . . .	7
2.2.1 Registration as a Minimization Problem . . . . .	8
2.2.2 Types of Registration . . . . .	9
2.2.2.1 Types of Transformation Models . . . . .	9
2.2.2.2 Types of Cost Functions . . . . .	11
2.3 Deformable Registration Algorithms Used In This Work . . . . .	14
2.3.1 ABA . . . . .	14
2.3.2 SyN . . . . .	15
2.4 Multiple Sclerosis . . . . .	17
2.4.1 Significance . . . . .	17
2.4.2 Challenges . . . . .	17
<b>3 Segmentation of Spinal Cord MRI Using Deformable Initializations</b>	<b>19</b>
3.1 Introduction . . . . .	19
3.2 Methods . . . . .	23
3.2.1 TOADS Overview . . . . .	24
3.2.2 Extending TOADS for the Spinal Cord . . . . .	25
3.2.3 Spinal Cord Topology and Statistical Atlases . . . . .	25
3.2.4 Incorporating Deformable Registration Into TOADS . . . . .	27
3.2.5 Topology Preserving Atlas Deformation . . . . .	27
3.2.6 Automated Atlas Construction . . . . .	29
3.3 Materials . . . . .	31

3.3.1	T1 Cohort . . . . .	31
3.3.2	MT Cohort . . . . .	31
3.3.3	Manual Segmentations . . . . .	32
3.3.4	Metrics . . . . .	32
3.4	Experimental Results . . . . .	33
3.4.1	Segmentation Comparison Against Manual Raters . . . . .	33
3.4.2	Statistical Atlas Construction Parameters . . . . .	33
3.4.3	Robustness in Large Scale Processing . . . . .	36
3.4.4	Clinical Relevance . . . . .	37
3.4.5	Exploratory Study of CSF Volumes . . . . .	39
3.5	Discussion . . . . .	39
3.5.1	Accuracy and Robustness . . . . .	41
3.5.2	Results Comparison Against Existing Literature . . . . .	42
3.5.3	Adapting to New Data . . . . .	43
3.6	Summary . . . . .	43
<b>4</b>	<b>Spinal Cord DTI Pipeline With Distortion Correction</b>	<b>45</b>
4.1	Introduction . . . . .	45
4.2	Methods . . . . .	46
4.2.1	Adapting CATNAP for the Spinal Cord . . . . .	46
4.2.2	Correcting EPI Susceptibility Distortions Using Constrained ABA . . . . .	47
4.2.3	Automatic Field of View Matching . . . . .	48
4.3	Quality Assurance . . . . .	48
4.4	Clinical Relevance . . . . .	49
4.5	Summary . . . . .	51
<b>5</b>	<b>Deformable Registration in Retinal OCT</b>	<b>53</b>
5.1	Introduction to Retinal Optical Coherence Tomography . . . . .	53
5.2	Methods . . . . .	57
5.2.1	Initial Preprocessing . . . . .	57
5.2.2	Image Registration Method . . . . .	58
5.2.3	Constructing A Normalized Space Using Deformable Registration . . . . .	63
5.2.4	Regional Analysis of Volumes Examined in Normalized Space . . . . .	63
5.3	Materials . . . . .	64
5.3.1	Data . . . . .	64
5.4	Registration Validation . . . . .	65
5.5	Applications . . . . .	66
5.5.1	Average Atlas and Normalized Space . . . . .	66
5.5.2	Statistical Atlas . . . . .	67
5.5.3	RAVENS Analysis of Multiple Sclerosis . . . . .	67
5.6	Discussion . . . . .	68
5.6.1	Evaluation Against Existing Methods . . . . .	68
5.6.2	Clinical Relevance . . . . .	70
5.6.3	Algorithm Limitations . . . . .	71
5.7	Summary . . . . .	72
<b>6</b>	<b>Multi-channel Registration of Brain MRI</b>	<b>73</b>
6.1	Introduction . . . . .	73
6.2	Vectorized Adaptive Bases Registration Algorithm (VABRA) . . . . .	75
6.2.1	Introduction . . . . .	75
6.2.2	Methods . . . . .	75
6.2.2.1	Multi-Channel Cost Function . . . . .	75

6.2.3	Experiments and Results . . . . .	76
6.2.3.1	Toy Image Simulation . . . . .	76
6.2.3.2	Deformation Recovery Using Phantom and Real MR Data . . . . .	77
6.3	Distance Transforms as Second Channel . . . . .	79
6.3.1	Introduction . . . . .	79
6.3.2	Methods . . . . .	80
6.3.2.1	Integrating Distance Transform of Anatomical Segmentation . . . . .	80
6.3.2.2	Data . . . . .	81
6.3.3	Experiments and Results . . . . .	81
6.3.3.1	Mutual Information With Regard to Rotation . . . . .	81
6.3.3.2	Single-Channel Known Deformation Recovery . . . . .	82
6.3.3.3	Segmentation Comparison of Multi-Channel Results . . . . .	83
6.4	Using Image Synthesis for Multi-modal Registration . . . . .	83
6.4.1	Introduction . . . . .	83
6.4.2	Methods and Materials . . . . .	84
6.4.2.1	Data . . . . .	84
6.4.2.2	MRI Contrast Synthesis and Normalization . . . . .	85
6.4.2.3	Using Synthesized Images in the Multi-channel Framework . . . . .	86
6.4.2.4	Registration Algorithms . . . . .	86
6.4.3	Experiments . . . . .	86
6.4.3.1	Intra-subject Deformation Recovery . . . . .	86
6.4.3.2	Intra-subject Qualitative Boundary Analysis . . . . .	87
6.4.3.3	Inter-subject Label Transfer Validation . . . . .	87
6.5	Summary . . . . .	89
<b>7</b>	<b>Conclusion and Future Work</b> . . . . .	<b>92</b>
7.1	Introduction . . . . .	92
7.2	Segmentation of Spinal Cord MRI Using Deformable Initializations . . . . .	93
7.2.1	Main Results . . . . .	93
7.2.2	Relevance to MS Analysis . . . . .	94
7.2.3	Future Work . . . . .	94
7.3	Spinal Cord DTI Pipeline With Distortion Correction . . . . .	95
7.3.1	Main Result . . . . .	95
7.3.2	Relevance to MS Analysis . . . . .	95
7.3.3	Future Work . . . . .	95
7.4	Deformable Registration for Retinal OCT . . . . .	96
7.4.1	Main Result . . . . .	96
7.4.2	Relevance to MS Analysis . . . . .	96
7.4.3	Future Work . . . . .	97
7.5	Multi-channel Registration of Brain MRI . . . . .	97
7.5.1	Main Results . . . . .	97
7.5.2	Relevance to MS Analysis . . . . .	98
7.5.3	Future work . . . . .	99
7.6	Conclusion . . . . .	99
	<b>Bibliography</b> . . . . .	<b>100</b>
	<b>Vita</b> . . . . .	<b>113</b>

# Abbreviations and Symbols

MR(I)	magnetic resonance (imaging)
DW(I)	diffusion weighted (imaging)
DT(I)	diffusion tensor (imaging)
MT	magnetization transfer
OCT	optical coherence tomography
CT	computed tomography
MI	mutual information
CC	cross correlation
SSD	sum of square differences
MSE	mean square error
1D	one-dimensional
2D	two-dimensional
3D	three-dimensional
pixel	picture element
voxel	volume element
MS	multiple sclerosis
CNS	central nervous system
CSF	cerebrospinal fluid
ILM	inner limiting membrane
BrM	Bruch's membrane
RNFL	retinal nerve fiber layer
GCL	ganglion cell layer
IPL	inner plexiform layer
INL	inner nuclear layer
OPL	outer plexiform layer
ONL	outer nuclear layer
IS	inner segment
OS	outer segment
RPE	retinal pigment epithelium
$S$	source image
$\mathcal{T}$	target image
$\mathbf{v}$	transformation field
$\mathbf{x}$	image coordinate



# List of Figures

1.1	Shown is an example of an atlas alignment using image registration between two different brain magnetic resonance images. The atlas image (top left) is transformed (top right) to be aligned with the target image (center). The transformation allows the anatomical labels from the atlas (bottom left) to be directly transferred (bottom right) to label the target image.	2
2.1	Block diagram of the general registration framework. The coloring represent the main pieces of the framework: the input images (green), the output image (purple), the similarity cost function (orange), the transformation model (blue), and the optimizer (yellow).	8
2.2	Shown are examples of registration results between a source and target MR image of the brain from two different subjects, using a <b>(a)</b> rigid, <b>(b)</b> affine and <b>(c)</b> deformable registration.	8
3.1	The center image is an illustration of a spinal cord. The left hand column shows (center) magnetization transfer-prepared T2*-weighted gradient-echo and (top and bottom) T1-weighted axial cross-sections of spinal cord MRIs and corresponding manual segmentations. The right-most column shows a sagittal slice of a T1-weighted MRI with a field of view covering the cervical and portions of the thoracic vertebrae. The green line in both the illustration and the sagittal slice on the right demarks the separation between the cervical and thoracic vertebrae.	20
3.2	Sagittally acquired T1-weighted MR slices of the spinal cord from four different healthy subjects at approximately the same field of view. This demonstrates the wide variability in the shape and curvature of the spinal cord in the images.	22
3.3	Examples of two, three, and five class segmentations using a standard tissue classification tool [55] on (top) axially acquired magnetization transfer-prepared T2*-weighted gradient-echo MRI and (bottom) sagittally acquired T1-weighted MRI of the spinal cord, each from separate healthy subjects. Results are shown for when the classification was performed on the full MRI (first two columns) and when the image was manually truncated to just the spinal cord and CSF (last four columns).	23
3.4	An example of the intensity, topology (spinal cord in light gray, CSF in dark gray, and wrapper in white) and statistical atlases constructed from a T1-weighted MRI.	26
3.5	Example of registrations between an intensity atlas and a target image using ABA and SyN.	27
3.6	Shown is <b>(a)</b> the topology atlas (spinal cord in light gray, CSF in dark gray, and wrapper in white) before initializing with a deformation learned from registration, <b>(b)</b> an example of a topology deadlock that can occur when initializing the entire topology atlas by a digital homeomorphic approximation of the deformation, and <b>(c)</b> the result when only the spinal cord is initialized by the homeomorphic deformation, and the remaining topology atlas is rebuilt dynamically.	29

3.7	Comparison of statistical priors of the spinal cord and CSF constructed using <b>(a)</b> the standard registration approach (with five segmentations) and <b>(b)</b> a single manual segmentation Gaussian smoothed. A kernel size of $\sigma = 1$ was used in both cases. Further explanation and details are in Section 3.4.2. . . . .	31
3.8	Cropped example of a MT-prepared T2*-weighted MRI segmentation by a human rater in comparison to the result from our algorithm. Shown are one sagittal and three axial views. The colored border around the axial slices denote the respective cross-section within the sagittal image. The Dice coefficient between the shown manual and automatic segmentations are 0.91 for the spinal cord (white) and 0.86 for the CSF (gray). . . . .	35
3.9	Cropped example of a T1-weighted MRI segmentation by a human rater in comparison to the result from our algorithm. Shown are one sagittal and three axial views. The colored border around the axial slices denote the respective cross-section within the sagittal image. The Dice coefficient between the shown manual and automatic segmentations are 0.87 for the spinal cord (white) and 0.73 for the CSF (gray). . . . .	36
3.10	Average Dice coefficient between automatic and manual segmentations when using statistical atlases built from the standard registration based approach (using five segmentations) and our single segmentation approach, at different levels of Gaussian smoothing ( $\sigma$ ). The left plot shows the average results for five T1-weighted images, and the right shows the average results for five MT-weighted images. . . . .	37
3.11	Shown are axial slices for four successful segmentations and the only eight failures found when processing the 238 images in the MT cohort with the presented algorithm. For each pair of images, the left shows a crop of the original MRI, while the right shows the respective spinal cord (light gray), CSF (dark gray), and wrapper (white) segmentation results from the algorithm. . . . .	38
3.12	Correlation plots showing the relationship between normalized spinal cord area (age and sex adjusted) with EDSS (top) and disease duration (bottom) for MS patients. The black line shows the relationship for all MS patients grouped together. The colored lines indicate the relationship for the specific subtypes — relapsing remitting (RR) in green, secondary progressive (SP) in blue, and primary progressive (PP) in red. The correlation ( $r$ ) and significance ( $p$ ) are given for each line. . . . .	40
4.1	An axial slice of a $b_0$ , diffusion weighted spinal cord image before and after correcting for susceptibility distortion by registering to a MT-weighted image from the same subject. . .	48
4.2	Example of field of view (FoV) differences between a diffusion $b_0$ image and a MT image from the same subject. All images show the same axial slice of the spinal cord from the same subject. <b>(a)</b> shows the original FoV for each image, and <b>(b)</b> shows the image pair after matching and cropping the FoV to the spinal cord. . . . .	49
4.3	JIST layout showing our full spinal cord DTI processing pipeline. Boxed in green is our improvement to the original CATNAP pipeline, which includes our field of view matching and distortion correction approaches. . . . .	50
4.4	Tri-planar views of FA colormap results from our pipeline when using and not using the distortion correction. Also shown is the structural MT image used as the correction target. . . . .	51
5.1	Shown is a diagram of <b>(a)</b> the eye with <b>(b)</b> the macula zoomed in. <b>(c)</b> shows an example of a macular OCT image slice (B-scan) and <b>(d)</b> shows a partial segmentation of the retinal layers in the OCT. See Figure 5.2 for the names of each layer. . . . .	54
5.2	Names and abbreviations for the primary layers of the retina, and their structure as shown on an OCT image. . . . .	55
5.3	The top row shows B-scans from two OCT images used as the source and target. The second row shows example results when using the default settings for two generic deformable registration algorithms, SyN [6] and DRAMMS [96], to register the source image to the target. . . . .	57

5.4	Shown are the outputs at each step of the registration algorithm, from the source image $\mathcal{S}$ at the top, to the results of the registration after <b>(a)</b> the rigid alignment to the fovea, <b>(b)</b> the affine alignment of the A-scans and <b>(c)</b> the deformable registration. The target image $\mathcal{T}$ is shown at the bottom for reference. The bottom figures in <b>(b)</b> and <b>(c)</b> show checkerboard comparisons between each result and the target image. . . . .	61
5.5	B-scan (left) and en-face (right) views of an average atlas created from macular OCT images from 40 healthy control subjects. The green and red lines show the location of each view relative to the other. The vertical scale in the B-scan view is tripled to better show the details of the atlas. . . . .	66
5.6	Statistical atlases of the 8 retinal layers constructed from 40 healthy control subjects registered into a normalized space. . . . .	68
5.7	Shown are an image from a healthy control subject and an average atlas, their registrations to each other, and the subject's RAVENS maps for each layer, overlaid on the average atlas. Each RAVENS map is shown in log scale to better illustrate where the tissue is expanding (blue) or compressing (red) relative to the average atlas. The vertical scale of the B-scan is doubled to better show the details of the maps. . . . .	69
5.8	SPM significance map (at an $\alpha$ level of 0.05) of RAVENS differences between the control and MS cohorts overlaid on the average atlas. Shown are a B-scan view (top) and three en-face views at different depths (bottom). The colored markers on the left side of the B-scan show the depth location of each en-face view. Colored lines indicate the boundaries between each layer. The vertical scale of the B-scan view is tripled to better show the significant areas respective to the average atlas. . . . .	70
6.1	Shown in the top row are a pair of aligned T1w and T2w brain images from the same subject, demonstrating the different contrasts and features that can be seen in different MR modalities. The red boxes indicate the zoomed in regions shown in the bottom row. . . .	74
6.2	Toy example of single channel and multi-channel ABA registration results using a distance transform of a cube (rightmost column). The source images were constructed by deforming the distance transform with a $3 \times 3 \times 3$ magnitude sinusoid. The target images were constructed by taking the distance transform and replacing half of it with a constant value. . . . .	77
6.3	Registration results between two white matter segmentation masks (top row) and the same registration between their distance transforms (bottom row). . . . .	81
6.4	Plots of mutual information as a function of rotation for an MR brain image, its white matter mask and distance transform. . . . .	82
6.5	Single and multi-channel registration results between a source and target image. Shown are <b>(a)</b> the result when only using the MR images and <b>(b)</b> the result when using the distance transform of the white matter segmentation as a second channel. . . . .	83
6.6	Shown is a diagram of our method for using image synthesis to convert a single channel multi-modal registration with a source T1w and a target T2w image (top row) into a multi-channel registration using normalized ( $nT1w$ , $nT2w$ ) and synthetic ( $sT2w$ , $sT1w$ ) images created from the T1w and T2w images (bottom row). . . . .	85
6.7	Qualitative comparison of intra-subject registrations between a T1w source image and a T2w target image. The first row shows edge maps of the T1w registered results (in orange) overlaid on the T2w target, when using (a) rigid registration with NMI, (b) single channel ABA with NMI, or (c) multi-channel ABA with synthetic and normalized images. The second row shows the ventricles zoomed in for each image to better show the alignment differences. The red arrows on (c) indicate areas where there are visual improvements to alignment when using the multi-channel approach. . . . .	88

# List of Tables

3.1	Detailed demographic description for the 146 subjects in the MT cohort with manual slice numbers for the C2 and C5 vertebrae (used in Section 3.4.4 and 3.4.5). Key: healthy controls (HC), clinically isolated syndrome (CIS), relapsing-remitting (RR), primary progressive (PP), and secondary progressive (SP). . . . .	32
3.2	Evaluation of the CSF, spinal cord (“Cord”), and combined (“CSF + Cord”) segmentation results against manual segmentations from two raters (R1 and R2) for the two cohorts (T1 and MT). Shown are the mean (standard deviation) of the Dice coefficient when using just the registration (ABA and SyN) for segmentation transfer, and the final segmentation result from the presented method when using the registration for initialization. . . . .	34
3.3	Pairwise group comparisons of normalized cord area (mm <sup>2</sup> ) between healthy controls (HC) and patients with MS (ALL-MS) and the MS subtypes of clinically isolated syndrome (CIS), relapsing-remitting (RR), primary progressive (PP), and secondary progressive (SP). Shown are the mean and standard deviation of the normalized cord area for each group and the significance (p-values) of the cord area differences between each group pairing, after adjusting for age and sex. . . . .	39
3.4	Pairwise group comparisons of normalized CSF area (mm <sup>2</sup> ) between healthy controls (HC) and patients with MS (ALL-MS) and the MS subtypes of clinically isolated syndrome (CIS), relapsing-remitting (RR), primary progressive (PP), and secondary progressive (SP). Shown are the mean and standard deviation of the normalized CSF area for each group and the significance (p-values) of the CSF area differences between each group pairing, after adjusting for age and sex. . . . .	41
5.1	Dice overlap between segmentations transferred using a registration algorithm and the manual segmentation for eight retinal layers, averaged over 200 registrations (40 target and 5 source images) using SyN [6], A-OCT, and D-OCT. Asterisk (*) values on the D-OCT row indicate the layers that gained significant improvements (at an $\alpha$ level of 0.01) in Dice when comparing A-OCT against D-OCT. . . . .	66
5.2	Average layer boundary surface errors ( $\mu$ m) between segmentations transferred using a registration algorithm and the manual segmentation for nine retinal layer boundaries, averaged over 200 registrations (40 target and 5 source images) using SyN [6], A-OCT, and D-OCT. Asterisk (*) values on the D-OCT row indicate the layers that gained significant improvements (at an $\alpha$ level of 0.01) in Dice when comparing A-OCT against D-OCT. . . . .	67
6.1	Shown are the average absolute errors (in voxels) between a known deformation applied to the Brainweb phantom and the deformation recovered using single channel (“T1w” and “T2w”) and multi-channel (“T1w+T2w”) registration, for low and high deformation magnitudes. . . . .	78

6.2	Shown are the average absolute errors (in voxels) between known deformations applied to 11 MR brain images and the deformations recovered using single channel (“T1w” and “T2w”) and multi-channel (“T1w + T2w”) registration, for low and high deformation magnitudes, and when performed on full head images or images with non-brain tissues masked out. . . . .	79
6.3	Average error of the recovered deformation field, when using the whole MR image, the white matter mask, and the distance transform of the white matter mask. . . . .	82
6.4	Average Dice’s coefficient between brain structure segmentations for the registration results and for the target images. The columns indicate when the registration was performed with just a the MR image, and when the white matter mask or its distance transform were used as second channels. Shown in parentheses are the percentage increase or decrease from adding the second channel. . . . .	84
6.5	Shown are the average error (in voxels) and standard deviation of known deformation recovery experiments using T1w and T2w images from the Brainweb dataset with a single channel multi-modal registration (“T1w→T2w”), and multi-channel registrations using the synthesized images with (“[nT1w, sT2w]⇒[sT1w, nT2w]”) and without (“[T1w, sT2w]⇒[sT1w, T2w]”) the normalized images. . . . .	87
6.6	Mean (and standard deviation) of Mindboggle and TOADS label transfer Dice results, when using ABA and SyN, with different similarity metrics, for the single channel multi-modal registration (“T1w→T2w”), and multi-channel registrations using the synthesized images with (“[nT1, sT2w]⇒[sT1w, nT2w]”) and without (“[T1w, sT2w]⇒[sT1w, T2w]”) the normalized images. . The bolded values show the best results for each algorithm for a given label set. . . . .	90

*To my loving parents,  
without whom none of this could have been possible.*

# Chapter 1

## Introduction

### 1.1 Image Registration and Multiple Sclerosis

In medical image analysis, the *correspondence* between important features or analogous anatomy in two images is an important piece of information that can be used to study disease. Knowing the correspondences between spatial locations allow for comparisons between specific anatomical structures in the images. This allows us to answer questions such as, “Is this structure larger in subject A than in subject B?” or “Is that structure malformed relative to the average population?” Likewise, knowing correspondences across time allows us to study changes in rates of disease processes. For example, “Is a disease causing the structure to grow or shrink over time?” or “How does the rate of change compare to an healthy individual?”

Correspondences between images also provide the ability to transfer information, which can be used as prior knowledge for tasks such as segmentation. For example, knowing the boundary for a specific anatomical structure in image A allows the image to be used as an atlas for finding those same boundaries in other images. If the correspondences between images A and B are known, then the boundary in image A can be transferred through the correspondences and used as an approximate starting point for finding the analogous boundaries in image B.

In the field of medical imaging and computer vision, the task of computing and aligning correspondences between different images is referred to as *image registration*. Given two images, image registration algorithms use image features such as image intensities or structures in the images to find a transformation that best aligns the correspondences between the two images. In Figure 1.1 we show an example where such an algorithm is used to align the image intensities between two different brain images. We see that this alignment allows the anatomical labels on an atlas image to be directly transferred to the target image.

While the primary concept of image registration is simple, finding the solution is rather difficult. The subject has been studied extensively for the past 40 years [1], and there is still a lack of consensus

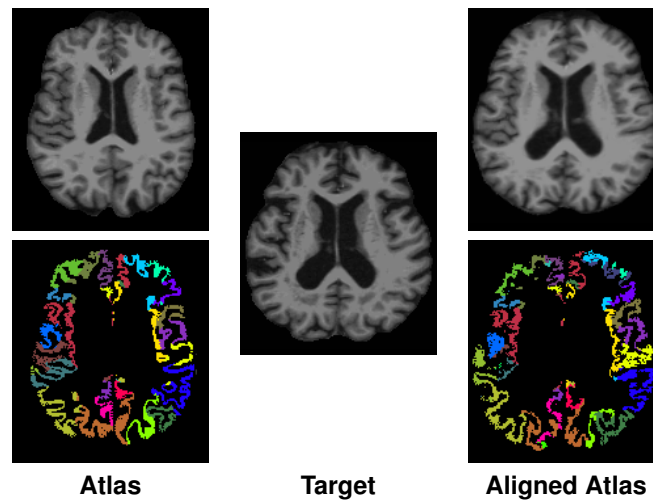


Figure 1.1 Shown is an example of an atlas alignment using image registration between two different brain magnetic resonance images. The atlas image (top left) is transformed (top right) to be aligned with the target image (center). The transformation allows the anatomical labels from the atlas (bottom left) to be directly transferred (bottom right) to label the target image.

on the best general approach for the problem. We often cannot determine what are the correct correspondences between two images. In addition, we rarely know the exact way to model the transformation that best aligns those correspondences. We see from the example in Figure 1.1 that aligning the intensity correspondences do not accurately align all of the anatomical correspondences between the images.

The number of varieties and applications of image registration that have been presented to date is tremendous [2, 3]. In this dissertation, we will only discuss a limited subset of these techniques. The main focus of this dissertation is on the application and development of these registration algorithms for the analysis of multiple sclerosis (MS), a neurodegenerative disease that damages the myelin sheath of nervous tissue, and often results in physical and mental debilitation. One challenge of studying MS is that the disease is known to affect the entire central nervous system (CNS). As a result, the analysis of the disease requires the ability to span across multiple anatomical structures. In this dissertation, we address the three primary areas of the CNS that are currently of most interest in the study of MS – the spinal cord, the retina, and the brain.

For image registration, each of these anatomical structures present their own challenges that are specific to the morphology of each structure. In addition, the imaging technologies used to study and analyze these structures are not consistent. Even for cases where the same imaging device is used, there are inherent differences that must be addressed. For example, in spinal cord and brain magnetic resonance imaging (MRI), the type of coils used to fit the head is significantly different than those used for the spine. As a result, the coils produce MR images that contain substantially different characteristics such as noise, artifacts, and resolution. In the case of the retina, the structure is far too small for MR to sufficiently capture the details of the anatomy. Hence, a completely different imaging device (optical coherence tomography) must be used, which introduces its own set of challenges when registering the



retina. In each of these cases we make improvements on our ability to accurately and robustly register the specific anatomical structure, which allows us to develop and perform previously unused analysis techniques for the study of MS in those structures.

## 1.2 Dissertation Overview

### 1.2.1 Contributions

In this dissertation we make four main contributions towards the development and application of deformable registration tools for the analysis MS:

**Segmentation of Spinal Cord MRI Using Deformable Initializations** Our first contribution is the development of a fully automatic segmentation of the spinal cord and cerebrospinal fluid (CSF) in MRI. The primary challenge of segmenting the spinal cord in MR images is that the structure is very small and flexible. Hence, the position and curvature of the spinal cord in the image is difficult to predict. As a result, analysis that require spinal cord segmentations are typically performed manually or semi-automatically, which limits the size of such studies.

In our approach we address this limitation by using deformable registration to transfer a set of intensity, statistical, and topology atlases to the target image. The registration accounts for the variations in the spinal cord's location and curvature in the image, and provides a reliable initialization for a topology preserving tissue classification approach to segment the spinal cord. Our method was validated against manual segmentations, and showed high levels of accuracy and robustness. By providing an automatic approach for segmenting the spinal cord that is comparable to manual raters, we allow for large scale studies of the spinal cord to be performed when studying MS. We demonstrated this by running an analysis of spinal cord atrophy between healthy volunteers and MS patients using a dataset consisting of 146 spinal cord MR images.

**Spinal Cord Diffusion Tensor Imaging Pipeline with Distortion Correction** Our second contribution is an improved spinal cord diffusion tensor imaging processing pipeline that is able to correct for susceptibility distortions in diffusion weighted (DW) images. Due to the echo planar sequence used for diffusion weighted acquisitions, DW images suffer from geometric distortions in regions near tissue transitions. This is particularly problematic for the spinal cord due to the bone-tissue interface in the spine, and air-tissue interface in the throat. These distortions cause diffusion metrics (e.g., fractional anisotropy, mean diffusivity, etc.) calculated from the images to be highly inaccurate and unreliable for analysis.

In our pipeline we correct for this distortion by using a deformable registration constrained to only transform in the phase-encode direction, where the distortion is mostly oriented. The registration is performed using an undistorted structural image as the target. This correction allows us to make more accurate calculations of diffusion metrics from spinal cord MRI. The improved metrics provided by this

pipeline has led to several studies by our clinical collaborators, which showed significant correlations between diffusion imaging metrics and clinical measures of sensorimotor function and disability levels.

**Deformable Macular OCT Registration** Our third contribution is a deformable registration approach designed specifically for aligning optical coherence tomography (OCT) images of the retina. Since OCT is a relatively new imaging technology, registration methods for the modality are not fully developed. In addition, image registration in retinal OCT is challenging, because the cornea provides a final optical lens for the imaging device that is specific to each individual. As a result, images are not recorded in their physical scan locations, which makes it difficult for generic registration approaches to align the retinal structures.

Our method addresses this limitation by constraining the registration to only perform transformations in the directions that we know are geometrically correct. Hence, we only allow rigid translations by whole A-scans, and limit all other transformations to be parallel to the A-scan direction. This allows for a more accurate registration that respects the geometry of the OCT image. Using manual segmentation of the retinal layers, we compared our method against several generic registration approaches that do not limit the registration to the OCT geometry. Our results showed that, on average, our proposed approach produced the best retinal layer alignment out of all the methods.

Our registration method enables a number of deformation and atlas based analysis techniques for studying the retina in MS patients, which previously could not be used due to a lack of reliable deformable registration for retinal OCT. To demonstrate such a technique, we used our registration to perform a voxel-based volumetric analysis [4] of macular OCT from healthy volunteers and MS patients. The analysis showed significant differences between the healthy and MS cohorts in regions of the retina that is consistent with previous findings on retinal layer changes in MS. The advantage of our analysis is the ability to detect where specifically in the 3D image such changes are occurring, whereas previous analysis relied on average OCT thickness calculated across 2D regions of the macula or post-mortem histology.

**Multi-channel Registration Using Distance Transforms and Image Synthesis** The fourth and final contribution in this dissertation is the development of a multi-channel framework for the ABA [5] registration algorithm, which allows additional contrasts and information to be used in the registration. We use this multi-channel framework to solve two challenges in brain MRI registration. First we address a drawback inherent to the mutual information cost function, which is one of the most widely used measures for comparing similarity in image registration. Being a probabilistic measure, mutual information loses its effectiveness as a matching criterion when working within areas of an image that have very homogeneous intensity, such as the white matter tissue in the brain. To solve this problem, we developed an approach that includes distance transforms of white matter segmentation as a second channel in our multi-channel framework. Since the distance transform overlaps the white matter directly, this populates the white matter

regions with distance information that allows the second channel to drive the registration in the areas where mutual information is not effective in the first channel.

The second challenge we address is on how to perform multi-channel registration when there is data missing, such as when the source and target images have different modalities. In general, multi-channel registration can not be used when the source and target images do not have analogous modalities in each of the channels. This is problematic when registering new datasets to old datasets that do not have all the modern modalities, or when trying to perform intra-subject multi-modal registration. To solve this problem we developed an approach that uses image synthesis to fill in the incomplete channels by creating the missing modalities from the existing ones. This allows single channel multi-modal problems to be converted into a multi-channel registration with several mono-modal channels that are each registered within itself. In addition, the approach allows our multi-channel registration to be used with almost any MR dataset, regardless of the modalities available. Both applications of our framework was validated using deformation recovery experiments with phantom MRI data, and label transfer experiments with real MRI data. Our results showed statistically significant improvements in accuracy when using the multi-channel framework with the proposed approaches.

Together, the goal of these four contributions aim to improve our understanding of MS through the development of advanced techniques that enable previously unavailable analysis of the disease. All of the software presented in this dissertation is open source, and are released either as part of the JIST software package (<http://www.nitrc.org/projects/toads-cruise/>), or as Matlab code (<https://www.iacel.ece.jhu.edu/>).

## 1.2.2 Organization

This dissertation is organized in the following manner. In Chapter 2 we provide an introduction to image registration. This includes our notation and framework for the registration problem, descriptions of several common registration types, and the main algorithms used in our work. Also included are some background information on MS, its clinical significance, and the challenges we face when analyzing the disease. The remaining chapters in this dissertation are then divided according to the anatomical structures being worked with. Due to the imaging technology for each anatomical structure being different, the images vary greatly in characteristics, quality, and artifacts between structures. As a result, the challenges and goals of our work also shift with each structure. Separating our work by anatomy allows us to frame our contributions with respect to standard techniques currently used for each particular structure.

In Chapter 3, we present our approach for performing robust and accurate segmentation of the spinal cord and cerebrospinal fluid in MRI using a deformable registration for initialization. Chapter 4 presents our pipeline for calculating accurate diffusion metrics from spinal cord DWI by correcting for susceptibility distortion in the images. In Chapter 5, we introduce our approach for rigidly and deformably registering retinal OCT, which allows us to perform atlas based analysis of volumetric population differences between healthy volunteers and MS patients. Chapter 6 describes our multi-channel registration framework, and our application of the framework with distance transforms and image synthesis to improve

multi-modal registration of brain MRI. Lastly, Chapter 7 presents a summary of the contributions provided in each of the previous chapters. In addition, we discuss how each contribution has improved our understanding of MS through the use of deformable registration based techniques, and potential future directions for the work.

# Chapter 2

## Background

### 2.1 Introduction

In this chapter, we present our notation and framework for the general registration problem and several common registration types that we refer to in later chapters. This includes brief discussions on popular transformation models and cost functions that are often used in image registration and descriptions for the two main registration algorithms (ABA [5] and SyN [6]) used in our experiments. Since multiple sclerosis is the main application of our work, the final section in the chapter is dedicated to discussing the significance of the disease and the challenges that arise when studying it.

### 2.2 Basics of Image Registration

The main goal of an image registration algorithm is to take a moving *source image* and transform it to be spatially or temporally aligned with a static *target image*. The algorithm is generally defined by two parts: the type of transformation allowed to be performed on the source image (the *transformation model*) and a definition of good alignment (the *similarity cost function*) between the two images. The algorithm is often iterative, in which case there is also an *optimizer*, which searches for how to adjust the transformation to best minimize the cost function. This is typically performed by estimating a transformation using the model, applying it to the source image, and then evaluating the cost function between the transformed source image and the target image. This cost then informs the algorithm on how to estimate a more accurate transformation for the next iteration. The process is repeated and optimized until either the source and target images are considered aligned (i.e., a local minimum is reached in the cost function), or a maximum iteration count is exceeded. Figure 2.1 summarizes this iterative framework as a block diagram. Figure 2.2 shows several examples of registration results when using different transformation models to register between two MR images of the brain,

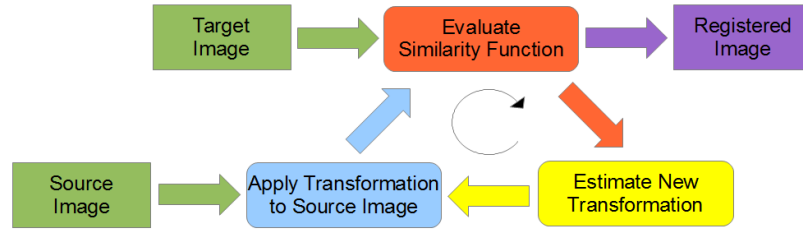


Figure 2.1 Block diagram of the general registration framework. The coloring represent the main pieces of the framework: the input images (green), the output image (purple), the similarity cost function (orange), the transformation model (blue), and the optimizer (yellow).

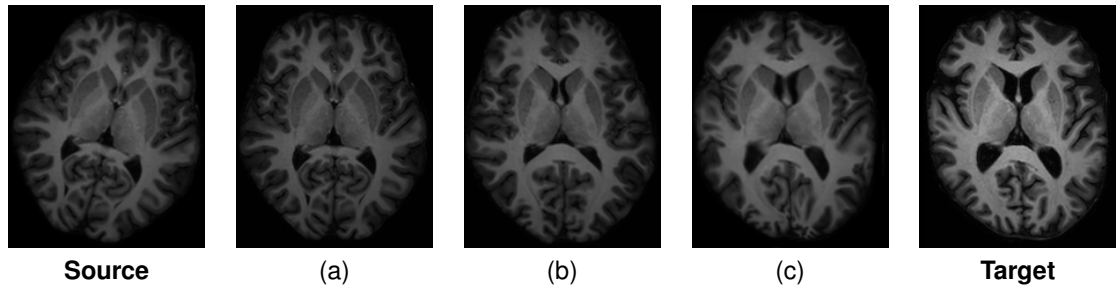


Figure 2.2 Shown are examples of registration results between a source and target MR image of the brain from two different subjects, using a (a) rigid, (b) affine and (c) deformable registration.

## 2.2.1 Registration as a Minimization Problem

To describe the general registration problem, we begin by using functions  $\mathcal{S}(\mathbf{x}')$  and  $\mathcal{T}(\mathbf{x})$  to represent the source and target images, where  $\mathbf{x}' = (x', y', z')$  and  $\mathbf{x} = (x, y, z)$  describe 3D coordinates in the source and target image domains ( $\mathbb{D}_{\mathcal{S}}$  and  $\mathbb{D}_{\mathcal{T}}$ , respectively), and  $\mathcal{S}(\mathbf{x}')$  and  $\mathcal{T}(\mathbf{x})$  are the intensities of each image at those coordinates. The primary goal of image registration is to estimate a transformation  $\mathbf{v} : \mathbb{D}_{\mathcal{T}} \rightarrow \mathbb{D}_{\mathcal{S}}$ , which maps corresponding locations between  $\mathcal{S}(\mathbf{x}')$  and  $\mathcal{T}(\mathbf{x})$ . This is generally represented as a *pullback* vector field,  $\mathbf{v}(\mathbf{x})$ , where the vectors are rooted in the target domain and point to locations in the source domain. The field is applied to  $\mathcal{S}(\mathbf{x}')$  by pulling source image intensities into the target domain. This produces the registration result, a transformed source image,  $\tilde{\mathcal{S}}$ , defined as

$$\tilde{\mathcal{S}}(\mathbf{x}) = \mathcal{S} \circ \mathbf{v}(\mathbf{x}) = \mathcal{S}(\mathbf{v}(\mathbf{x})), \quad \forall \mathbf{x} \in \mathbb{D}_{\mathcal{T}}, \quad (2.1)$$

which has coordinates in the target domain.

The typical registration algorithm aims to find  $\mathbf{v}$  such that the images  $\tilde{\mathcal{S}}$  and  $\mathcal{T}$  are as similar as possible, while constraining  $\mathbf{v}$  to be smooth and continuous so that the transformation is physically sensible. This can be performed by minimizing a cost function  $\mathcal{C}(\cdot, \cdot)$  that evaluates how well aligned  $\mathcal{S} \circ \mathbf{v}(\mathbf{x})$  and  $\mathcal{T}(\mathbf{x})$  are to each other, and forcing  $\mathbf{v}$  to follow a specific transformation model. Together we

can describe this problem as a standard minimization problem,

$$\underset{\mathbf{v}}{\operatorname{argmin}} \mathcal{C}(\mathcal{S} \circ \mathbf{v}, \mathcal{T}), \quad (2.2)$$

where the transformation  $\mathbf{v}$  is the parameter being optimized.

## 2.2.2 Types of Registration

Registration algorithms are generally categorized by the transformation model used to constrain  $\mathbf{v}$  and the cost function  $\mathcal{C}$  to evaluate similarity. The optimization approach, while important, does not usually characterize the algorithm, and is often chosen to best complement the other two components of the algorithm. In this section we cover several standard models and cost functions that are regularly used in medical imaging. However, the actual number of registration varieties in the current literature is extensive and outside the scope of this work. Several literature reviews on image registration exist for a more comprehensive understanding of the subject [2, 3].

### 2.2.2.1 Types of Transformation Models

The transformation model used to constrain  $\mathbf{v}$  in the registration algorithm is generally chosen to match the problem at hand. For example, suppose we know that the source and target image is of the same person, and their only difference is caused by a turn of the head in the scanner. In such a case, we would want to use a registration algorithm that restricts  $\mathbf{v}$  to only perform translations and rotations in order to limit the possible transformation to what we expect has occurred. However, if the two images are of different people, then we might consider a more fluid transformation that can nonlinearly align parts of the anatomy. Here we will discuss two main archetypes of transformation models that are regularly used in medical imaging.

**Transformation Matrix Models** One common choice for the transformation model is to represent  $\mathbf{v}$  entirely through a global transformation on the image coordinate system. Here  $\mathbf{v}$  is described by a single linear transformation matrix  $M$  and a translation vector  $\mathbf{t} = (t_x, t_y, t_z)$ ,

$$\mathbf{v}(\mathbf{x}) = M\mathbf{x} + \mathbf{t}. \quad (2.3)$$

The transformation matrix  $M$  determines the restrictiveness of the model, which is often referred to as the model's *degrees of freedom* (dof). Algorithms that only allow translations and rotations (6 dof) are referred to as *rigid* registrations. In such cases,  $M$  is the product of three rotation matrices (one for each axis),

$$M_{\text{rigid}} = \begin{bmatrix} 1 & 0 & 0 \\ 0 & \cos \theta_x & -\sin \theta_x \\ 0 & \sin \theta_x & \cos \theta_x \end{bmatrix} \begin{bmatrix} \cos \theta_y & 0 & \sin \theta_y \\ 0 & 1 & 0 \\ -\sin \theta_y & 0 & \cos \theta_y \end{bmatrix} \begin{bmatrix} \cos \theta_z & -\sin \theta_z & 0 \\ \sin \theta_z & \cos \theta_z & 0 \\ 0 & 0 & 1 \end{bmatrix}, \quad (2.4)$$

where  $\theta_x$ ,  $\theta_y$ , and  $\theta_z$  determine the amount of rotation around each axis. If global scaling is also allowed (7 dof) then the algorithm becomes a *similarity* registration, and  $M_{rigid}$  is multiplied with an additional scaling matrix:

$$M_{similarity} = \begin{bmatrix} s & 0 & 0 \\ 0 & s & 0 \\ 0 & 0 & s \end{bmatrix} M_{rigid}, \quad (2.5)$$

where  $s$  determines the amount of scaling. Finally, adding individual scaling and shearing (12 dof) allows for an *affine* registration. Here the scaling matrix is modified to have independent terms  $s_x$ ,  $s_y$ , and  $s_z$  for each axis, and a shear matrix is included in the product,

$$M_{affine} = \begin{bmatrix} 1 & h_{xy} & h_{xz} \\ h_{yx} & 1 & h_{yz} \\ h_{zx} & h_{zy} & 1 \end{bmatrix} \begin{bmatrix} s_x & 0 & 0 \\ 0 & s_y & 0 \\ 0 & 0 & s_z \end{bmatrix} M_{rigid}, \quad (2.6)$$

where the six  $h$  terms describe the direction and magnitude of shearing in each axis.

The main application of these models is to account for registration problems where the source and target images differ by very limited transformations. Rigid registration is regularly used to align images of the same subject, allowing for more accurate longitudinal analysis. It is also applied to images from different subjects to remove global misalignment, such as movement or shifts in position, while still maintaining the physical structure in the images. Similarity and affine registrations are used when the images are expected to have differences in size or large regional transformations. In medical imaging, they offer a way to normalize different subjects in order to remove effects that are often considered unrelated to the disease being studied, such as the size of the head. In addition, affine registrations can be used to provide an initialization for more fluid registrations by removing large sweeping differences, and allowing the subsequent algorithm to focus on aligning more detailed differences. Figure 2.2a and 2.2b provide examples of results from rigid and affine registrations between brain MRIs from two different subjects.

**Deformable Model** The main disadvantage of using only a transformation matrix to represent  $\mathbf{v}$  is its inability to account for local differences between the source and target images. To perform such alignments, a *deformable* registration is necessary, where the transformation is individually defined at each point in the image using a vector field,

$$\mathbf{v}(\mathbf{x}) = \mathbf{x} + \mathbf{u}(\mathbf{x}). \quad (2.7)$$

The vector field  $\mathbf{u}$  is referred to as a *displacement field* and is generally restricted to be smooth and continuous to ensure the overall deformation is regularized so that the object is transformed in a physically sensible way.



Deformable registration can be loosely divided between algorithms that use parametric or nonparametric transformation models to represent  $\mathbf{v}$ . Parametric registrations use a set number of parameters to control basis functions, such as splines [7] or radial basis functions [5], to construct and interpolate  $\mathbf{v}$ . The algorithm optimizes these parameters to find the best  $\mathbf{v}$  that minimizes the cost function. The transformations found under these models are often smooth and continuous by construction due to the basis functions used.

Nonparametric registrations are generally designed to create transformations that resemble physical motions such as elasticity [8], viscosity [9], diffusion [10], and diffeomorphism [11]. Rather than optimizing a set of parameters, the algorithm evolves the transformation at every iteration using forces imposed by the model. The strength and direction of these forces are determined by the cost function chosen and the constraints of the physical motion being modeled.

The primary application of deformable registration is to compute and align detailed correspondences between the source and target images. This allows such registrations to be better suited for information transfer tasks, such as deforming anatomical labels in the source image to match and label the same structures in the target image, and providing an initialization using various atlases and priors. In addition, the displacement field learned in the registration represent relative spatial change between correspondences in the source and target image. Hence it can be used to analyze morphology and shape differences between individuals [12, 13]. Figure 2.2c shows an example of a deformable registration performed using the adaptive bases algorithm (see Section 2.3.1) after an affine alignment. Compared to the affine result, we see that the individual structures within the brain are now locally better aligned to match the same structures in the target brain.

### 2.2.2.2 Types of Cost Functions

The purpose of the similarity cost function is to quantify how closely aligned the transformed source image and target images are to each other. Since it drives the optimization of the transformation model, the characteristics of the cost function determines what kind of images can be aligned, the degree of accuracy, and the ease of optimization. In this section we will mainly discuss the three most popular intensity based cost functions, which are available in most algorithms. Naturally, a large number of cost functions have been proposed in the literature, and a more complete list can be found here [2].

**Sum of Square Differences** Sum of square differences (SSD), or equivalently mean squared error (MSE), between image intensities is one of the most basic, and earliest cost functions used for evaluating the similarity between two images. It consists simply of subtracting the intensity difference at each voxel between two images, squaring the difference, and then summing across all the voxels in the entire image. This can be described using

$$C_{\text{SSD}}(\mathcal{T}, \tilde{\mathcal{S}}) = \sum_{\mathbf{x} \in \mathbb{D}_{\mathcal{T}}} (\mathcal{T}(\mathbf{x}) - \tilde{\mathcal{S}}(\mathbf{x}))^2. \quad (2.8)$$

The advantage of SSD is that it is computationally efficient, requiring only roughly three or four operations per voxel. In addition, it is very localized, since each voxel between the source and target pair is calculated independently and then summed. This allows non-overlapping regions of the image to be calculated and optimized in parallel. In addition, this provides high local acuity, which allows small spatial differences between the images to be resolved by the cost function.

The main drawback of using SSD is that it is highly dependent on the absolute intensity values in the image. If correspondences in two images do not have exactly the same intensity range, the cost function will fail to register them correctly. As a result, SSD is very susceptible to errors in the presence of artifacts, intensity shifts, and partial voluming in the images.

**Normalized Cross Correlation** The cross correlation (CC) function is a concept borrowed from signal processing theory for comparing the similarity between waveforms. It requires vectorizing the image (reshaping the 3D image grid into a single vector), subtracting the mean of each image, and then computing the dot product between the image vectors. The value is then divided by the magnitude of both mean subtracted vectors. This can be described by,

$$c_{CC}(\mathcal{T}, \tilde{\mathcal{S}}) = \left\langle \frac{(\mathcal{T} - \mu_{\mathcal{T}})}{\|\mathcal{T} - \mu_{\mathcal{T}}\|}, \frac{(\tilde{\mathcal{S}} - \mu_{\tilde{\mathcal{S}}})}{\|\tilde{\mathcal{S}} - \mu_{\tilde{\mathcal{S}}}\|} \right\rangle \quad (2.9)$$

$$= \frac{1}{\|\tilde{\mathcal{S}} - \mu_{\tilde{\mathcal{S}}}\| \|\mathcal{T} - \mu_{\mathcal{T}}\|} \sum_{\mathbf{x} \in \mathbb{D}_{\mathcal{T}}} \left( (\mathcal{T}(\mathbf{x}) - \mu_{\mathcal{T}})(\tilde{\mathcal{S}}(\mathbf{x}) - \mu_{\tilde{\mathcal{S}}}) \right), \quad (2.10)$$

where  $\mu_{\mathcal{T}}$  and  $\mu_{\tilde{\mathcal{S}}}$  are the mean intensities of each image, and  $\|\cdot\|$  indicate the  $L_2$  norm of the vectorized image intensities.

The primary advantage of CC over SSD is that it is robust to relative intensity shifts in the image, while SSD is not. This is due to the normalization using the image mean and magnitude, and the reliance on multiplication of voxel pairs instead of absolute differences. In the absence of an intensity shift, NCC can be shown to be equivalent to SSD as a cost function for optimization.

The drawback of CC is that both the mean and magnitude requires a calculation over the entire image, hence NCC loses much of the parallelization potential of SSD. In addition the gradient on the function is more complicated to evaluate, which makes it a more difficult problem to optimize.

**Mutual Information** Mutual information is a probabilistic measure of similarity derived from information theory. Using mutual information for image registration was originally presented in [14], and since then it has become one of the most widely used registration cost functions [3]. Its success largely comes from its probabilistic nature, which gives it robustness to noise and shifts in intensity. In addition, the measure avoids evaluating direct intensity differences, and instead looks at how the intensities between the two images are interdependent. This makes it a very robust measure for evaluating similarity between images with different modalities.

Mutual information is described from an information theory perspective. Hence, we start with a discrete random variable  $\mathcal{A}$ , with  $P_{\mathcal{A}}(a)$  representing the probability of the value  $a$  occurring in  $\mathcal{A}$ . The Shannon Entropy [15] of this variable is defined by

$$H(\mathcal{A}) = - \sum_a P_{\mathcal{A}}(a) \log (P_{\mathcal{A}}(a)) . \quad (2.11)$$

If the random variable represents image intensity values, then this entropy measures how well a given intensity value in the image can be predicted. Similarly, for a second random variable  $\mathcal{B}$  and joint probability distribution  $P_{\mathcal{A},\mathcal{B}}(a, b)$ , the joint entropy is

$$H(\mathcal{A}, \mathcal{B}) = - \sum_{a,b} P_{\mathcal{A},\mathcal{B}}(a, b) \log (P_{\mathcal{A},\mathcal{B}}(a, b)) , \quad (2.12)$$

which represents how well a given pair of intensity value in the images can be predicted. Using these terms, the mutual information is given by

$$\text{MI}(\mathcal{A}, \mathcal{B}) = H(\mathcal{A}) + H(\mathcal{B}) - H(\mathcal{A}, \mathcal{B}) , \quad (2.13)$$

which becomes

$$\mathcal{C}_{\text{MI}}(\mathcal{T}, \tilde{\mathcal{S}}) = - \left( H(\mathcal{T}) + H(\tilde{\mathcal{S}}) - H(\mathcal{T}, \tilde{\mathcal{S}}) \right) , \quad (2.14)$$

within the context of our registration problem. Since MI increases when the images are more similar, we negate the measure in order to fit our minimization framework.

Intuitively, mutual information describes how dependent the intensities in one image is on the other. We see that when the images are entirely independent, then the joint entropy becomes the sum of the individual entropies and the mutual information is zero. On the other hand, when the images are entirely dependent (i.e.,  $\mathbf{v}$  maps  $\mathcal{S}$  exactly to  $\mathcal{T}$ ), then the joint entropy becomes the entropy of the target image and the mutual information is maximized. In practice, the entropy and joint entropies are calculated empirically from histograms (and joint histograms) of the intensities in the images.

Since the range of entropy is sensitive to the size of the image, it is common to use a normalized variant of the measure called normalize mutual information (NMI) [16]:

$$\text{NMI}(\mathcal{T}, \tilde{\mathcal{S}}) = \frac{H(\mathcal{T}) + H(\tilde{\mathcal{S}})}{H(\mathcal{T}, \tilde{\mathcal{S}})} . \quad (2.15)$$

We see that this measure ranges from one to two, where two indicates a perfect alignment. Hence, we must again negate the measure when using it as a cost function to fit our minimization framework.

The main drawback of mutual information comes from its probabilistic nature. The measure relies on an accurate estimate of the probability density of the image intensities. As a result, its effectiveness

decreases significantly when working with small regions within the image, where there is not enough intensity samples to accurately estimate such densities. Likewise, the measure is ineffective when facing areas of the image that has poor statistical consistency or lack clear structure [17]. Examples of this includes cases where there is overwhelming noise or conversely, when the area has very homogeneous intensities and provides very little information. As a result, mutual information must be calculated over a relatively large region of the image, which reduces the measure’s local acuity and diminishes its ability to handle small changes between the source and target images. Lastly, as mentioned before, mutual information is almost entirely calculated from counts of intensity pairs, where the actual intensity value does not matter. While this is useful for addressing multi-modal relationships, it also introduces inherent ambiguity into the measure. Given a source and target image, their intensities can be paired in multiple ways to give the exact same mutual information after the transformation. Hence, the measure depends heavily on having a good initialization where the objects being registered are aligned well enough to give the correct intensity pairings at the start of the optimization. Otherwise, mutual information can cause the algorithm to align intensities pairs that incorrectly represent the correspondence between the images, resulting in registration errors [18].

## 2.3 Deformable Registration Algorithms Used In This Work

### 2.3.1 ABA

The main deformable registration algorithm we use and develop upon in this dissertation is the adaptive bases algorithm (ABA), originally presented by Rohde et al. [5]. The algorithm was chosen for several reasons. First, it has been shown to be very robust for handling a wide array of data, particularly when working with different modalities and anatomical structures. Chapter 4 presents our successful application of the algorithm for segmenting and fixing distortion in spinal cord MRI, and Chapter 5 presents our adaptation of the algorithm to handle OCT images of the retina. The deformation model, cost function, and optimization scheme used by ABA is very flexible. This allows us to make changes to particular areas of the algorithm without dramatically impacting the other parts. Together these advantages make ABA a good starting point for extensions into multivariate registration (Chapter 6).

The distinguishing feature of ABA is its model for representing the transformation  $\mathbf{v}$ , which is constructed entirely from radial basis functions (RBFs). A radial basis function is any function  $\Phi(\mathbf{x})$ , such that its values are only dependent on their distance from some center point  $\mathbf{c}$ , i.e.,  $\Phi(\mathbf{x}, \mathbf{c}) = \Phi(\|\mathbf{x} - \mathbf{c}\|)$ , where the norm is usually the Euclidean distance. We can represent a smooth transformation  $\mathbf{v}(\mathbf{x})$  as a linear combination of RBFs with center locations  $\mathbf{c}_i$  and coefficients  $w_i$ :

$$\mathbf{v}(\mathbf{x}) = \mathbf{x} + \sum_i w_i \Phi(\|\mathbf{x} - \mathbf{c}_i\|). \quad (2.16)$$

The RBFs used in ABA are defined by,

$$\Phi(\mathbf{x}) = \phi\left(\frac{\|\mathbf{x}\|}{s}\right), \quad (2.17)$$

and

$$\phi(r) = (1 - r)_+^4(3r^3 + 12r^2 + 16r + 4), \quad (2.18)$$

where  $r \geq 0$ , and  $(1 - r)_+ = \max(1 - r, 0)$ , which has circular support with radius  $s$ . This RBF was originally chosen in [5] for its smoothness and positive definiteness, which allows the deformation to be well defined when computing gradients and partial derivatives. Its compact support also reduces the computational complexity when optimizing the coefficients,  $w_i$ , by allowing non-overlapping RBFs to be optimized independently of one another. Rohde et al. [5] showed that by using this RBF with reasonable constraints on the weights, the deformations produced by ABA will be smooth and continuous.

One concern with using the RBF model is determining where to place each RBF during the optimization. Due to the size of most medical images, it is computationally impractical to place an RBF at each point and optimize over all of them. To address this, ABA uses a hierarchical approach to solve for  $\mathbf{v}$  across multiple scales and resolutions. Each iteration of the algorithm refines  $\mathbf{v}$  from an initial coarse mapping between downsampled versions of the source and target images, and then move up to the original resolution. In addition, during each scale level, the algorithm attempts to determine the regions in the image that are most misregistered by using the magnitude of the local gradient,  $G$ , of the cost function, which is evaluated using finite differences over a sub-region of the image. This can be described by,

$$G(\alpha) = \nabla_{\alpha} \mathcal{C}(\tilde{\mathcal{S}}, \mathcal{T}) \quad (2.19)$$

$$= \mathcal{C}(\tilde{\mathcal{S}}, \mathcal{T}) - \mathcal{C}(\tilde{\mathcal{S}} \circ \mathbf{v}_{\alpha}, \mathcal{T}), \quad (2.20)$$

where  $\alpha$  is the sub-region of the image where the local gradient is being evaluated, and  $\mathbf{v}_{\alpha}$  is a deformation described by a single RBF placed over  $\alpha$  to perturb the cost function. The argument is that the locations where the local cost function is changing greatly are the areas most likely to be misregistered and therefore have the most potential for improvement. Once these misregistered regions are identified, an RBF is placed at each location, and a line search algorithm is used to optimize the coefficients,  $w_i$ , in order to minimize the cost function.

### 2.3.2 SyN

The second registration algorithm that we use in our experiments is the symmetric normalization (SyN) approach originally presented by Avants et al. [6]. The algorithm ranks very high among state of the art registration algorithms in recent evaluations [19], and has placed first in both a brain mapping [20] and lung mapping competitions [21]. SyN's high performance makes the algorithm a good baseline registration approach to compare many of our methods against.

In SyN, the transformation  $\mathbf{v}$  is defined by a time varying, differentiable, invertible mapping known as a *diffeomorphism*. Such diffeomorphisms,  $\psi$ , are indexed by a variable  $t \in [0, 1]$  to represent the evolution of the transformation over time, where  $t=0$  is the identity transformation and  $t=1$  is the final transformation. In the registration, the goal is to find a diffeomorphism from the source image to the target image such that

$$\mathcal{T}(\mathbf{x}) = \mathcal{S} \circ \psi(\mathbf{x}, t = 1). \quad (2.21)$$

The main advantage of having a diffeomorphic transformation is that it is smooth and invertible by construction. For an ideal registration, the inverse of the diffeomorphism  $\psi^{-1}$  is the transformation from the target image to the source image, such that

$$\mathcal{S}(\mathbf{x}) = \mathcal{T} \circ \psi^{-1}(\mathbf{x}, t = 1). \quad (2.22)$$

However this property, known as *symmetry*, is generally not true in practice due to registration errors. Switching the registration direction by registering the target image to the source image will often produce a transformation quite different from  $\psi^{-1}$ . One of the key features of SyN is to enforce symmetry in its registrations. It does this by separating  $\psi$  into two halves, where the first half  $\psi_1$  transforms the source image to a midpoint image in between the source and target images, and the second half  $\psi_2$  transforms the target image to the same midpoint. This can be described by the constraint

$$\mathcal{S} \circ \psi_1(\mathbf{x}, t = 0.5) = \mathcal{T} \circ \psi_2(\mathbf{x}, t = 0.5). \quad (2.23)$$

To get the full transformation, the two halves are composed, where

$$\psi(\mathbf{x}, t = 1) = \psi_2^{-1}(\psi_1(\mathbf{x}, t = 0.5), t = 0.5) \quad (2.24)$$

and

$$\psi^{-1}(\mathbf{x}, t = 1) = \psi_1^{-1}(\psi_2(\mathbf{x}, t = 0.5), t = 0.5). \quad (2.25)$$

Since the middle point between the source and target images does not depend on the registration direction, this approach guarantees that the algorithm will produce symmetric registrations.

To find  $\psi_1$  and  $\psi_2$ , SyN uses the energy function,

$$E_{\text{sym}} = \inf_{\psi_1} \inf_{\psi_2} \int_{t=0}^{0.5} \left\{ \|\mathbf{w}_1(\mathbf{x}, t)\|_L^2 + \|\mathbf{w}_2(\mathbf{x}, t)\|_L^2 \right\} dt + \int_{\mathbf{x} \in \Omega} \mathcal{C}(\mathcal{S} \circ \psi_1(\mathbf{x}, 0.5), \mathcal{T} \circ \psi_2(\mathbf{x}, 0.5)) d\Omega, \quad (2.26)$$

where  $\mathcal{C}$  is an image similarity cost function,  $\mathbf{w}_1$  and  $\mathbf{w}_2$  are the velocity fields of  $\psi_1$  and  $\psi_2$ , and  $\Omega$  is the image domain at the midpoint. We see that the first term in the equation regularizes  $\psi_1$  and  $\psi_2$  by minimizing the squared norm of their velocity fields, and the second term ensures that the transformed source and inverse transformed target are aligned at the same midpoint. This energy function is optimized

by finding its gradient using Euler-Lagrange equations, and solved using a steepest gradient descent algorithm, as described by Beg et al. [11].

## 2.4 Multiple Sclerosis

### 2.4.1 Significance

Multiple sclerosis (MS) is an inflammatory disease where the myelin sheath of the nerve cells in regions of the central nervous system are damaged or destroyed. While the causes of the disease are still not entirely known, it is believed that the damage is a result of either an autoimmune response, or complications related to myelin production. The myelin sheath serves as an insulator for the axon of a neuron, and plays an important role in preserving the speed and signal strength of communication between neurons. Hence, MS can result in both physical and mental debilitation, depending on the location of the myelin damage.

MS consists of several subtypes, with the two main subtypes being relapsing-remitting (RRMS) and progressive MS. RRMS is characterized by sporadic *flare-ups*, where symptoms appear (relapse) and disappear (remit) over time. In contrast, progressive MS is characterized by a steady decline of health and function. Progressive MS is further divided into primary progressive (PPMS), where the steady decline occurs from the onset of the disease, and secondary progressive (SPMS) where the patient started with RRMS and transitioned into progressive decline.

MS is estimated to affect more than 2 million people worldwide, with an estimated cost of \$40,000–50,000 per patient per year [22]. The disease manifests most commonly in people between ages 20–40, an age range where the disease can greatly impact the able-bodied workforce, leading to additional indirect costs. On average, life expectancy for MS patients is roughly 10 years (quality-adjusted) lower than those without the disease [23].

### 2.4.2 Challenges

MS poses several challenges that make image based analysis of the disease difficult. The disease is believed to affect all areas of the CNS, which requires analysis of different anatomical structures. This results in working with different imaging technologies and imaging characteristics that are not consistent between each structure. As a general note, techniques that are successful for one anatomical structure can rarely be directly transferred to analyze another structure. Considerable improvements and modifications are often required to accommodate for the new images. This includes adjusting how the transformation is modeled, the level of expected noise, and any prior information used by the algorithm. In many cases, entirely new algorithms must be developed.

In RRMS, pathology is not consistently present in the images. Characteristic symptoms, such as brain lesions (sites of demyelination), can grow, shrink, or entirely disappear over time. This makes

registration tasks particularly difficult, since many algorithms rely on consistent correspondences to perform accurately. During periods of remission, images of RRMS patients are often indistinguishable from that of a health individual. This makes it difficult to analyze disease related differences in the subtype.

In the progressive subtypes, change is more consistent. However, they typically occur slowly. For example, white matter volume in the brain is estimated to decrease by only about 0.5% per year in MS [24]. This requires algorithms to have high longitudinal stability and accuracy in order to detect such changes over a short timespan. However, over enough time, such atrophy can accumulate which means algorithms must also be able to handle large differences in structure when analyzing more progressed patients. The requirement to simultaneously accommodate for both large and small transformations is a challenging task for image registration, since most algorithm have models tuned to address only one or the other.



## Chapter 3

# Segmentation of Spinal Cord MRI Using Deformable Initializations

### 3.1 Introduction

The human spinal cord is a long thin cylindrical structure in the central nervous system (CNS) that extends from the medulla oblongata to the lumbar vertebrae. It is the principal transmission pathway for neural signals between the brain and the rest of the body, which facilitates sensorimotor control. This primary function of the spinal cord makes it of great importance when studying diseases that lead to deterioration in CNS function, such as multiple sclerosis (MS), where inflammation in regions of the spinal cord can directly lead to weakness, loss of sensation, and disability.

*In vivo* magnetic resonance imaging (MRI) of the spinal cord presents a unique diagnostic tool for studying the progression and characteristics of MS. MRI uses electromagnetic fields to align and rotate the magnetization of hydrogen atoms in the body. When the atoms' magnetization are rotated away from a main magnetic field, they create a signal (via magnetic flux in the MRI scanner) that decays as their magnetization return to equilibrium. The rate of decay of this signal depends on the quantity and structure of the hydrogen atoms in the tissue being imaged. Hence, by measuring the signal part way through its decay, the scanner will detect different signal strengths from different tissue types. This allows the creation of a noninvasive 3D image that can show contrast between different tissues [25].

MRI based analysis of the spinal cord for studying MS can be traced as far back as Losseff et al. [24] who demonstrated strong association between spinal cord area and disability as measured by Kurtzke's Expanded Disability Status Scale [26] (EDSS) ( $r = -0.7$ ,  $P < 0.001$ ). Since then, significant progress has been made in both the analysis and application of MRI in spinal cord imaging. Kalkers et al. [27] proposed using MRI derived metrics to evaluate neuroprotective therapies. Studies from Lin et al. [28, 29] demonstrated that changes in edge detectability of the spinal cord boundary are related to changes in clinical disability. More recent work [30, 31] has shown the potential of using quantities derived

from various imaging modalities as biomarkers to characterize patients with MS. Other studies [32] have shown that cross-sectional area of the spinal cord is well correlated with cortical activity.

A common requirement for spinal cord based analysis is a full or partial segmentation of the spinal cord (see Figure 3.1) for each subject in the study, where the structure is delineated in each image. Such segmentations are typically performed manually or semi-automatically by human raters, which creates two immediate disadvantages. First, human raters are prone to unintended biases and inconsistencies in their work. This is particularly common when segmenting small structures such as the spinal cord, and is evident when replicating a segmentation of the same image or comparing between two separate raters. Second, raters require extensive training and time to perform the task. This imposes a strict limitation on the scale of studies and produces potentially long delays between acquiring the data and completing the analyses.

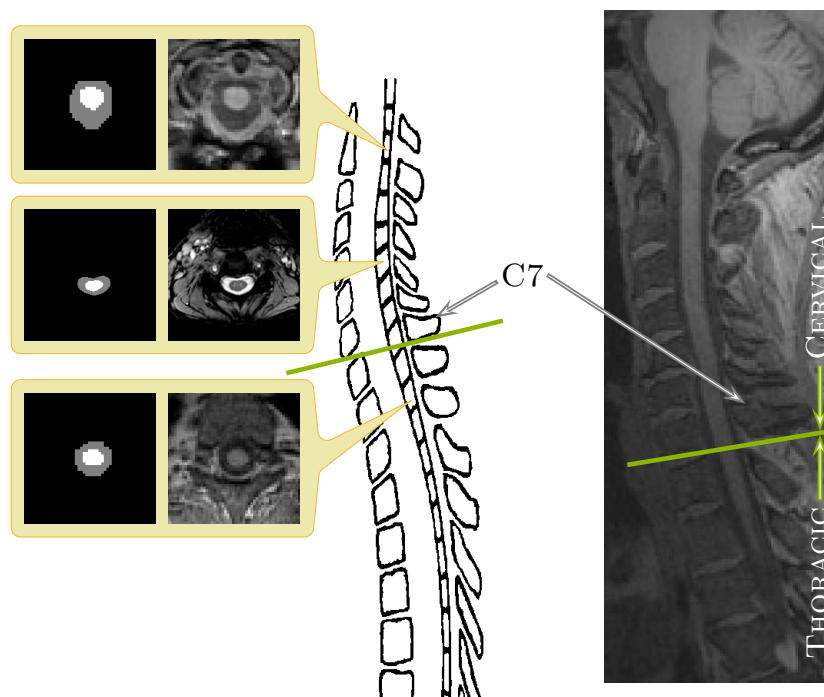


Figure 3.1 The center image is an illustration of a spinal cord. The left hand column shows (center) magnetization transfer-prepared T2\*-weighted gradient-echo and (top and bottom) T1-weighted axial cross-sections of spinal cord MRIs and corresponding manual segmentations. The right-most column shows a sagittal slice of a T1-weighted MRI with a field of view covering the cervical and portions of the thoracic vertebrae. The green line in both the illustration and the sagittal slice on the right demarks the separation between the cervical and thoracic vertebrae.

There have been several attempts to automate the segmentation of the spinal cord in computed tomography (CT) imaging [33, 34, 35, 36]. However, such methods are limited by a lack of soft tissue contrast in CT, making it difficult to distinguish between the spinal cord itself and the surrounding

cerebrospinal fluid (CSF). Most approaches are restricted to segmenting only the spinal canal, which is insufficient for analysis of spinal cord atrophy. This, in addition to concerns for patient safety, makes MRI a superior choice for imaging the spinal cord. However, MR imaging is not without its own difficulties. Inhomogeneities in receiver coil sensitivity can manifest as spatially distributed intensity biases. Susceptibility may create artifacts in the spinal cord proximal to the posterior fossa region [37]. Image quality is also degraded by truncation artifacts [38], ghosting artifacts from the heart and great vessels [39, 40, 41, 42] and intensity inhomogeneities [43]. Non-uniformity correction is particularly important for acquisitions from phased-array coils, which is often used when assessing spinal cord atrophy [29].

These drawbacks have delayed the development of fully automated MR spinal segmentation tools. As such, the majority of the methods presented thus far to address this problem have been semi-automated in nature [44, 45, 46, 47, 48]. These approaches vary from the watershed based [47] to applications of deformable models [48]. To the best of our knowledge there are only three fully automatic methods in the literature for human MRI spinal cord segmentation [49, 50, 51]. Koh et al. [49] developed a gradient vector flow [52] magnitude approach as part of a computer-aided diagnosis (CAD) system. Their algorithm estimates the spinal cord using the magnitude of the gradient vector flow edge map, followed by a connected component analysis to remove any holes in the segmentation. In Koh et al. [50], the same group developed a different approach to the problem using active contour models [53] based on saliency maps. Mukherjee et al. [51] also applied an active contour approach, but instead evolved an image gradient based, open-ended contour using dynamic programming-based energy-minimization. They initialize their method using an estimation of the vertebra bone contour in each 2D slice of the image, which is found using an optimal shortest path directed graph search based on gradient magnitude and gradient orientation. These 2D contours are then evolved under an active contour model that minimizes an energy based on the symmetry of the contour and the smoothness between successive contours (i.e., contours on adjoining 2D slices).

A common deficiency with current automated algorithms is their limitation to both a single MR-sequence and a particular field of view. The three existing methods mentioned above are designed to be used with T2 and T2\*-weighted MRIs because it offers the best soft tissue contrast [49, 50, 51]. None of them provide an intuitive and easily generalized approach for addressing MR-sequences or fields of view outside of the particular dataset they were designed for. This is problematic in spinal cord MR imaging because data is generally only collected across specific subsections of the spinal cord, and the MR-sequence is rarely standardized between datasets. Addressing these limitations is one focus of our work.

There are various reasons why existing image segmentation technologies cannot be readily applied to spinal cord MRIs. For example, the structure of the spinal cord makes typical atlas based registration highly inaccurate. This happens for two reasons; first, the long thin cylindrical nature of the spinal cord and its small size relative to the neck and torso leads to the spinal cord contributing only minimally to the overall cost function of a registration algorithm. This typically causes the registration algorithm to prioritize the alignment of other structures over the spinal cord during the optimization.

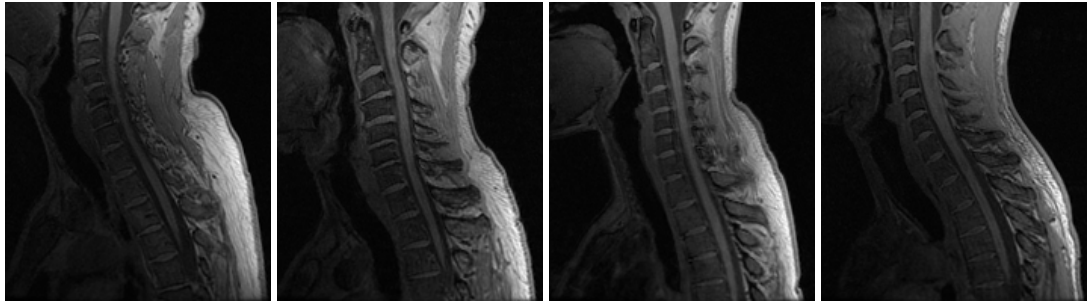


Figure 3.2 Sagittally acquired T1-weighted MR slices of the spinal cord from four different healthy subjects at approximately the same field of view. This demonstrates the wide variability in the shape and curvature of the spinal cord in the images.

Second, the spinal cord is a flexible non-rigid structure, which results in a large degree of variability in both the shape and curvature of the structure in MRIs (see Figure 3.2). This variability removes rigid and affine registrations as viable choices for the transformation. Even for free-form deformable registration the accuracy is dramatically limited due to the large deformations often required to properly align the curvatures. This is particularly true for registration with strict regularization constraints on the deformation.

Unsupervised intensity based segmentation algorithms encounter a different set of problems. They are prone to misclassification due to the partial voluming of nerve roots and the strong intensity inhomogeneities from the spine coils. The inhomogeneity from the surface coil is primarily a result of the MR signal dropping off for tissues further away from the coils. However, the problem is exacerbated by the curvature of the spinal cord. Since the cord is not parallel to the coils, the anatomy interacts with the intensity inhomogeneity unevenly. As a result, intensity values along the spinal cord are inconsistent and depend on its curvature during acquisition. This effect is particularly evident for images covering large fields of view, where both the distance from the coil and the curvature of the spinal cord is larger. Figure 3.3 shows an example of an axially acquired magnetization transfer-prepared T2\*-weighted gradient-echo image and a sagittally acquired T1-weighted MRI of the spinal cord, each from separate subjects. Both images have been segmented with a fuzzy c-means [54] approach [55] which includes gain field correction and regularization. We see that the spinal cord could not be properly segmented in any of the cases, including those where the image was manually truncated to include only the spinal cord and CSF. The intensity drop-off seen in the examples could not be handled by the inhomogeneity correction built into the classification algorithm, nor by preprocessing with N3 [56], an intensity non-uniformity correction tool commonly used in whole head MRI.

In this chapter, we present an approach for automatically segmenting the spinal cord and surrounding cerebrospinal fluid in a MR image. Our approach uses deformable registration to account for the curvature and location of the spinal cord. This allows us to perform a robust initialization for an atlas based, topolog preserving tissue classification approach that has previously been successful applied to the brain [57]. In addition, we present a method for adaptively building statistical and topology atlases for

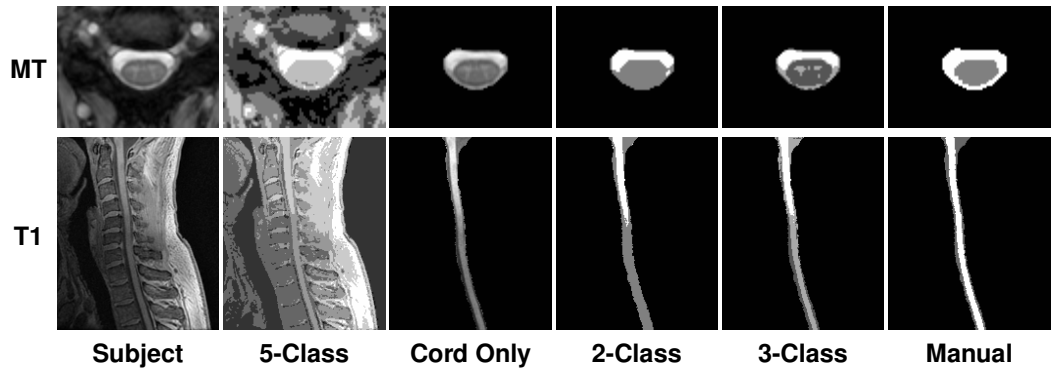


Figure 3.3 Examples of two, three, and five class segmentations using a standard tissue classification tool [55] on (top) axially acquired magnetization transfer-prepared T2\*-weighted gradient-echo MRI and (bottom) sagittally acquired T1-weighted MRI of the spinal cord, each from separate healthy subjects. Results are shown for when the classification was performed on the full MRI (first two columns) and when the image was manually truncated to just the spinal cord and CSF (last four columns).

the spinal cord, and an approach for initializing the topology atlas without breaking the digital connectivity of the objects in the atlas. These techniques allow our algorithm to be highly generalizable, providing a way to automatically generate new atlases for spinal cord data with different fields of views and modalities from a single example manual segmentation.

## 3.2 Methods

The topology-preserving, anatomy-driven segmentation (TOADS) algorithm [57] provides the main model for our segmentation approach. It is a fuzzy c-means (FCM) [54] based intensity classification algorithm that is capable of preserving the digital topology of the anatomy being segmented. The principal idea behind the model is to use prior knowledge about the target anatomy and its surrounding structures to constrain the topology of the final segmentation. This guarantees that the structures in the segmentation result are connected to each other (and themselves) in a fashion that respects what we know about the anatomy. The primary advantage of such constraints is that they allow the segmentation process to be highly resilient to noise and artifacts that would otherwise negatively affect the results. For example, if we know that the spinal cord in our images consists of a singular connected cylindrical structure, we can enforce this topologically by constraining the spinal cord in the segmentation to always be a single connected object. As a result, the segmentation becomes more robust to intensity drop-offs or artifacts in the middle of the image that might break the spinal cord segmentation into multiple objects.

In the following sections we provide a brief summary of the TOADS algorithm. Then, we introduce several new elements to generalize the TOADS model for spinal cord segmentation in MRI. Specifically, we describe the constraints we use to construct the spinal cord topology atlas, and how deformable registration is incorporated into this framework to initialize the atlas such that it can account

for the variability of the cord position in the image. This includes an explanation of our approach for maintaining the necessary digital topology of the atlas when applying large registration deformations. Finally, we present an approach for constructing the necessary topology and statistical atlases from a single manual segmentation of the spinal cord.

### 3.2.1 TOADS Overview

A brief overview of the TOADS algorithm is provided in this section. Complete details for the algorithm are available in the original paper presented by Bazin and Pham [57]. The goal of the algorithm is to perform an FCM based intensity classification of an image, while maintaining digital topology constraints on the objects in the segmentation. This is achieved by starting the segmentation from a *topology atlas* that describes the desired topological configuration of relevant objects in the anatomy. The atlas is then evolved to match the target image through a series of homeomorphic growing and thinning steps that guarantee the digital topology between the objects is never broken. This thinning and growing is driven by the FCM centroid(s) and membership(s), with recalculation at each iteration as the segmentation is updated. Bazin and Pham [57] describes the theory behind digital homeomorphism and how to augment the simple point criterion to evolve a segmentation while maintaining digital topology.

In addition to the topology atlas, TOADS also utilized a *statistical atlas* built from a collection of 18 manually generated segmentations of significant brain structures, derived from the IBSR dataset (Worth, 1996). The edge of each structure was smoothed, using a Gaussian kernel, to make a smooth probability map that approximates natural anatomical variations. This statistical atlas provides information for distinguishing adjoining structures with similar intensities.

Given an MR image,  $\mathcal{I}$ , each iteration of TOADS consists of performing a fuzzy segmentation and then updating a topologically consistent segmentation using fast marching. The fuzzy segmentation is obtained by minimizing the energy function,

$$E(u_{jk}^q) = \sum_{jk} \frac{u_{jk}^q}{r_{jk}} \|\mathcal{I}_j - c_k\|^2 + \beta \sum_{l \in N_j, m \neq k} \frac{u_{jk}^q}{r_{jk}} u_{lm}^q + \gamma \sum_{m \neq k} \frac{u_{jk}^q}{r_{jk}} w_{km} p_{jm}^q, \quad (3.1)$$

with respect to a membership function,  $u_{jk}^q$  for each voxel  $j$  in  $\mathcal{I}$ , and each structure  $k$  being segmented. The parameter  $q$  controls the “hardness” or “fuzziness” of the membership functions and is usually set to be two [55].

The three terms on the right side of Eqn. 3.1 can be explained as follows. 1) The first term is a data term that compares the intensity  $\mathcal{I}_j$  at each voxel against the intensity centroids  $c_k$  for each structure, where the differences are weighted by the membership functions for that voxel. 2) The second term enforces the smoothness of the membership functions. 3) The third term controls the influence of the statistical atlas, which provides the prior probability  $p_{jk}$  that a voxel  $j$  begins inside structure  $k$ . These atlas probabilities are weighted by  $w_{km}$ , which are distance measures between the centroids,  $c_k$  and  $c_m$ , of two classes; it is designed to be one when  $c_k = c_m$  and decays to zero as  $\|c_k - c_m\| \rightarrow \infty$ . The

variables  $\beta$  and  $\gamma$  in Eqn. 3.1 are weights on the relative importance of each term, while  $r_{jk}$  takes into account the global and local relationships between structures.

The digitally homeomorphic thinning and growing of the topology atlas is performed using a fast marching approach (Sethian, 1999). The thinning aims to remove errors from misalignment of the atlas to the image by only keeping high membership voxels. Then the growing step expands the skeletally thinned structures until all boundary voxels are in contact. In this manner, the segmentation captures more details of the structure boundaries at each iteration while retaining the topology of the atlas. The algorithm is assumed to converge when either the change in the energy function drops below a suitable threshold or a maximum number of iteration is reached.

### 3.2.2 Extending TOADS for the Spinal Cord

The flexibility of the TOADS algorithm allows the model to be adapted for the spinal cord; however, we must overcome several limitations in the existing framework. First, we must construct a set of topology and statistical atlases that are anatomically meaningful in the context of the spinal cord and have the flexibility to handle all possible fields of view. Unlike brain imaging where the whole brain is usually imaged, spinal cord MRIs tend to have limited fields of view that generally do not cover the entire cord. This results in possible artificial breaks in the topology when the image ends part way through the cord. This needs to be accounted for during both the construction and the initialization of the topology atlas. Second, TOADS assumes the brain images have been skull-stripped, e.g., via [58], prior to running the algorithm. The absence of non-brain tissue allows TOADS to rigidly register the topology atlas directly to the MRI for initialization. This is clearly not possible in our case, since our primary goal is to separate the spinal cord and CSF from the rest of the image. Hence, we must work with the surrounding tissue in the MRI, which makes registering the topology atlas (a segmentation image) to the MRI highly unreliable. In addition, the varied curvature of the spinal cord prevents a rigid, or even affine, transformation from providing an adequate initialization. The following sections will describe our solutions to these two problems.

### 3.2.3 Spinal Cord Topology and Statistical Atlases

The topology atlas serves as the topological rule set for the objects being segmented in our algorithm. In our model for the spinal cord, this atlas only contains three objects: 1) the spinal cord with spherical topology; 2) the CSF with a spherical shell topology; and 3) a “wrapper” object also with a spherical shell topology. The wrapper object serves as a catch-all object for any structures that immediately surround the spinal canal, including the vertebrae and surrounding muscles. Since it encompasses several tissue types, it covers a wide range of image intensities. Its primary purpose is to provide a boundary that prevents the CSF object from extending past the spinal canal. Everything outside

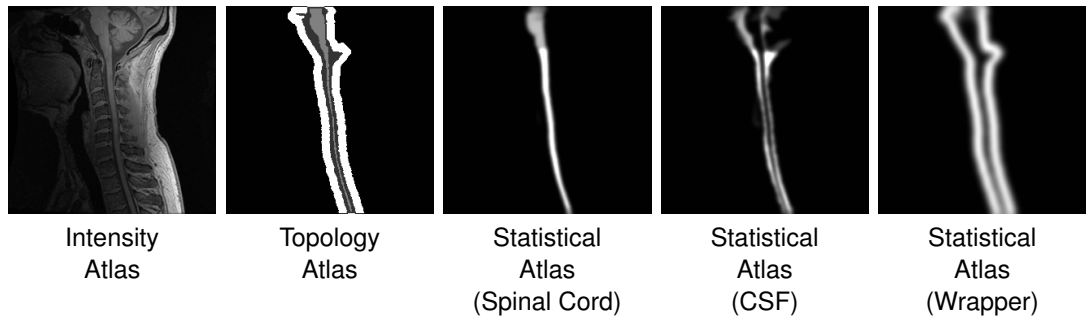


Figure 3.4 An example of the intensity, topology (spinal cord in light gray, CSF in dark gray, and wrapper in white) and statistical atlases constructed from a T1-weighted MRI.

the wrapper object is treated as background. We represent the topological relationships between these objects with just two basic assumptions:

1. The spinal cord is completely surrounded by the CSF.
2. The union of the CSF and spinal cord is completely surrounded by the wrapper object.

Figure 3.4 shows examples of this atlas for a sagittally acquired T1-weighted MRI dataset. We note that in our atlas, the CSF forms a “cap” on the top and bottom of the spinal cord, which is not anatomically correct. This is done because the field of view of the MRI forces a cutoff at the superior and inferior edges of the images. Hence, we must completely cap the ends of the spinal cord object with the CSF object in order to prevent the background and wrapper objects from being connected to the spinal cord. Otherwise, those objects would be allowed to evolve in between the CSF and spinal cord, effectively separating the two objects, which we know should not happen. Similarly, the wrapper object completely surrounds the CSF object to enforce a similar topology. Both of these artificial caps are added outside the field of view and are removed at the end of the algorithm; thus, they do not interfere with the accuracy of the segmentation at the boundaries.

In addition to the topology atlas, a statistical atlas is used to define probabilistic priors on the locations of objects in the topology atlas. This is created by taking multiple spinal cord MR images and deformably registering them to a common target. Manual segmentations of the structures in each MR image are then transformed using the same deformation. This provides an empirical calculation for the probability of each object occurring at each voxel in the target space. The resulting probabilities are Gaussian-smoothed to reduce discrete drop-offs in the atlas [57]. Figure 3.4 shows a statistical atlas for the spinal cord, CSF, and wrapper objects, constructed from five manual segmentations. In Section 3.2.6 we provide an automatic and more efficient approach for constructing both the topology and statistical atlases from only a single manual segmentation.



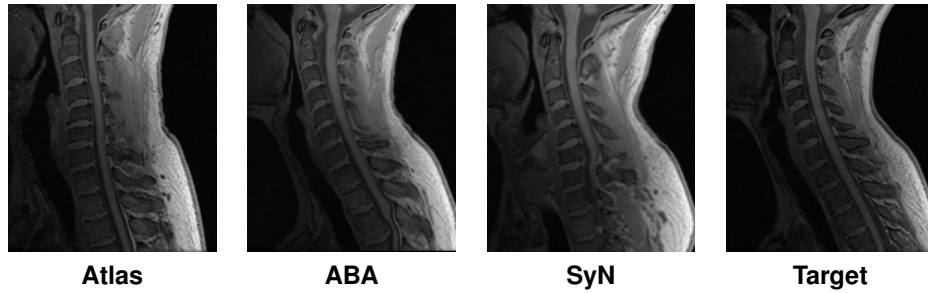


Figure 3.5 Example of registrations between an intensity atlas and a target image using ABA and SyN.

### 3.2.4 Incorporating Deformable Registration Into TOADS

Creating these two spinal cord specific atlases is still not sufficient to directly apply TOADS for spinal cord segmentation. We also need a new way to initialize the atlases, since the original TOADS relies on a rigid initialization, which cannot fully capture the variability of the spinal cord. To address this limitation, we replace the rigid alignment step with a deformable registration. Unfortunately, this replacement results in two new difficulties. First, deformable registration between a segmentation image (the topology atlas) and the MRI is highly unreliable. This is due to the segmentation image containing only a few structures, each with homogeneous intensity, while the MRI includes all the tissue surrounding the spinal cord, and contains noise and artifacts. This makes it extremely difficult to find the correct correspondences between these two types of images during registration. The small size of the spinal cord relative to the entire image also contributes to the difficulty.

Our solution to this is to introduce an *intensity atlas* into the TOADS framework. This atlas is directly associated with the objects in the topology atlas, and in most cases will be the underlying MRI that the topology atlas was constructed from. The goal is to use deformable registration to learn a mapping between the intensity atlas and the MRI being segmented. This learned deformation is then applied to the topology and statistical atlases to serve as their initialization in the algorithm. In this work, we evaluated both ABA (Section 2.3.1) and SyN (Section 2.3.2) to perform this task.

Figure 3.5 shows examples of spinal cord MRI registrations between an intensity atlas and a target image using these two registration algorithms. As expected, we see significant registration errors in parts of the spinal cord. However, they provide sufficient initialization for the TOADS algorithm, which is fairly robust to such errors in the initialization. In Section 3.4.1 we evaluate the effectiveness of both of these registrations algorithms in addition to their impact on our final segmentation.

### 3.2.5 Topology Preserving Atlas Deformation

The second issue with including a deformable registration into the framework is that, in general, such registrations do not take into account the digital topology of the objects being deformed. The complexity of maintaining digital topology during registration is the primary reason why only a rigid alignment

of the topology atlas was used in the original TOADS algorithm, and even then, the transformation had to be applied carefully. Bazin and Pham [57] showed that even simple rotations and/or scaling, which are purely homeomorphic in the continuous sense, are not necessarily homeomorphic in the digital domain. This demonstrates that simply having a homeomorphic (or diffeomorphic) transformation model is not sufficient to preserve digital topology. The only way to guarantee that a registration will produce a digitally homeomorphic transformation is to check the digital homeomorphism criterion at every step of the optimization. This is computationally expensive and becomes highly impractical for higher order registration that can generate complex deformations.

In our earlier work [59], this was addressed by using a technique that can generate a digitally homeomorphic approximation of a deformation field [60]. The technique is applied after a deformation field is found between the intensity atlas and the target image. It starts by resetting the deformation field to zero and then slowly regrowing each deformation vector in the field back to its original value. This creates a series of incremental deformations that are applied to the topology atlas. At every step, the digital homeomorphism criterion is checked to make sure an increment does not break the topology of the atlas. If incrementing a particular deformation vector will cause a topology break, then that deformation is stopped from entirely growing back. This produces an approximation of the deformation field that can deform the topology atlas while maintaining its initial topology. Since this method is applied after the registration is completed, it also has the added advantage of being applicable to any registration algorithm.

In general, this digital homeomorphic approximation of the deformation field is very robust when the deformations are small or the atlas is simple. However, it can potentially introduce considerable segmentation errors when deforming complex topologies over large distances. This is a result of topology deadlocks that can occur, where a set of voxels are stuck in a configuration that prevents them from moving without breaking the object topology. The problem becomes more prominent when working with spinal cord MRI with large and varied fields of view, where the deformations produced by the registration are very large. An example of this is in the thoracic region of the spinal cord where the shape and distance can vary greatly between the atlas and target images. Figure 3.6(b) shows an example of a topology deadlock that can be introduced when approximating such a deformation.

To prevent these errors, we introduce a dynamic approach for initializing the topology atlas. Instead of applying the learned deformation to all three objects in the atlas, we only apply it to the spinal cord object. After the spinal cord object has been deformed, the other two objects are then automatically added back to the atlas by following the topology rules listed in Sec 3.2.3. That is, the CSF object is added to the atlas as a dilation of the spinal cord label, and likewise the wrapper object is added as a dilation of the union of the spinal cord and CSF labels. Transforming and building the atlas *on-the-fly* in this manner greatly simplifies the homeomorphic deformation approximation, thereby allowing us to avoid topology deadlocks that can be introduced during the initial registration step. Figure 3.6(c) shows how initializing the topology atlas in this manner can prevent the deadlock seen before.

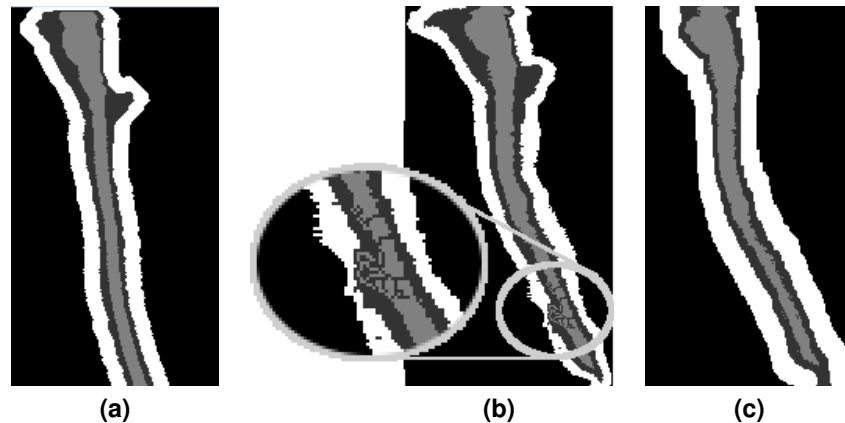


Figure 3.6 Shown is **(a)** the topology atlas (spinal cord in light gray, CSF in dark gray, and wrapper in white) before initializing with a deformation learned from registration, **(b)** an example of a topology deadlock that can occur when initializing the entire topology atlas by a digital homeomorphic approximation of the deformation, and **(c)** the result when only the spinal cord is initialized by the homeomorphic deformation, and the remaining topology atlas is rebuilt dynamically.

We see from the example that initializing the topology atlas in this manner does alter the initial structure of the CSF and wrapper object in the atlas. However, it is important to remember that the role of the topology atlas is mainly to enforce our topology rule set. The initial structure of each object has little effect on the final segmentation, since all the objects are immediately thinned and then grown back to maximize their membership functions during the first iteration. It is more important that the atlas does not start with deadlocks that would prevent it from evolving in this manner.

### 3.2.6 Automated Atlas Construction

A major deficiency with existing methods for spinal cord segmentation is their inflexibility when facing very different datasets, particularly ones not used in the design of the algorithm. For example, in current methods that rely on deformable models [50, 51], the forces used in the algorithm are not immediately applicable for other datasets with different fields of view or MR pulse sequences. Redesigning such forces is time consuming and requires a certain level of expertise and familiarity with the algorithm.

Our introduction of deformable registration into the TOADS algorithm helps address this problem by allowing our atlas to be initialized on a wider variety of data. However, it is still possible for the target image to be so different from the atlas that a proper registration cannot be reasonably achieved. To overcome such situations, we describe an automatic process for generating the necessary topology and statistical atlases from a single manual segmentation of an image from the desired dataset. This is achieved by taking advantage of TOADS's robustness to initialization errors, and the simple topology of the spinal cord.

**Topology Atlas Construction** In the original TOADS paper [57], the topology atlas was constructed by starting from an initial segmentation produced using the statistical atlas, and then manually editing the areas in the atlas that did not follow their assumptions about the topology. Constructing the topology atlas in this manner is not a trivial task. Small errors in the topology can easily be missed or obscured by the orientation the image is being viewed. In addition, the topology of every combination of objects in the image must be checked.

We follow a similar approach for our topology atlas construction by starting from a manual segmentation of our intensity atlas and fixing any topology errors that break our model. However, our task is greatly simplified due to the dynamic initialization approach introduced in Section 3.2.5. Since all the objects in our atlas are dynamically built from just the spinal cord object, we only need to correct the topology for that single object. In addition, since the spinal cord in our model has spherical topology, this correction can be performed automatically using a simple algorithm:

1. Find the largest connected component in the foreground.
2. Set all smaller connected components in the foreground to background.
3. Find the largest connected component in the background.
4. Set all smaller connected components in the background to foreground.

This allows the topology atlas for our method to be constructed quickly and automatically from a single approximation of the segmentation.

**Statistical Atlas Construction** Creating a true statistical atlas from a single manual segmentation is clearly not possible. By definition, such atlases require multiple subjects to empirically estimate the spatial variance of the anatomy. However, we make two observations. First, TOADS does not need a true statistical atlas to produce an accurate segmentation. The statistical prior only serves to provide a rough guideline for where structures lie in the image. Its primary purpose is to provide a prior for different tissues with similar intensities, which is not present in our problem. In our case, the underlying intensity provides the main driving force for the algorithm. Second, as we have shown in Figure 3.5, deformable registration of the spinal cord is often inaccurate. As a result, statistical atlases constructed using such registrations are already fairly unreliable. Rather than representing the spatial variance of the spinal cord, they often just represent the variance of the registration error. This effect can be seen in Figure 3.4, where the inferior ends of the spinal cords are not correctly aligned. Such registration variances are inconsistent across different images, and offer little value for the TOADS optimization. In certain cases, it may even degrade the segmentation result.

Given these considerations, we approximate the statistical atlas by assuming a simple Gaussian distribution spatially around the single manual segmentation. This is equivalent to Gaussian smoothing each structure in the manual segmentation, and normalizing at each voxel. Figure 3.7 shows a visual

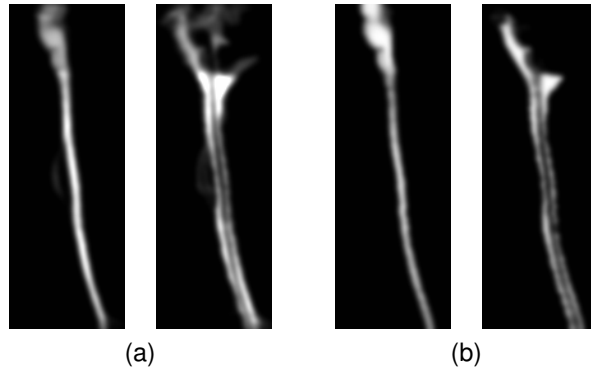


Figure 3.7 Comparison of statistical priors of the spinal cord and CSF constructed using **(a)** the standard registration approach (with five segmentations) and **(b)** a single manual segmentation Gaussian smoothed. A kernel size of  $\sigma = 1$  was used in both cases. Further explanation and details are in Section 3.4.2.

comparison between statistical priors constructed using the standard registration approach (with five segmentations) and our approximation of the atlas using Gaussian smoothing. In Section 3.4.2, we show that approximating the statistical atlas in this manner produces roughly the same accuracy as the standard atlas construction approach, and in certain cases can actually improve the overall accuracy of the final segmentation.

### 3.3 Materials

Our algorithm was applied to two datasets having different population characteristics, MR protocols and scanners, and fields of view.

#### 3.3.1 T1 Cohort

The first dataset used in our experiments consisted of MR images of the brain stem and spinal cord from the C1-T4 vertebrae acquired from seven patients diagnosed with multiple sclerosis (MS). Each image was acquired using a T1-weighted inversion recovery fast spoiled gradient recall (FSPGR) pulse sequence on a 3 Tesla GE Signa scanner (GE, Milwaukee WI) with the following parameters: TR=7.8ms, TE=2.98ms, TI=750ms, and flip angle=16°. The resolution of the acquired images was 1mm isotropic.

#### 3.3.2 MT Cohort

The second dataset used in our experiments consisted of 238 MRIs of the cervical spinal cord, acquired from the C2-C6 vertebrae. The data were acquired from 18 healthy controls (HC) and 220 patients with multiple sclerosis (MS). The scans were performed with a 3 Tesla Philips Intera scanner (Philips Medical Systems, Best, The Netherlands) using body coil excitation and two-element

phased array surface coil reception. The images were magnetization transfer (MT) prepared T2\*-weighted gradient echoes, using an MT prepulse applied at 1.5 kHz off resonance (24 ms, five-lobed Sinc-Gauss pulse with maximum amplitude 9.5 mT), as described in [61]. Other parameters: TR=110 ms, TE=13 ms, flip angle=9°, echo planar imaging factor 3, and SENSE acceleration factor 2. Each image had a through plane resolution of 2.25mm and an in-plane resolution of 0.6 × 0.6mm.

### 3.3.3 Manual Segmentations

All seven images in the T1 cohort were each manually segmented (labeling the spinal cord and the CSF) by two different raters. Twenty images (18 HC, 2 MS) in the MT cohort were similarly segmented by two different raters. Each rater labeled 10 and 14 subjects, respectively, with 4 images in common between the raters.

The image slice numbers corresponding to the C2 and C5 vertebrae were manually identified by a single rater in 146 images in the MT cohort. This subset was used in our statistical analysis in Section 3.4.4 and 3.4.5. Table 3.1 shows the detailed demographic information for this subset.

Table 3.1 Detailed demographic description for the 146 subjects in the MT cohort with manual slice numbers for the C2 and C5 vertebrae (used in Section 3.4.4 and 3.4.5). Key: healthy controls (HC), clinically isolated syndrome (CIS), relapsing-remitting (RR), primary progressive (PP), and secondary progressive (SP).

	HC	CIS	RR	PP	SP
<b>N (Male/Female)</b>	15 (5/10)	5 (2/3)	76 (23/53)	16 (8/8)	34 (12/22)
<b>Age (SD)</b>	39.4 (9.1)	34.8 (9.6)	38.9 (10.5)	53.4 (6.7)	51.9 (7.3)

### 3.3.4 Metrics

We report the accuracy of our method in comparison to human raters by using the Dice coefficient [62],

$$\text{Dice}(H, A) = \frac{2|H \cap A|}{|H| + |A|},$$

for a particular structure (e.g., cord or CSF), where  $H$  and  $A$  are the segmentations generated by the human rater and the algorithm, respectively. The Dice coefficient is a measure of set agreement and is commonly used as a volumetric measure for comparing the quality of automatic vs. manual segmentations. It has a range of [0.0, 1.0], where a value of 1.0 indicates perfect agreement between the algorithm and the manual result, while a score of 0.0 represents no overlap between the two.

## 3.4 Experimental Results

We performed several experiments to demonstrate the performance and applications of our spinal cord segmentation tool. Our first experiment evaluates the accuracy of our algorithm relative to human raters. It also considers the effect of our registration choice for initializing our atlases. We then evaluate the impact of our statistical atlas construction approach, and the size of the Gaussian smoothing kernel used in its construction. Lastly, we performed a large scale evaluation using the MT cohort to establish the robustness and potential clinical relevance of our algorithm.

### 3.4.1 Segmentation Comparison Against Manual Raters

We evaluated our automated segmentation results against the seven images from the T1 cohort and the twenty from the MT cohort that have corresponding manual segmentations. The Dice coefficient was calculated for the spinal cord, CSF, and the union of the two structures (i.e., the spinal canal). For each dataset, we evaluated using either ABA or SyN for initialization. Table 3.2 shows the mean and standard deviation of the Dice coefficient of our results against manual segmentations when initializing with each registration algorithm, and for each cohort.

In general, the algorithm performed better on the MT cohort than the T1 cohort, particularly for the CSF. This can be largely attributed to the better tissue contrast and smaller intensity inhomogeneities in the MT cohort images. These differences can be seen in Figs. 3.8 and 3.9, which show cropped examples of the original MRI, its manual segmentation, and our automatic segmentation results for each cohort. From the figures we see that the automatic results were very similar to the manual segmentations for both cases. However, the automatic results tended to be overall smoother due to the TOADS regularization. Comparing between the two figures, we see that the T1 cohort result had more areas where the CSF was mis-segmented as the spinal cord than in the MT cohort result. This is particularly noticeable in the inferior areas of the T1 image where the intensity inhomogeneity was very strong, and the contrast between the CSF and spinal cord was lower.

The individual accuracy of each registration algorithm was also considered by looking at its ability to transfer the atlas segmentation to the target image through applying the learned deformation from the intensity atlas registration. Table 3.2 shows the Dice coefficient between the transferred segmentation from each registration algorithm and the manual segmentation for the target image. We see from these results that ABA generally performed much better than SyN for both datasets. Hence, it was the only registration algorithm considered in the remaining experiments.

### 3.4.2 Statistical Atlas Construction Parameters

The impact of the two statistical atlas construction approaches described in Secs. 3.2.3 and 3.2.6 was evaluated by repeating our algorithm on five images from each cohort, while using atlases from both approaches with increasing kernel sizes ( $\sigma$ ) for the Gaussian smoothing. In general,  $\sigma$  can be seen

Table 3.2 Evaluation of the CSF, spinal cord ("Cord"), and combined ("CSF + Cord") segmentation results against manual segmentations from two raters (R1 and R2) for the two cohorts (T1 and MT). Shown are the mean (standard deviation) of the Dice coefficient when using just the registration (ABA and SyN) for segmentation transfer, and the final segmentation result from the presented method when using the registration for initialization.

	Registration Only			Final Segmentation		
	CSF	Cord	CSF+Cord	CSF	Cord	CSF+Cord
<b>T1</b>						
ABA vs R1	0.67(0.10)	0.77(0.14)	0.70(0.12)	0.63(0.17)	0.82(0.18)	0.70(0.18)
ABA vs R2	0.65(0.09)	0.75(0.13)	0.68(0.10)	0.63(0.17)	0.77(0.15)	0.68(0.17)
SyN vs R1	0.13(0.11)	0.14(0.13)	0.13(0.11)	0.22(0.12)	0.28(0.18)	0.23(0.14)
SyN vs R2	0.12(0.09)	0.13(0.13)	0.12(0.10)	0.21(0.09)	0.26(0.17)	0.22(0.12)
R1 vs R2				0.81(0.03)	0.89(0.02)	0.84(0.02)
<b>MT</b>						
ABA vs R1	0.73(0.07)	0.83(0.07)	0.76(0.06)	0.85(0.03)	0.91(0.03)	0.88(0.02)
ABA vs R2	0.74(0.04)	0.87(0.01)	0.79(0.03)	0.84(0.02)	0.92(0.01)	0.87(0.01)
SyN vs R1	0.63(0.20)	0.73(0.25)	0.67(0.22)	0.72(0.28)	0.75(0.37)	0.74(0.31)
SyN vs R2	0.63(0.15)	0.70(0.21)	0.66(0.17)	0.82(0.05)	0.89(0.03)	0.85(0.04)
R1 vs R2				0.88(0.01)	0.93(0.01)	0.90(0.01)



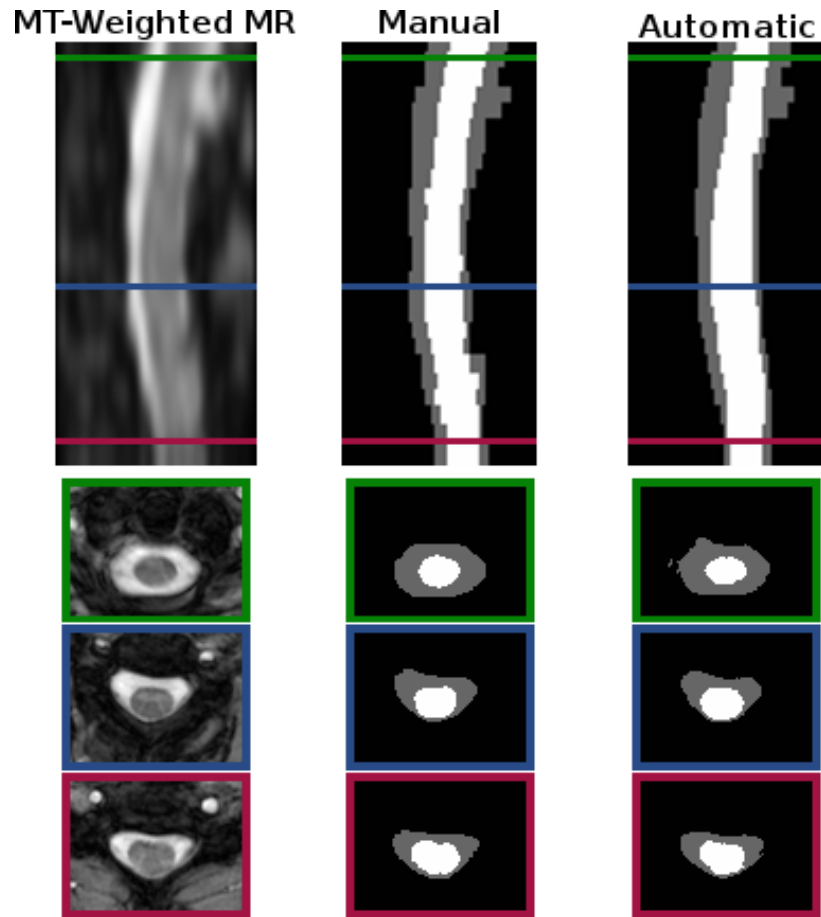


Figure 3.8 Cropped example of a MT-prepared T2\*-weighted MRI segmentation by a human rater in comparison to the result from our algorithm. Shown are one sagittal and three axial views. The colored border around the axial slices denote the respective cross-section within the sagittal image. The Dice coefficient between the shown manual and automatic segmentations are 0.91 for the spinal cord (white) and 0.86 for the CSF (gray).

as a parameter for controlling the capture range of the statistical atlas. A small value should be used if the initialization from the registration is believed to be very accurate and trustworthy. A large value can compensate for bad registrations, but may also cause the method to latch onto the wrong structure or artificially expand the segmentation size. Figure 3.10 shows plots of the mean Dice coefficient between the manual segmentations and the automatic results, for each cohort, when using either the registration approach presented by Bazin and Pham [57] or our single segmentation approach. For both cases, we ranged  $\sigma$  from one to five in increments of 0.5.

From the figure we see that, for the registration approach, the best performance was achieved without any smoothing ( $\sigma = 0$ ). However, for our single segmentation approach, smoothing with  $\sigma = 1$  was necessary to achieve the best performance. In addition, we see that the two approaches had roughly the same performance at their respective optimal configurations, with our single segmentation approach

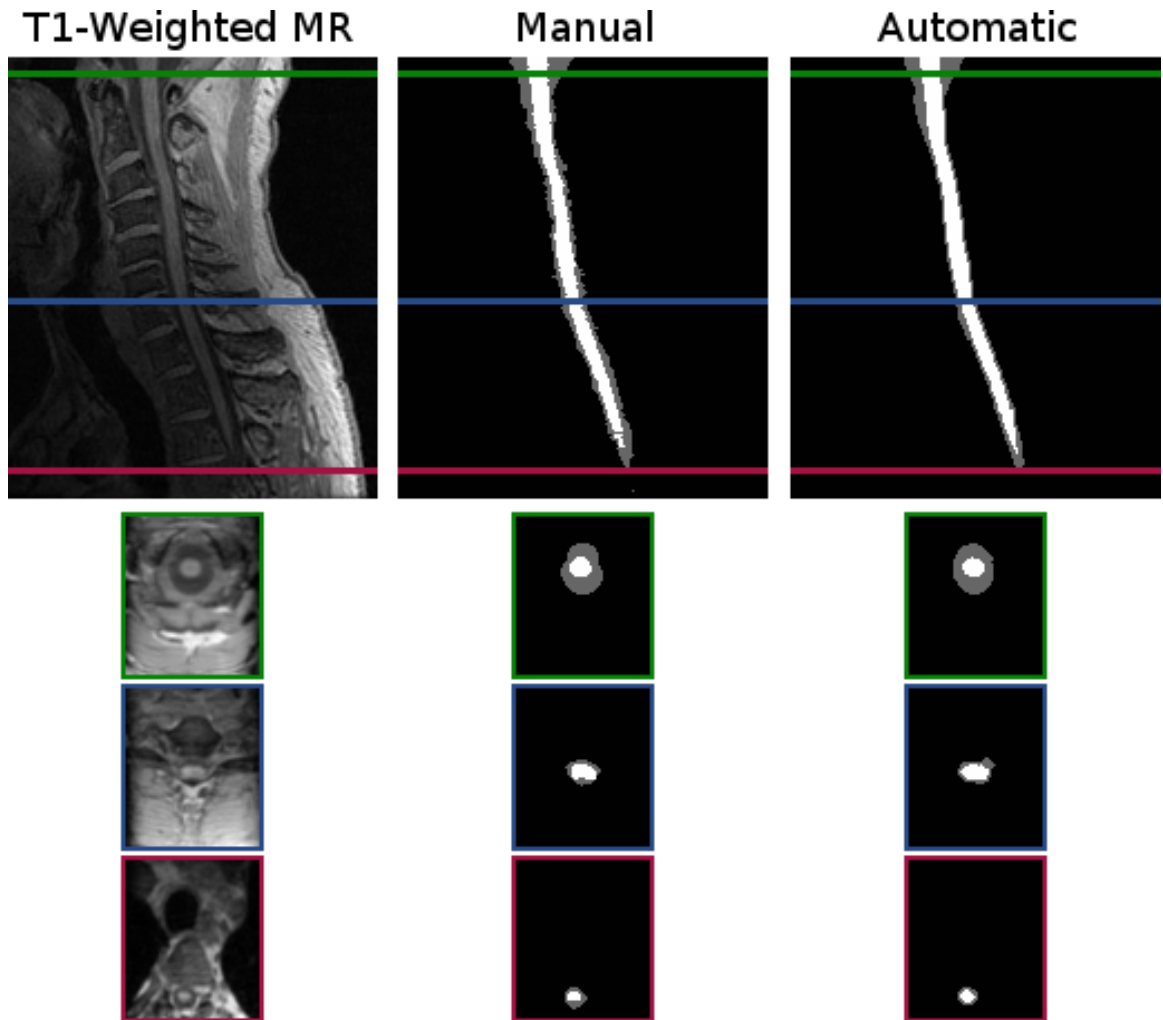


Figure 3.9 Cropped example of a T1-weighted MRI segmentation by a human rater in comparison to the result from our algorithm. Shown are one sagittal and three axial views. The colored border around the axial slices denote the respective cross-section within the sagittal image. The Dice coefficient between the shown manual and automatic segmentations are 0.87 for the spinal cord (white) and 0.73 for the CSF (gray).

performing slightly better in the CSF for the T1 data. For these reasons, we chose to use our single segmentation approach (with  $\sigma = 1$ ) for the experiments in the remaining sections.

### 3.4.3 Robustness in Large Scale Processing

To evaluate the robustness of our method, the entire MT cohort was processed using the presented algorithm. The results were manually inspected for clear failures, which we designated as segmentations with roughly less than 75% spinal cord overlap (by visual inspection). Of the 238 images in the dataset, only eight failures were identified. Figure 3.11 shows axial slices and their segmentation

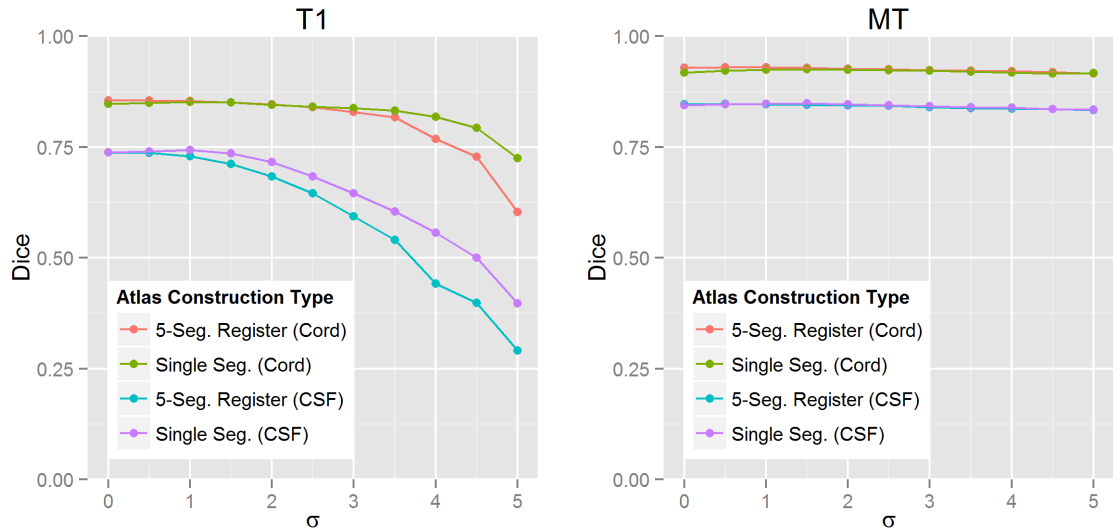


Figure 3.10 Average Dice coefficient between automatic and manual segmentations when using statistical atlases built from the standard registration based approach (using five segmentations) and our single segmentation approach, at different levels of Gaussian smoothing ( $\sigma$ ). The left plot shows the average results for five T1-weighted images, and the right shows the average results for five MT-weighted images.

results for all eight failed cases. For reference, the figure also shows four successful cases from the processing.

All eight failures were primarily due to strong artifacts present in each image. Seven of the cases were a result of motion artifacts that blurred the structures in the images. This caused the intensity for the spinal cord, CSF, and surrounding tissues to have similar means and high variances. This created segmentations where either the entire spinal canal was segmented as a single object, or the various tissues were classified interchangeably.

In the remaining failure, a strong intensity inhomogeneity was present that removed roughly a quarter of the image. This resulted in a very poor registration that translated the initial segmentation far from the spinal cord, which the algorithm could not recover from. We note that while the failures in Figure 3.11 appear to be breaking the topology of the segmentation, it is actually a result of the 2D visualization of the images. In those cases where it appears that an object is in multiple pieces, the object is actually extending from above (or below) the slice.

### 3.4.4 Clinical Relevance

Statistical analysis was performed on the spinal cord volumes produced by our algorithm on the 146 images from the MT cohort that had manually selected slice numbers for the C2 and C5 vertebrae.

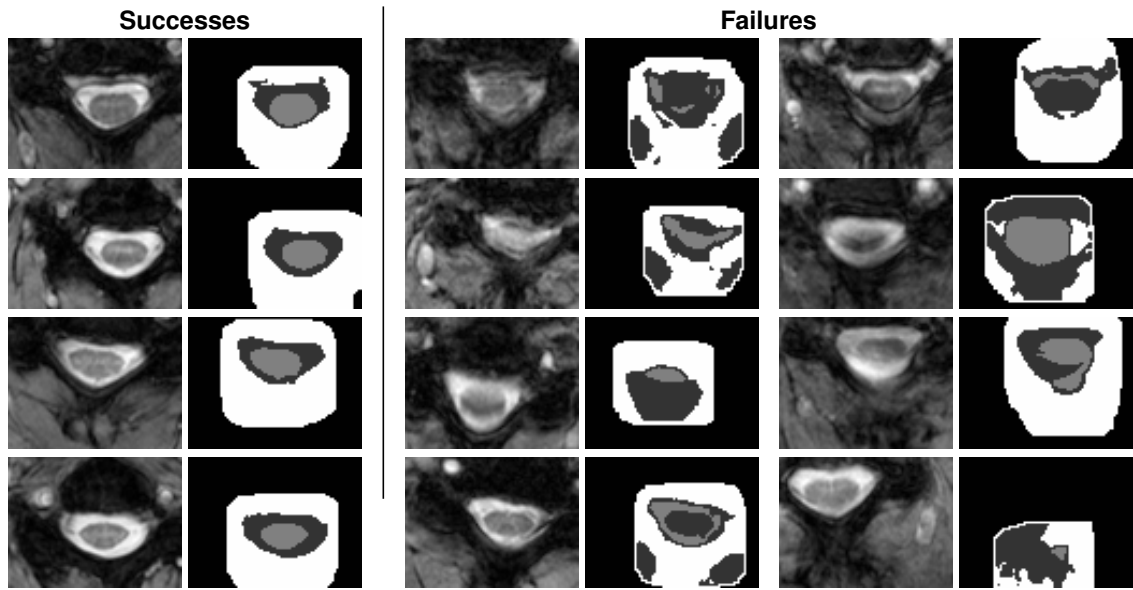


Figure 3.11 Shown are axial slices for four successful segmentations and the only eight failures found when processing the 238 images in the MT cohort with the presented algorithm. For each pair of images, the left shows a crop of the original MRI, while the right shows the respective spinal cord (light gray), CSF (dark gray), and wrapper (white) segmentation results from the algorithm.

For normalization, spinal cord volumes were divided by the length of distance between the C2 and C5 vertebrae, which produces normalized cross section areas [63].

Multivariate linear regression was used to perform age and sex adjusted Student's *t*-tests between the healthy controls (HC) and patients with multiple sclerosis (MS). Pairwise group comparisons were also made between individual subgroups (healthy controls (HC), clinically isolated syndrome (CIS), relapsing-remitting (RR), primary progressive (PP), and secondary progressive (SP)). Table 3.3 shows the mean normalized cord area for each subgroup, and the significance of their difference after adjusting for age and sex. Significant differences were found when comparing healthy controls against the entire MS group ( $p$ -value = 0.042), however significant differences between healthy controls and individual MS subtypes could not be established. Within subtypes, significant differences were found when comparing secondary progressive patients against relapsing-remitting ( $p$ -value = 0.005) and primary progressive ( $p$ -value = 0.011) patients.

For the MS patients, semi-partial correlation was used to evaluate Pearson's correlation coefficients between normalized cord area for both the Expanded Disability Status Scale (EDSS) and disease duration, while adjusting for age and sex. Further correlations were evaluated for the RR, PP, and SP subtypes. The CIS subtype was omitted due to the small number of subjects. Figure 3.12 shows the relationship of normalized spinal cord area with EDSS (top plot) and disease duration (bottom plot), after adjusting the values for age and sex. In each case, the black line shows the relationship for the whole MS group, while colored lines indicate relationships for a particular MS subtype. Moderately weak, but

Table 3.3 Pairwise group comparisons of normalized cord area (mm<sup>2</sup>) between healthy controls (HC) and patients with MS (ALL-MS) and the MS subtypes of clinically isolated syndrome (CIS), relapsing-remitting (RR), primary progressive (PP), and secondary progressive (SP). Shown are the mean and standard deviation of the normalized cord area for each group and the significance (p-values) of the cord area differences between each group pairing, after adjusting for age and sex.

Group Comparisons of Normalized Spinal Cord Area						
	Area (mm <sup>2</sup> )	Pairwise p-Values				
	Mean (SD)	CIS	RR	PP	SP	ALL-MS
<b>HC</b>	88.8 (14.5)	0.411	0.075	0.708	0.101	<b>0.042</b>
<b>SP</b>	68.7 (20.1)	0.826	<b>0.005</b>	<b>0.011</b>		
<b>PP</b>	83.0 (19.2)	0.642	0.976			
<b>RR</b>	81.2 (14.6)	0.779				
<b>CIS</b>	83.1 (11.0)					
<b>ALL-MS</b>	78.2 (17.4)					

significant relationships were found for normalized spinal cord area with both EDSS ( $r = -0.19$ , p-value = 0.03) and disease duration ( $r = -0.23$ , p-value = 0.01) when observing the whole MS group together. No relationship could be established when looking at each MS subtype group individually.

### 3.4.5 Exploratory Study of CSF Volumes

One advantage of our approach over existing methods is the ability to generate segmentations of cerebrospinal fluid (CSF) from the spinal cord image. To our knowledge, no study has been performed that observe the volume of spinal CSF with respect to multiple sclerosis. To demonstrate the potential of such analysis, we provide a basic exploratory study of such a measure. The data and methods used in this analysis is analogous to that used in 3.4.4 for the spinal cord volume. Since there are no clear guidelines for normalizing the CSF volume, we again normalize by the distance between the C2 to C5 vertebrae, producing a normalized CSF area.

Table 3.4 show the mean normalized CSF area for each MS subgroup, and the significance of their difference after adjusting for age and sex. No significant differences were found when comparing healthy controls against the entire MS group. However, several significant differences could be found when comparing against the progressive cases (SP and PP). The pairs where significant differences were found are SP vs. HC (p-value = 0.040), SP vs. RR (p-value < 0.001), and PP vs. RR (p-value = 0.003).

## 3.5 Discussion

We have presented a fully automatic approach for segmenting the spinal cord and cerebrospinal fluid from MRIs. Unlike existing methods, our approach is designed to be highly generalizable to spinal cord images of any field of view or MR contrast. The only criterion necessary for our algorithm is a

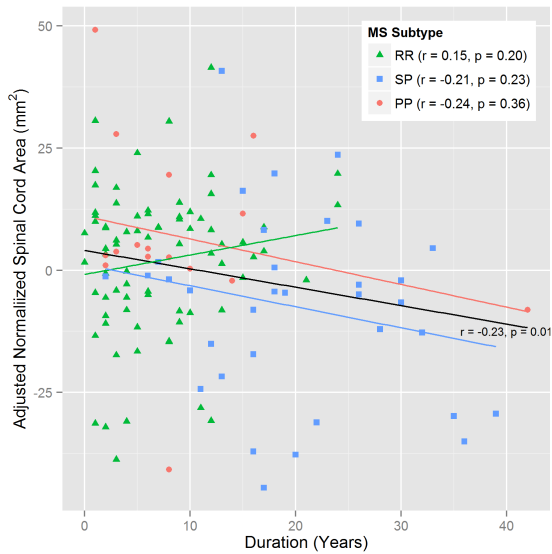
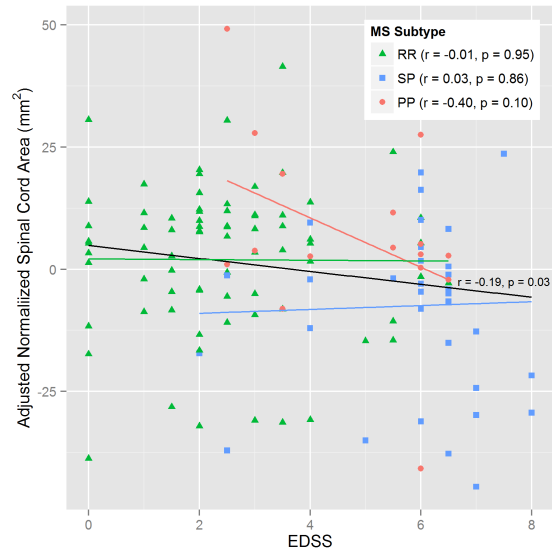


Figure 3.12 Correlation plots showing the relationship between normalized spinal cord area (age and sex adjusted) with EDSS (top) and disease duration (bottom) for MS patients. The black line shows the relationship for all MS patients grouped together. The colored lines indicate the relationship for the specific subtypes — relapsing remitting (RR) in green, secondary progressive (SP) in blue, and primary progressive (PP) in red. The correlation ( $r$ ) and significance ( $p$ ) are given for each line.

Table 3.4 Pairwise group comparisons of normalized CSF area (mm<sup>2</sup>) between healthy controls (HC) and patients with MS (ALL-MS) and the MS subtypes of clinically isolated syndrome (CIS), relapsing-remitting (RR), primary progressive (PP), and secondary progressive (SP). Shown are the mean and standard deviation of the normalized CSF area for each group and the significance (p-values) of the CSF area differences between each group pairing, after adjusting for age and sex.

Group Comparisons of Normalized CSF Area						
	Area (mm <sup>2</sup> )	Pairwise p-Values				
	Mean (SD)	CIS	RR	PP	SP	ALL-MS
HC	128.3 (24.8)	0.850	0.304	0.472	<b>0.040</b>	0.141
SP	168.4 (45.5)	0.128	< <b>0.001</b>	0.999		
PP	173.7 (65.1)	0.990	<b>0.003</b>			
RR	136.3 (28.3)	0.207				
CIS	119.9 (33.5)					
ALL-MS	148.6 (42.5)					

reasonable registration between an atlas and the image being segmented. For data where such a registration is unreliable (i.e., if the images differs too greatly from the provided atlas), we have presented a fast and automatic approach for generating a suitable atlas using a single manual segmentation of an image from the desired dataset.

### 3.5.1 Accuracy and Robustness

Our evaluations show that the presented method achieved high accuracy and robustness when compared against manual segmentations from two independent raters for two datasets with very different image characteristics. From Table 3.2, we see that on average our algorithm achieved a 0.91 Dice coefficient for the spinal cord and 0.85 Dice for the CSF when working with the MT-prepared T2\*-weighted data. Such values are remarkably high, especially considering that the Dice coefficient is very sensitive to errors when the structures being compared are long and thin. In general, the overlap achieved by our algorithm on this data is on par with inter-rater accuracy for the spinal cord, and slightly lower for the CSF.

The T1-weighted data, which had a much larger field of view, proved to be more challenging. On average our algorithm achieved a 0.80 Dice coefficient for the spinal cord and 0.63 Dice for CSF when ran on this data. Overall, these values are still considered fairly high for Dice coefficients, particularly for the spinal cord. The lower CSF performance can be largely attributed to the strong field inhomogeneities in the image, making it difficult to distinguish it from surrounding tissues.

Our large scale evaluation on 238 images shows that the method is highly robust. Only eight failures were produced over the entire dataset, and all of them were a result of intense artifacts that rendered the images unusable. In the context of a clinical trial using the same MR-sequence, these example failures can provide a preliminary basis in the acquisition protocol for determining when an image contains too much artifact or distortion to be used with our algorithm. The overall quality and robustness

of our results can be largely attributed to the topology constraint, which allows the algorithm to better handle the noise and artifacts that are prevalent in spinal cord MRIs.

### 3.5.2 Results Comparison Against Existing Literature

To our knowledge, none of the currently existing automatic MRI spinal cord segmentation algorithms [49, 50, 51] nor the data used in their evaluation are openly available for download. This prevents a direct comparisons against their methods. However, compared against the Dice overlap reported in their work, on average our algorithm performed very favorably. Namely, Koh et al. [49] achieved an average Dice of 0.70 when compared against two human raters on 52 images. In the alternative approach presented by Koh et al. [50], they gained marginal improvements with an average Dice overlap of 0.71. In Mukherjee et al. [51] a direct overlap validation was not performed, and instead only values for area correlation between manual raters was presented.

Our statistical results can be compared against several works studying the relationship between normalized spinal cord area and MS. The most relevant of these is the work presented by Horsfield et al. [46] where a semi-automated approach was used to perform similar analysis as those we have presented in Section 3.4.4.

Our analysis when comparing normalized spinal cord volume between healthy control and MS patients produced several conclusions that are consistent with that reported by Horsfield et al. [46]. Namely, we showed significant differences between healthy controls and the entire MS group (p-value = 0.042), significant differences between relapsing-remitting and secondary progressive subtypes (p-value = 0.005), and a lack of significant difference between relapsing-remitting MS and healthy controls (p-value = 0.075). In addition, our correlation analysis with EDSS showed a moderate, but significant relationship between normalized spinal cord area for the whole MS group, but a lack of significant correlation when comparing against individual MS subtypes. Both of these results match those presented by Horsfield et al. [46].

There are, however, two results that are distinct. Horsfield et al. [46] found no significant relationship between normalized spinal cord volume and disease duration, while we found a small but significant correlation for the relationship. Horsfield et al. [46] also found significant differences between HC and SP, while we did not (p-value = 0.101). This may be due, in part, to our control group being smaller and considerably younger than our SP group. Hence, first adjusting for age and sex might have removed any noticeable effect.

Finally, our analysis of CSF volume shows a capability that, to our knowledge, has not been expressed before. Our exploratory analysis on normalized CSF area showed a considerable trend of higher CSF in the progressive MS subtypes (SP and PP), with significant differences being found after adjusting for age and sex when compared against the RR subtype (p-value < 0.001 and p-value = 0.003, respectively), and between healthy controls and SP (p-value = 0.040).



### 3.5.3 Adapting to New Data

One major advantage of our algorithm is its ability to be quickly and automatically adapted for use with different spinal cord MRI data. We have designed a topology rule set that allows the topology atlas to be automatically constructed by correcting the topology of the spinal cord object and dynamically generating the remaining structures. We have also provided an alternative approach for approximating the statistical atlas, which does not require multiple manual segmentations to be registered to a common target. In Figure 3.10 we show that if we Gaussian smooth a single manual segmentation, we can create an statistical atlas that provides roughly the same level of performance as an atlas generated through the standard registration approach. In addition, for the T1-weighted data, we see that this approach can actually be superior to the standard approach, particularly in the CSF. The main advantage, however, is that now only a single manual segmentation is necessary to construct all the atlases required for our algorithm to be entirely tailored to a specific dataset.

One important note regarding our algorithm's adaptability is that the performance of the method is still heavily reliant on the data being used. As we see from the T1 and MT results, the performance is not guaranteed to be preserved when changing between MR-sequences. Our algorithm provides a rapid way to adapt to new datasets, which can be particularly useful if no existing method is available for such data. However, further evaluations are still necessary when applied to new MR-sequences and fields of view to ensure that the performance is preserved after the adaptation.

## 3.6 Summary

MRI of the spinal cord presents many challenges, such as noise and artifacts, which makes automatic segmentation of such data a difficult task. In this chapter we have presented a topology preserving approach that combines deformable registration with the TOADS algorithm, and have shown its effectiveness for both accuracy and robustness. For MS, our algorithm removes the dependency on manual or semi-automatic delineations of the spinal cord, therefore enabling studies on larger datasets to be performed more efficiently and for less cost. In addition, as spinal cord imaging rarely has a standard field of view or MR contrast, we assume that the atlases provided with our algorithm are not optimal for every type of spinal cord MRI data. Hence, we have gone to great length to allow our algorithm to be easily adaptable. This includes providing an automatic and reliable way to construct the necessary atlases from a single manual segmentation, and designing our framework so that it is not tied to a particular registration algorithm for initialization. This provides users with an option to use the registration algorithm that performs best on their particular given dataset. Lastly, our incorporation of deformable registration into TOADS has implications that extend beyond our application in the spinal cord. Allowing the atlas to be initialized deformably enables the model to be used with many other anatomical structures. The main limitations are only that successful registrations can be performed on the structure and the topology of the structure is simple enough to be constructed adaptively. In addition, new intensity and statistical

atlases would need to be built for the specific structure. This work described in this chapter has been presented in conference [59] and journal [64] form.

## Chapter 4

# Spinal Cord DTI Pipeline With Distortion Correction

### 4.1 Introduction

Diffusion weighted (DW) imaging is a MR modality that is used to image the diffusion process of water in tissues [65]. Since cellular membranes and fibers constrict the movement of water, observing a tissue's diffusion process can provide information on its structural pathway and orientation [66]. This is particularly useful in the spinal cord, because its primary function as a transmission pathway results in highly structured white matter tracts that traverse its entire length. As a result, diffusion is highly anisotropic in the spinal cord. In MS, observing changes to this anisotropy can provide potential insight on disease processes, and reveal damage to the neurons that may not be evident from structural imaging.

However, DW imaging by itself is insufficient to properly analyze the diffusion's anisotropy. To study such properties, diffusion tensor imaging (DTI) is required, where six or more DW directions are used to estimate a diffusion tensor at each voxel in the image [67]. The eigenvectors for this tensor provide information on the primary directions that diffusion is occurring in the voxel. The eigenvalues,  $\lambda_1$ ,  $\lambda_2$ , and  $\lambda_3$  (ordered largest to smallest), for these vectors tell us the length of each axis and the shape of the diffusion.  $\lambda_1$  is referred to as the *parallel diffusivity* ( $\lambda_{\perp}$ ) and describes the diffusion along the principle axis. The average of the two smaller eigenvalues is known as the *perpendicular diffusivity* ( $\lambda_{\parallel}$ ),

$$\lambda_{\parallel} = (\lambda_2 + \lambda_3)/2, \quad (4.1)$$

and describes diffusion perpendicular to the principle axis.  $\lambda_{\parallel}$  is often used to quantify how restrictive the surrounding membrane is to diffusion. The average of all three eigenvalues is known as the *mean diffusivity*,

$$MD = (\lambda_1 + \lambda_2 + \lambda_3)/3, \quad (4.2)$$

and can be used as a measure of total diffusion in the voxel. Lastly, *fractional anisotropy*,

$$FA = \sqrt{\frac{1}{2} \frac{\sqrt{(\lambda_1 - \lambda_2)^2 + (\lambda_2 - \lambda_3)^2 + (\lambda_3 - \lambda_1)^2}}{\sqrt{\lambda_1^2 + \lambda_2^2 + \lambda_3^2}}}, \quad (4.3)$$

is used to quantify the degree of anisotropy at the voxel. Together, these measures offer insight on the orientation and shape of the underlying cellular structure in the tissues being imaged.

In this chapter we present a pipeline for calculating these diffusion metrics from DW images of the spinal cord. Our approach is an extension of the CATNAP [68] pipeline presented for brain DTI processing. Our main improvement to the pipeline is the introduction of a constrained deformable registration to address susceptibility distortions in the images. To facilitate this we also introduce an approach for automatically matching the fields of view between the DW images and a structural magnetization transfer (MT) weighted MR image, which allows the registration to correct the distortions more reliably. These improvements allowed the pipeline to produce more accurate DTI measures, which enabled two studies by our clinical collaborators relating these measures with clinical measures of sensorimotor function and disability levels in MS.

## 4.2 Methods

### 4.2.1 Adapting CATNAP for the Spinal Cord

Our spinal cord DTI processing pipeline is adapted from the Coregistration, Adjustment, and Tensor-solving, a Nicely Automated Program (CATNAP) pipeline [68], designed for brain DTI processing. The CATNAP pipeline consists of four main operations. First it uses rigid registrations to correct for motion misalignment between each DW direction image and a structural image. It then corrects the gradient direction information for each DW image by rotating each direction using the transformation matrix from the rigid registrations. Using the corrected DW images and gradient information, it then computes the diffusion tensors using a log-linear minimum mean squared error (LLMSE) approach [69]. Finally, it calculates the DTI measure (FA, MD, etc.) from the computed tensors.

The main challenge of adapting CATNAP for the spinal cord is that susceptibility distortion is much more prominent in the spinal cord than the brain. Susceptibility distortions occur because different types of tissue acquire different degrees of internal magnetization when under the static magnetic field from the MRI scanner. At tissue interfaces the contrasting internal magnetizations cause local dephasing and frequency shifts, which results in signal loss and incorrect mapping of the intensities (generally in the phase-encode direction). These errors are exacerbated in DW imaging, because single-shot, echo planar imaging (EPI) sequences are required to increase the acquisition speed [70].

The largest susceptibility distortion generally occurs at tissue-air or soft tissue-bone interfaces. In brain MRI, these types of interfaces are mostly located away from the brain, which is separated from the skull by cranial CSF and the meninges. Hence, susceptibility distortions mostly only affect regions

near the upper respiratory tract, such as areas of the frontal lobe and cerebellum. The effect is often not significant and can sometimes be left unaddressed, such as in the original CATNAP pipeline. However, for the spinal cord, susceptibility distortions cannot be ignored. The vertebrae surrounding the spinal cord is in such close proximity that susceptibility distortions have significant and visually noticeable effects on almost the entire spinal cord in DW images. This is particularly true for images of cervical spinal cord, where the air in the trachea can cause additional distortions. DTI measures calculated from these distorted images are noisy and generally unreliable for analysis.

#### 4.2.2 Correcting EPI Susceptibility Distortions Using Constrained ABA

To address susceptibility distortion in the spinal cord, we use ABA (Section 2.3.1) to register between the DW images and a structural MT image, which doesn't use an EPI sequence and is less affected by susceptibility distortion. The two modalities, acquired from the same person, must share an underlying physical anatomy. Hence, geometric differences between the image must be caused by the distortion in the EPI sequence. By using the DW image as the source image and the MT image as the target, the registration can solve for this distortion as the deformation between the two images.

In our approach, only the  $b_0$  ( $b = 0$ ) image from the DW images is used in the registration. The  $b$ -value indicate the amount of influence diffusion processes have on the image intensities. Hence when the  $b$ -value is equal to zero, the DW image is uninfluenced by diffusion processes and therefore represents a structural image. However, the image is still acquired using an EPI sequence, which means it is affected by the same distortions as the other DW images. This allow the  $b_0$  image to serves as a good reference for the geometric differences between the modalities, while not complicating the registration with the intensity changes from diffusion processes. Once the deformation is learned between the  $b_0$  and MT images, the same field is applied to the other DW images to correct their distortion.

Since we know the susceptibility distortion is mostly concentrated in the phase-encode direction (which we designate as the  $y$ -direction), we limit the deformation  $v$  to be constrained entirely to that direction. This changes Eqn. 2.16 for ABA to be

$$v(\mathbf{x}) = \mathbf{x} + \begin{bmatrix} 0 \\ \sum_i w_i \Phi(\|\mathbf{x} - \mathbf{c}_i\|) \\ 0 \end{bmatrix}, \quad (4.4)$$

where the RBFs are only built and optimized in that single direction. Figure 4.1 shows an example of this distortion correction in an axial slice of the spinal cord. We see that the large geometric compression in the original  $b_0$  image was corrected through this process. This type of registration-based distortion correction approach has been proposed previously for solving the same problem in brain diffusion images [71, 72].



Figure 4.1 An axial slice of a  $b_0$ , diffusion weighted spinal cord image before and after correcting for susceptibility distortion by registering to a MT-weighted image from the same subject.

### 4.2.3 Automatic Field of View Matching

One difficulty with using a registration based distortion correction approach is that the initial alignment between the  $b_0$  and structural image plays an important role in the final result. This can be problematic because the structural image does not always contain the same field of view (FoV) as the DW images. Due to the small size of the spinal cord, registrations tend to be error prone when the FoVs are not matched. The extra surrounding tissues in the larger FoV make it difficult to find the correct correspondences to perform the alignment, especially when distortion is present.

To address this problem we present an automatic FoV matching algorithm, which aligns the center of the spinal cord in each image and crops both images to the same FoV. To find the spinal cord center in each image, we use a multi-atlas segmentation approach to locate a rough bounding box around the spinal cord. This is done by using a set of manually segmented  $b_0$  and MT images as atlases, and performing registrations from each atlas to their respective modality in the target image. For each atlas, this gives an approximation of the spinal cord location in each image. Using majority voting, we combine the results from each atlas and then crop each image to a fixed dimension centered around the detected spinal cord.

Figure 4.2(a) shows an example of the possible field of view differences between a  $b_0$  image and a MT spinal cord image from the same subject. Figure 4.2(b) shows the same images after our FoV matching. We see from the images that the MT image contained a considerably larger FoV with additional surrounding structures that are not present in the DW image. By matching and reducing the FoV to focus on just the spinal cord, we removed areas of the image that can pull the registration algorithm away from solving the distortions within the spinal cord itself.

Figure 4.2.3 shows the full DTI pipeline after our FoV matching and distortion correction improvements. The pipeline is implemented as a JIST [73] layout, which can be used to automatically process large datasets.

## 4.3 Quality Assurance

Both the CATNAP pipeline and the application of ABA to solve for EPI distortion has been described and validated in previous work. Our main focus is to ensure that our adaptations of the pipeline,

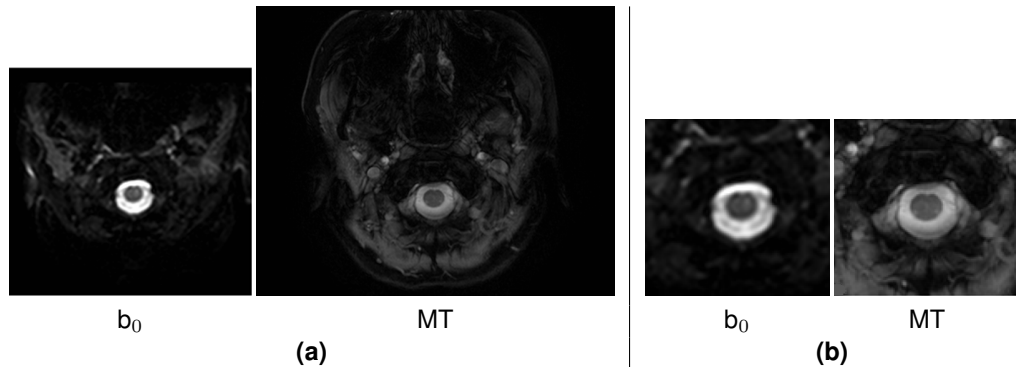


Figure 4.2 Example of field of view (FoV) differences between a diffusion  $b_0$  image and a MT image from the same subject. All images show the same axial slice of the spinal cord from the same subject. **(a)** shows the original FoV for each image, and **(b)** shows the image pair after matching and cropping the FoV to the spinal cord.

distortion correction, and FoV matching for spinal cord data will lead to robust DTI calculations that can be used to analyze spinal cord MS data. To validate this process, a clinician trained in analyzing spinal cords MRIs was asked to perform a qualitative analysis of our DTI results. The pipeline was used to fully process 130 cervical spinal cord DW MRIs (16 directions, single shot EPI, parallel imaging factor=2, TR=4,727 ms, TE=63 ms), consisting of images from both healthy volunteers and MS patients. For each result, the clinician checked the overall registration accuracy relative to the structural target, and the FA colormap result relative to expected tract orientation and structure. Overall, the DTI results were found to be much more reliable after the distortion correction.

Figure 4.4 shows a comparison of FA colormap results from our pipeline when using and not using the distortion correction. The color at each voxel in the map indicate the direction of the anisotropy and the intensity indicates the FA. We see that by using the distortion correction, the calculated FA is generally less noisy in the spinal cord. This is particularly evident in the CSF, which we expect to be isotropic and have an FA close to zero.

## 4.4 Clinical Relevance

The spinal cord DTI measures calculated using our pipeline has facilitated two subsequent studies of MS. First, the pipeline was used to explore spinal cord DTI measure differences between healthy control subjects and MS patients [74]. The study analyzed cervical spinal cord MRIs from 129 MS patients (74 RRMS, 36 SPMS, and 19 PPMS) and 14 healthy controls (HC). Student's t-test were performed to compare between MS and HC subjects. Significant ( $p$ -value  $< .05$ ) differences were found for MD, and  $\lambda_{\perp}$  between the two groups. A comparison between relapsing and progressive MS patients was also performed, which showed significant differences in MD, FA,  $\lambda_{\perp}$  between the subtypes. In addition, multivariate linear regression was used to study relationships between the DTI measures and three

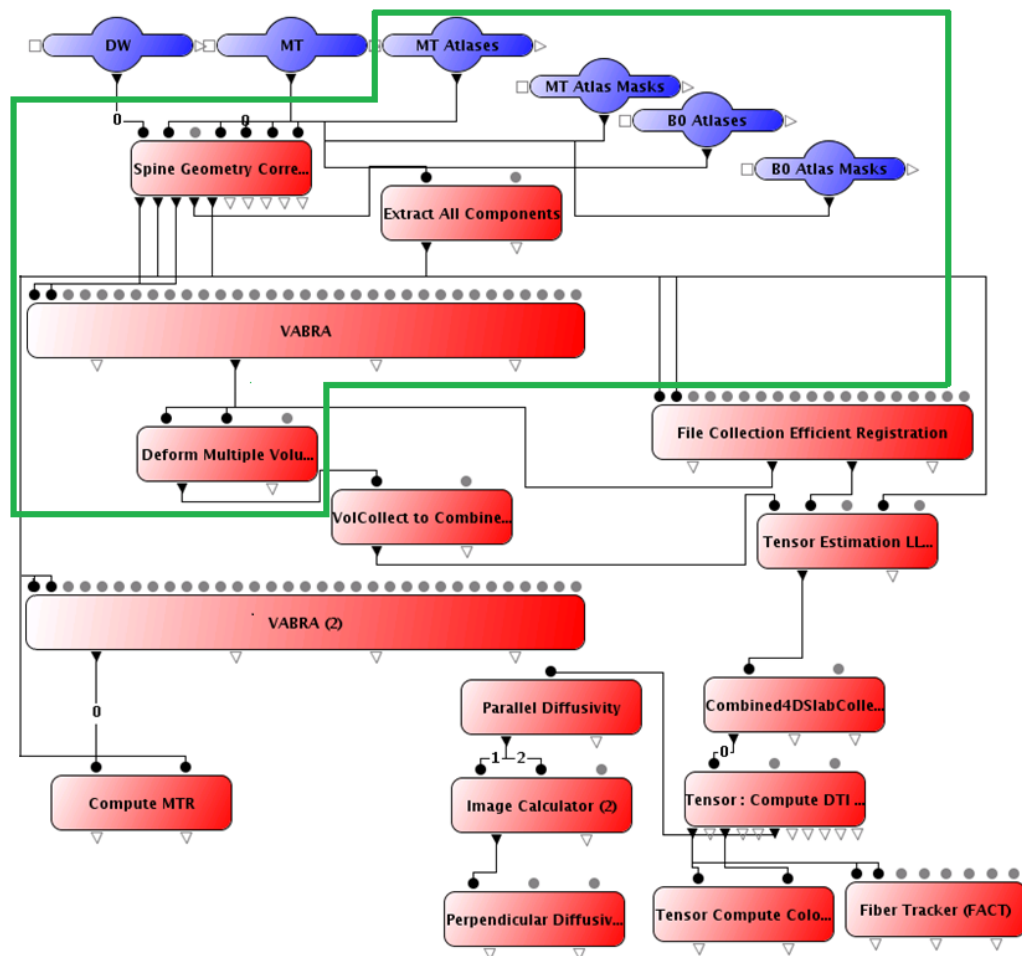


Figure 4.3 JIST layout showing our full spinal cord DTI processing pipeline. Boxed in green is our improvement to the original CATNAP pipeline, which includes our field of view matching and distortion correction approaches.

clinical measures (hip flexion strength, vibration sensation threshold, and Expanded Disability Status Scale [EDSS]) from the patients. All three analyses were performed after adjusting for age, sex, spinal cord cross-sectional area, and brain parenchymal fraction. Three DTI measures (MD,  $\lambda_{\perp}$ , and  $\lambda_{\parallel}$ ) showed significant (at an  $\alpha$  level of 0.05) independent associations with the hip flexion strength measure, and FA trended towards independent association ( $p$ -value = 0.07) with it. For vibration sensation threshold, FA showed significant independent associations and  $\lambda_{\perp}$  trended towards an independent association ( $p$ -value = 0.06). Lastly, FD, MD, and  $\lambda_{\perp}$  showed significant independent associations with EDSS. These associations help demonstrate the utility of using the diffusion measures to study structural-functional relationships in MS.

The second study used spinal cord diffusion measures to discriminate different levels of disability in MS patients [75]. In the study, spinal cord DTI data from 124 MS patients were subdivided into groups



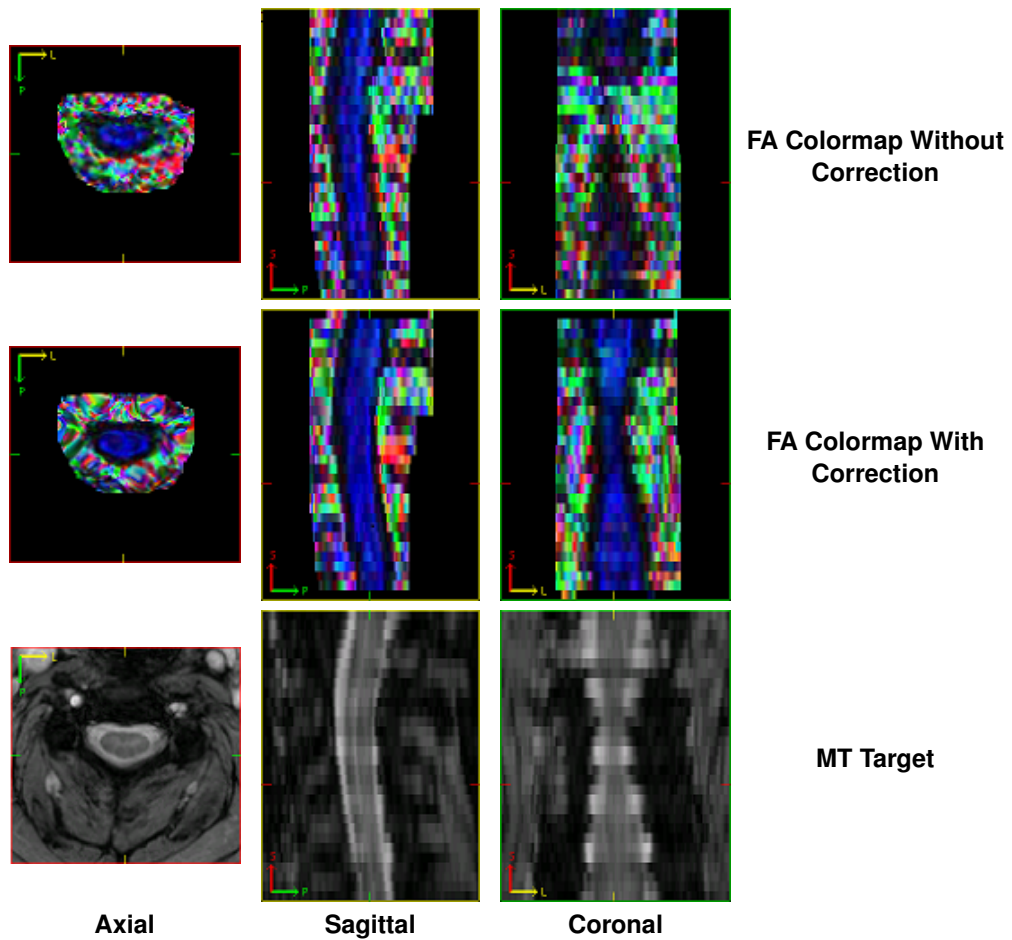


Figure 4.4 Tri-planar views of FA colormap results from our pipeline when using and not using the distortion correction. Also shown is the structural MT image used as the correction target.

with low (EDSS < 6) and high (EDSS  $\geq$  6) levels of disability, and groups with low ( $\leq 2$ ) or high ( $> 2$ ) lesion counts. The results showed that regardless of lesion count, patients with high levels of disability had significantly (at an  $\alpha$  level of 0.05) higher measures of diffusivity (MD,  $\lambda_{\perp}$ ) and lower measures of anisotropy (FA) than patients with low levels of disability. These changes in diffusion measures suggest additional damage to the underlying microstructure in the spinal cord, and are consistent with interpretations of additional spinal cord damage in patients with higher disability. The results suggest that spinal cord DTI measures can be used as a quantitative score that discriminate disability in MS patients. This can be useful for therapeutic purposes, such as analyzing drug effectiveness in clinical trials.

## 4.5 Summary

We have presented improvements to the CATNAP pipeline to provide a fully automatic spinal cord DTI processing pipeline that can correct for susceptibility distortion, and robustly handle differences in

fields of view between the DW images and a structural MT image. Our pipeline was used to automatically process over one hundred datasets, and the results were validated by a trained clinician. The improved pipeline allows for more accurate and robust DTI analysis, and has enabled two studies by our clinical collaborators that showed significant relationships between the diffusion metrics we produce and clinical measures of sensorimotor function and disability levels in MS. These results suggest that the DTI metrics from our pipeline can potentially be useful for monitoring disease progression and disability.

## Chapter 5

# Deformable Registration in Retinal OCT

### 5.1 Introduction to Retinal Optical Coherence Tomography

The human *retina* is an isolated part of the CNS located on the posterior surface inside the eye. Ganglion cells extend from the optical nerve, and form several layers, which together can detect, interpret and transmit visual information to the brain. At the center of the retina is the *macula*, which provides the most acute vision in the retina. It is characterized by the *fovea*, a dip in the retinal layers where the ganglion cells part away to allow for a high density of cones and rods, which provides an increase in visual acuity. Figure 5.1(a) shows an illustration of the retina, macula, and fovea.

Figure 5.2 shows a list of the names and abbreviations for the primary layers of the retina. These layers are organized according to function. The two most anterior layers (towards the top of the image) consist of the axons (retinal nerve fiber layer) and cell bodies (ganglion cell layer) of the ganglion cells, which transmit visual signals to the brain. The next two layers (inner plexiform and inner nuclear layers) consist of the amacrine, bipolar, and horizontal cells, which help integrate signals from multiple photoreceptors, and transmit the signal to the ganglion cells. The next four layers (outer plexiform, outer nuclear, inner segment, and outer segment layers) form the parts of the photoreceptors cells, which convert light into neural signals. Finally, the retinal pigment epithelium is a pigmented cell layer that absorbs light, provides nutrients for the photoreceptors, and controls the homeostasis in the subretinal space.

As part of the CNS, the retina is also affected by MS. Several studies have shown retinal layer degeneration with disease progression [76, 77, 78] and the presence of retinal pathology in MS patients [79]. Studying the retina can help address and prevent visual disabilities due to the disease. In addition, the retina can be observed through the pupil which is faster, cheaper and more convenient to

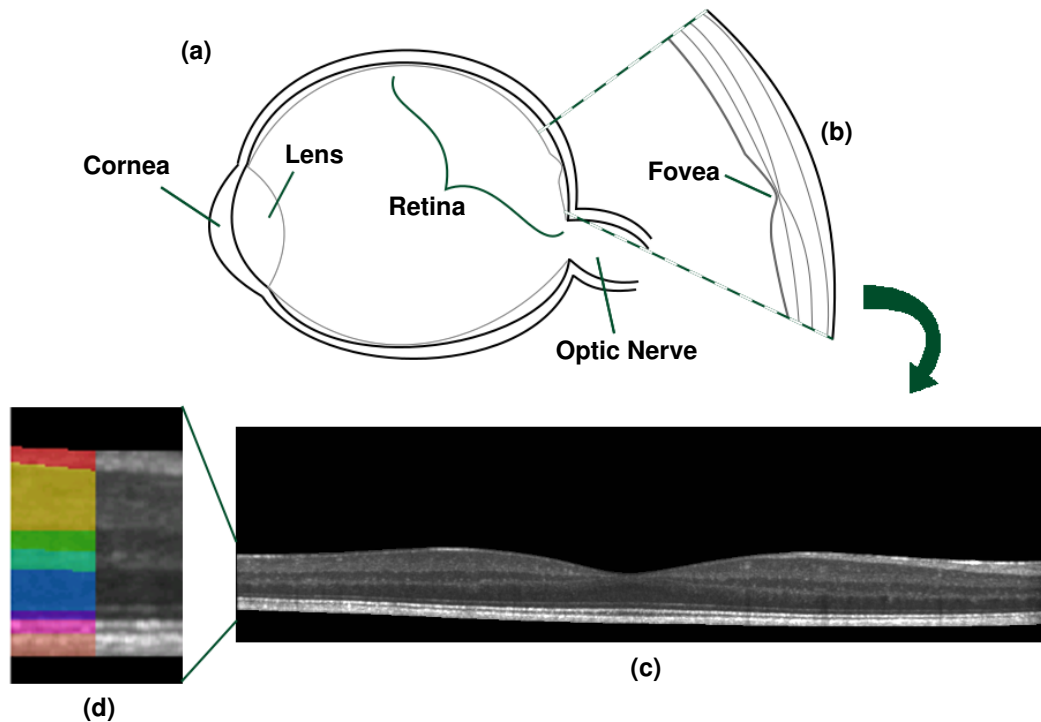


Figure 5.1 Shown is a diagram of **(a)** the eye with **(b)** the macula zoomed in. **(c)** shows an example of a macular OCT image slice (B-scan) and **(d)** shows a partial segmentation of the retinal layers in the OCT. See Figure 5.2 for the names of each layer.

image than other areas of the CNS, such as the brain or spinal cord. Hence, better understanding of the effect MS has on the retina can provide a better way to monitor and observe disease progression.

One challenge when studying the retina is that the individual layers are very thin. Most conventional imaging instrumentations, such as CT, MRI, or ultrasound, cannot image at resolutions that will differentiate the layers. To acquire 3D images of the retinal layers, the current practice is to use optical coherence tomography (OCT), which allows micrometer ( $\mu\text{m}$ ) resolution imaging by measuring the optical scattering properties of tissues. The OCT scanner sends near-infrared light through the cornea, and then records the intensity and timing of the reflections as the light hits the tissue. Different tissues have different reflection properties, hence a beam of light penetrating the tissues will return a signal profile with varying intensities that correspond to the different retinal layers. This one-dimensional acquisition is referred to as an *A-scan*. Sweeping the light beam laterally in a line and collecting multiple *A-scans* forms a two-dimensional image slice known as a *B-scan*. Figure 5.1(c) shows an example of an OCT B-scan of the macula. Each vertical column in the image is an *A-scan*. By acquiring multiple uniformly spaced *B-scans*, the OCT scanner is able to form a full 3D image of the retina.

While automated and semi-automated methods for analyzing and segmenting retinal layers in OCT have been introduced regularly over the past decade [80, 81, 82, 83, 84, 85], there has been very little development of image registration methods for OCT. Existing works are restricted almost exclusively to rigid registrations [86, 87, 88, 89, 90, 91], which are generally inadequate for the retina, since the differences between retinal layers from different subjects (or even the same subject over time) cannot be

Name	Abbr.	
Retinal nerve fiber layer	RNFL	■
Ganglion cell layer and Inner plexiform layer	GCL+ IPL	■
Inner nuclear layer	INL	■
Outer plexiform layer	OPL	■
Outer nuclear layer	ONL	■
Inner segment	IS	■
Outer segment	OS	■
Retinal pigment epithelium	RPE	■




Figure 5.2 Names and abbreviations for the primary layers of the retina, and their structure as shown on an OCT image.

fully represented by such a low-dimensional model. To capture these differences, an affine or deformable registration is necessary.

Excluding our own preliminary work [92], only three other algorithms have been reported that apply a nonlinear deformable model to register retinal OCT data. Gibson et al. [93] presented a method that segments and extracts the optic nerve head surface from the OCT image, and then registers the surfaces using a combined surface and volumetric registration. The method was validated by comparing the overlap of the optical nerve head after the registration. Antony et al. [94] introduced a method where the surface between the inner and outer segments of the photoreceptor cells are used with a thin-plate spline to correct for axial artifacts. Lastly, Zheng et al. [95] presented a segmentation approach that uses SyN (Section 2.3.2) to aid in segmentation. The method uses approximate segmentations of the retinal layers to divide the image into regions, and then registers each region individually with training data to estimate a more accurate segmentation. Of these three methods, only Gibson et al. provided an inter-subject registration that allows for the construction of a normalized space and population analysis. The other two methods primarily used the registration internally to aid their distortion correction and segmentation algorithm. All three of these deformable registration methods required a segmentation of the OCT data to guide the registration algorithm. This requirement restricts the registration accuracy to that of the segmentation. Since OCT segmentations only provide information about the positions of layer boundaries, these registration algorithms are potentially inaccurate within the segmented regions.

There are a number of generic volumetric registration algorithms (most of which were developed for brain image registration) that can be applied to OCT data. However, our investigations have found that such algorithms are unreliable when applied to the whole OCT image, without separating and registering individual layers as in Zheng et al [95]. Figure 5.3 shows two OCT images and the results of registering a source image to a target image using SyN and DRAMMS [96] with default settings.

The lack of deformable registration tools for retinal OCT can be attributed to several factors. First, OCT (particularly spectral-domain OCT) is a relatively new modality in comparison to other medical imaging modalities such as magnetic resonance imaging (MRI), computed tomography, and ultrasound. Hence, the demand and necessity for algorithms and techniques designed for OCT images is fairly recent. Second, there are a number of characteristics inherent to OCT images which make adaptation and

development of existing registration algorithms challenging. These characteristics include poor signal-to-noise ratio (SNR) in comparison to other imaging modalities, which makes it difficult for intensity based methods to find correct correspondences. The data is often extremely anisotropic, where the gap between the B-scans can be upwards of 30 times larger than the resolution within each B-scan. This is generally not compatible with the regularization inherent in most transformation models in existing algorithms, and also creates significant challenges when performing interpolation. Third, the geometry of OCT images are not well defined between different subjects. The A-scans in the images are generally represented parallel to each other, while physically they should be fanning outwards from the center [97]. Since this geometry is specific to the optics of each individual's eye, it is unclear how transformations between retinal OCT images should be performed, particularly when deforming across different A-scans. Finally, the high resolution of OCT images create a large data size that poses a computational challenge. In the examples shown in Figure 5.3, each algorithm took on average 8–10 hours to run; this is significantly longer than for a standard MR brain registration, which takes just over an hour using the same algorithms. Together, these traits lead to relatively poor performance when applying existing approaches directly to retinal OCT images. The successful development of deformable image registration techniques for OCT can offer the ability to greatly enhance our understanding of the complex interplay of macular degeneration with MS from a population perspective.

In this chapter, we present a deformable image registration approach designed specifically for macular OCT images. The approach begins with an initial translation to align the fovea of each subject, followed by a linear rescaling to align the top and bottom retinal boundaries. Finally, the layers within the retina are aligned by a deformable registration using ABA radial basis functions (Section 2.3.1). The algorithm was validated using manual delineations of retinal layers in OCT images from a cohort consisting of healthy controls and patients diagnosed with MS. We show that the algorithm overcomes the shortcomings of existing generic registration methods.

We demonstrate the utility of our registration algorithm for studying MS by performing several population based analysis techniques that are regularly used in other imaging modalities. First, macular scans from a population of healthy control subjects were used to create a macular stereotaxic space (also known as a *normalized space*), which serves as a standard reference space for comparing between different subjects. Such a space directly enables a number of advanced analytic techniques such as voxel based morphometry (VBM) [12], which allows the exploration of local tissue composition differences between two populations, and has seen extensive use in analyzing functional and structural differences in the brain [98, 99].

Our second application of the deformable registration was to register segmentations of the retinal layers from healthy control subjects to the normalized space in order to create statistical atlases for the retinal layers. These atlases can be used as prior knowledge for segmentation algorithms (such as in our approach for the spinal cord in Section 3.2.3), and can also provide a basic reference for normal retinal variance, similar to standard growth charts.

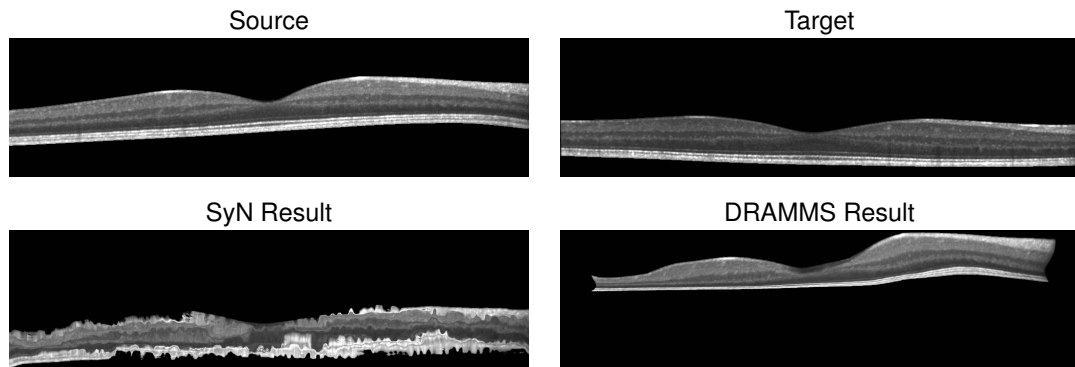


Figure 5.3 The top row shows B-scans from two OCT images used as the source and target. The second row shows example results when using the default settings for two generic deformable registration algorithms, SyN [6] and DRAMMS [96], to register the source image to the target.

Our final application of our algorithm was to study localized volumetric changes between populations by using the Regional Analysis of Volumes Examined in Normalized Space (RAVENS) [4, 13] method. The technique uses the deformations learned from each subject registration to compute the local expansions and contractions of tissue volume relative to the normalized space, and can be used to generate visualizations, called RAVENS maps, of the difference between two populations. In our analysis this technique enabled 3D local investigation of layer volume changes in MS, which was not possible from solely examining layer thickness calculations from segmentation results.

## 5.2 Methods

### 5.2.1 Initial Preprocessing

Prior to performing the OCT registration, our method requires two initial preprocessing steps that are applied to the OCT images. First, in order to reduce intensity outliers and develop a compatible scale for intensity comparison, we apply an intensity normalization process to each OCT volume. Second, we estimate and mask the images to the retinal boundaries by locating the anterior boundary of the RNFL (*inner limiting membrane* [ILM]) and the posterior boundary of the RPE (*Bruch's membrane* [BrM]), which both also serve as landmarks for our affine registration step. The following subsections will briefly summarize these two steps. Both techniques have been used with success in previous work for layer segmentation [85], where more detailed explanations can be found. The OCT images shown in our figures have all been normalized and masked using these two techniques.

**Intensity normalization** Our deformable registration algorithm is based on intensity differences between the source and target images. Hence, we require that the images have similar intensity ranges, and that the values observed in a particular tissue type should be consistent across populations of images.

However, OCT data often shows considerable intensity variability. Even B-scans within the same volume often have very different intensity ranges which cannot be attributed to tissue differences. Possible causes of this are (1) the automatic intensity rescaling performed by the scanner, which can be skewed by high intensity reflection artifacts, and (2) the automatic real-time averaging performed by the scanner, which can result in a specific B-scan undergoing more averaging, creating differences in its dynamic range.

To address these issues, we perform intensity normalization using a straightforward linear contrast stretching on each B-scan independently. Intensity values in the range  $[0, I_{\max}]$  are linearly rescaled to  $[0, 1]$ , with values larger than  $I_{\max}$  being capped at the maximum. The cutoff,  $I_{\max}$ , is determined robustly by first median-filtering each individual A-scan within the same B-scan with a kernel size of 15 pixels (58  $\mu\text{m}$ ), and then setting  $I_{\max}$  as 5% larger than the maximum intensity in the median filtered image.

**Retinal boundary detection and fovea localization** Our next preprocessing step is estimating and masking the images to the top and bottom boundaries of the retina, which are defined by the ILM and BrM, respectively. These retinal extents are found in the following manner. Each B-scan is independently Gaussian smoothed ( $\sigma = 3$  pixels which is  $\sigma_{(x,y)} = (17, 12)$   $\mu\text{m}$ ), followed by an image gradient computation along each A-scan using a Sobel kernel. In each A-scan, the two largest positive gradient values that are more than 25 pixels (97  $\mu\text{m}$ ) apart are taken as initial estimates of either the ILM or the inner segment (IS) outer segment (OS) boundary. We estimate the BrM, by searching up to 30 pixels (116  $\mu\text{m}$ ) below the IS-OS boundary for the largest negative gradient. These boundary estimates are refined by comparing to the median filtered collection of the gradients, and then Gaussian smoothing the result. Using this detection, we mask out non-retinal material and approximate the location of the fovea as the superior point of the thinnest portion of the retina within a search window at the center of the image.

## 5.2.2 Image Registration Method

For our OCT registration algorithm, we use the same framework presented in Section 2.2.1, where we estimate a transformation  $\mathbf{v}$  that maps corresponding locations between a source image  $\mathcal{S}(\mathbf{x}')$  and a target image  $\mathcal{T}(\mathbf{x})$ . As before,  $\mathbf{x}' = (x', y', z')$  and  $\mathbf{x} = (x, y, z)$  describe 3D coordinates in the source and target image domains,  $\mathbb{D}_{\mathcal{S}}$  and  $\mathbb{D}_{\mathcal{T}}$ , respectively, and  $\mathcal{S}(\mathbf{x}')$  and  $\mathcal{T}(\mathbf{x})$  are the intensities of each image at those coordinates. For our OCT images, we assign the  $x$ ,  $y$ , and  $z$  axes as the lateral, through-plane, and axial directions, respectively. This makes A-scan lines parallel to the  $z$  axis and B-scans as images parallel to the  $xz$ -plane.

As described in Section 5.1, the two major challenges of retinal OCT registration are (1) the image voxels tend to be highly anisotropic, and (2) the physical geometry of the image is not properly defined by how the A-scans are presented in the OCT. The former makes regularization and interpolation difficult, if not infeasible, for images with large B-scan separations. The latter obfuscates our ability to apply a sensible deformation that respects the physical space being imaged. This is particularly problematic



when attempting to apply a deformation that crosses multiple A-scans. For example, a deformation parallel to the  $x$  or  $y$  axes in the OCT image is actually curved in physical space. The amount of curvature depends on the fanning of the A-scan during the acquisition, which depends on the optics of the eye being imaged. Such information is often not acquired with the OCT, which makes the actual deformation applied in the physical space ambiguous.

To address these concerns, we impose strong restrictions on the class of transformations our registration is allowed to estimate. In the  $x$  (lateral) and  $y$  (through-plane) directions, we permit only discrete translations such that A-scans from the source always coincide with A-scans in the target (except for missing scans at the boundaries). This removes the need to interpolate intensities between two A-scans or two B-scans. Non-rigid transformations are only allowed in the  $z$  (axial) direction and will be constructed as a composition of individual (A-scan to A-scan) affine and deformable registration steps. This will permit accurate alignment of the features in each A-scan, including the retinal layers.

Our overall registration result is the composition of three steps: a 2D global translation of the whole volume (using discrete offsets only), a set of 1D affine transformations applied to each A-scan, and a set of 1D deformable transformations applied to each A-scan. These transformations are learned and applied in stages and then composed to construct the total 3D transformation  $\mathbf{v}$ . Let  $\mathbf{r}$  represent the 2D global translation, and let  $\mathbf{a}_{i,j}$  and  $\mathbf{d}_{i,j}$  represent, respectively, the 1D affine and 1D deformable transformations applied to the A-scan indexed by the discrete  $x$  and  $y$  coordinates,  $m = (i, j)$ . We can write the total transformation as  $\mathbf{v}(\mathbf{x}) = \mathbf{r} \circ \mathbf{a}_m \circ \mathbf{d}_m(\mathbf{x})$ , where it is assumed that  $\mathbf{x}$  belongs to the A-scan indexed by  $m$ . The deformed source image in the target space is then given by

$$\tilde{\mathcal{S}}(\mathbf{x}) = \mathcal{S}(\mathbf{r}(\mathbf{a}_m(\mathbf{d}_m(\mathbf{x})))), \quad \forall \mathbf{x} \in \mathbb{D}_{\mathcal{T}}. \quad (5.1)$$

In the following sections we present the methods used to carry out these steps.

**2D global translation** The goal of the 2D global translation is to align the source such that its fovea is aligned with the same A-scan as the fovea in the target image. Let the positions of the foveae in the source and target images be denoted by  $\mathbf{f}_S$  and  $\mathbf{f}_T$ , respectively. These locations are found using the approach described in Section 5.2.1, which forces them to be located within A-scans in the two images. The rigid transformation is therefore described by

$$\mathbf{r}(\mathbf{x}) = \mathbf{x} - \mathbf{t}, \quad (5.2)$$

where

$$\mathbf{t} = \begin{bmatrix} (\mathbf{f}_S)_x - (\mathbf{f}_T)_x \\ (\mathbf{f}_S)_y - (\mathbf{f}_T)_y \\ 0 \end{bmatrix}. \quad (5.3)$$

The notation  $(\mathbf{f}_S)_x$  and  $(\mathbf{f}_S)_y$  denote the  $x$  and  $y$ -components of  $\mathbf{f}_S$ , and likewise for  $(\mathbf{f}_T)_x$  and  $(\mathbf{f}_T)_y$ . Figure 5.4(a) shows an example of a result after applying just this rigid 2D foveal translation to the source image.

**1D affine transformation** The 1D affine transformation step assumes that the foveae are aligned and will now consider each A-scan separately. The goal is to find the 1D affine transformation that matches the ILM and BrM boundary locations (both found in Section 5.2.1) between each pair of foveal aligned A-scans in the source and target images. Since there are two landmarks and two unknowns in a 1D affine transformation, the solution can be written in closed form. For each A-scan  $m$  the ILM and BrM boundaries are scalar locations along the A-scan. We refer to these as  $\mathbf{i}_{S,m}$  and  $\mathbf{b}_{S,m}$  for the source image and  $\mathbf{i}_{T,m}$  and  $\mathbf{b}_{T,m}$  for the target image, respectively. The 1D affine transformation for that A-scan is then given by

$$\mathbf{a}_m(\mathbf{x}) = F_m \mathbf{x} + \mathbf{t}_m, \quad (5.4)$$

where

$$F_m = \begin{bmatrix} 1 & 0 & 0 \\ 0 & 1 & 0 \\ 0 & 0 & r_m \end{bmatrix}, \quad (5.5)$$

and

$$\mathbf{t}_m = \begin{bmatrix} 0 \\ 0 \\ \frac{\mathbf{i}_{S,m} + \mathbf{b}_{S,m}}{2} - r_m \left( \frac{\mathbf{i}_{T,m} + \mathbf{b}_{T,m}}{2} \right) \end{bmatrix}. \quad (5.6)$$

The scale factor,  $r_m$ , is calculated from the ILM and BrM locations for each A-scan using

$$r_m = \frac{(\mathbf{b}_{S,m} - \mathbf{i}_{S,m})}{(\mathbf{b}_{T,m} - \mathbf{i}_{T,m})}. \quad (5.7)$$

We refer to the combination of the rigid translation step and this collection of 1D affine transformations at each A-scan as our A-OCT registration. Figure 5.4(b) shows the resulting image after applying this step to the foveal aligned result.

**1D deformable transformation** Following the A-OCT registration, the next step in our algorithm is to use a 1D deformable registration to further improve the alignment of the retinal layers. Unlike the 1D affine registration, where the transformation can be represented as a matrix, the deformable transformation  $\mathbf{d}_m$  for each A-scan  $m$  is a free-form mapping at each  $\mathbf{x}$  with the restriction that the deformation must be smooth and can only occur along the A-scan ( $z$ ) direction. In this registration,  $\mathbf{d}_m$  is modeled as a

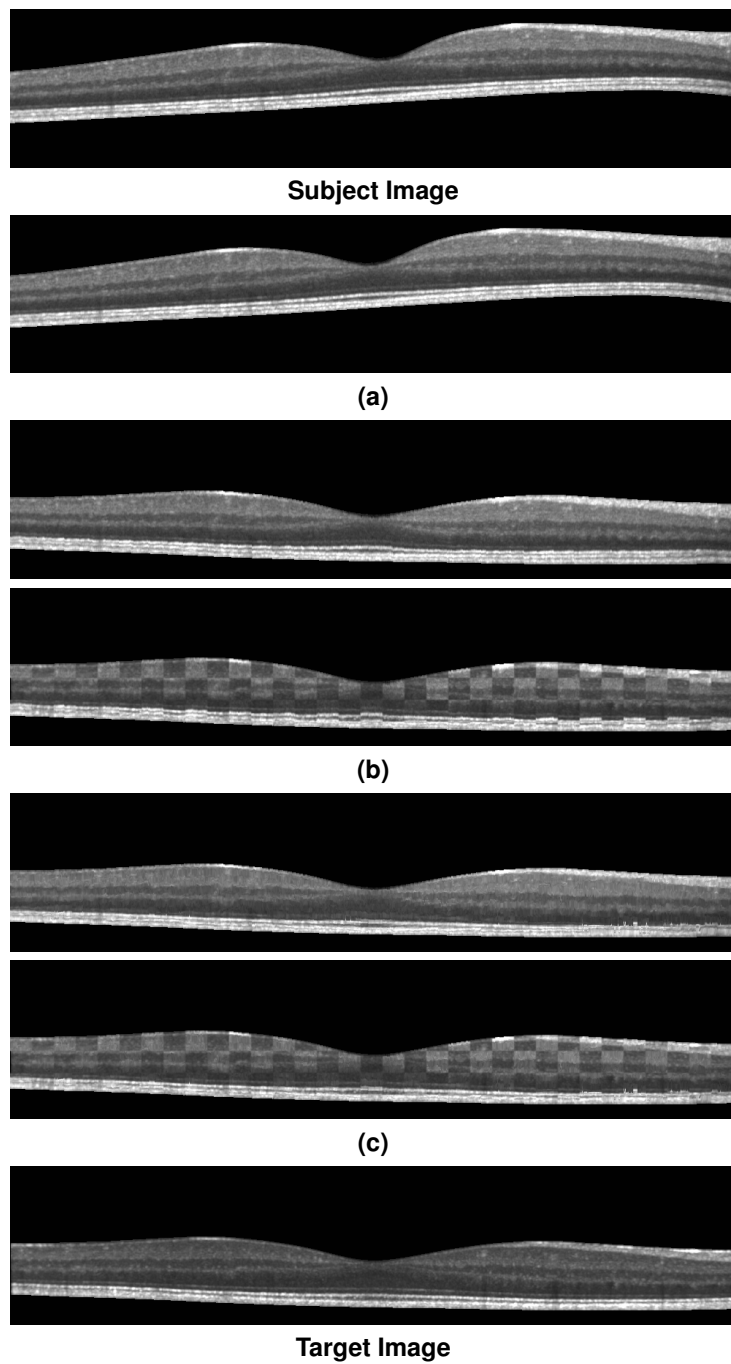


Figure 5.4 Shown are the outputs at each step of the registration algorithm, from the source image  $S$  at the top, to the results of the registration after **(a)** the rigid alignment to the fovea, **(b)** the affine alignment of the A-scans and **(c)** the deformable registration. The target image  $T$  is shown at the bottom for reference. The bottom figures in **(b)** and **(c)** show checkerboard comparisons between each result and the target image.

summation of radial basis functions (RBFs),  $\Phi(\mathbf{x})$ , using

$$\mathbf{d}_m(\mathbf{x}) = \mathbf{x} + \sum_i c_i \Phi(\mathbf{x} - \mathbf{x}_i), \quad (5.8)$$

where  $c_i$  and  $\mathbf{x}_i$  determine the size and center of each RBF, respectively. For  $\Phi(\mathbf{x})$ , we choose the same RBF as presented for ABA [5], except with the deformation restricted only to the  $z$  direction:

$$\Phi(\mathbf{x}) = \begin{bmatrix} 0 \\ 0 \\ \phi\left(\frac{\|\mathbf{x}\|}{s}\right) \end{bmatrix}, \quad \text{where } \phi(r) = (1-r)_+^4 (3r^3 + 12r^2 + 16r + 4), \quad (5.9)$$

for  $(1-r)_+ = \max(1-r, 0)$ , which has support  $s$ . This RBF has several beneficial properties such as smoothness, positive definiteness, and compact support. In addition, Rohde et al. [5] showed that given the correct constraints on the size of each RBF,  $\mathbf{d}_m$  is guaranteed to be homeomorphic. A homeomorphic deformation field allows the deformation to preserve the topology of the image and prevent folding and tearing of the underlying anatomy in the image.

To solve for  $\mathbf{d}_m$ , the algorithm uniformly places the RBFs along the A-scan and then iteratively minimizes the SSD energy function

$$E_m^{\text{SSD}} = \sum_{\{\mathbf{x}|(x,y)=m\}} (\mathcal{T}(\mathbf{x}) - \mathcal{S}_{(\text{A-OCT})}(\mathbf{d}_m(\mathbf{x})))^2, \quad (5.10)$$

which describes the intensity difference between the target image and the A-OCT result deformed by the current estimate of  $\mathbf{d}_m$ , across a particular A-scan.

One disadvantage of optimizing the deformation field between only pairs of A-scans is that it can lead to discontinuities in the total deformation. It also ignores potentially useful neighboring information that can aid the optimization. To address this, we introduce a regularization term,

$$E_m^{\text{Reg}} = \sum_{\substack{r=-R \\ r \neq 0}}^R \sum_{\{\mathbf{x}|(x,y)=m+(r,0)\}} \frac{1}{|r|} (\mathcal{T}(\mathbf{x}) - \mathcal{S}_{(\text{A-OCT})}(\mathbf{d}_m(\mathbf{x})))^2, \quad (5.11)$$

where  $R$  is a parameter that determines how many adjacent A-scans, in the same B-scan, to use in the regularization. The current deformation  $\mathbf{d}_m$  is applied at each adjacent A-scan  $(m + (r, 0))$  and then the function checks the SSD error produced by that deformation relative to the target image. Since we expect adjacent A-scans to have similar deformations, if a deformation at  $m$  causes large errors in adjacent neighbors, then that deformation is heavily penalized. A weight term is included to reduce the contribution of comparisons made further away from  $m$ , since we expect the penalty to be less applicable with distance.

We make two notes regarding this regularization term. First, the deformations of the adjacent A-scans with  $\mathbf{d}_m$  are only used for the optimization of the deformation at the current A-scan. The deformations are not applied permanently to the adjacent A-scans. When the algorithm moves on to estimate a deformation at those adjacent A-scans, a new deformation is estimated. Second, the cost function does not regularize across B-scans, which follows our premise that the large separation between B-scans provide poor correspondences for the registration. Naturally, for data that do not suffer from this limitation, this regularization can be easily extended to use multiple B-scans as well.

The two energy terms are summed ( $E^{\text{SSD}} + E^{\text{Reg}}$ ) to produce our total cost function, which we minimize at each A-scan to estimate  $\mathbf{d}_m$ . Brent's 1D line search optimization method [100] is used to perform this minimization. After evaluating  $\mathbf{d}_m$  at each A-scan, we have all the transformations required to create the final registration result,  $\tilde{\mathcal{S}}$  from Eq. 5.1, which represent the source image registered to the target domain. Figure 5.4(c) shows an example of this final result. We refer to the combination of all three registration steps as our D-OCT registration.

### 5.2.3 Constructing A Normalized Space Using Deformable Registration

The construction of a normalized space for the analysis of a population of subjects is an important application of deformable registration. The normalized space is a common target space to which all images in a group of subjects are registered. This allows spatial correspondences between the subjects to be observed and analyzed together as a population. Often, an average atlas is constructed for this purpose, where the atlas represents the average anatomy of the population. Constructing such an atlas and using it as a normalized space via deformable registration is a well studied topic in brain MRI analysis. A number of methods have been proposed for creating such a space [101, 102, 103]. In generating our normalized space, we follow the method presented in [101] where the average atlas is found by iteratively registering each subject to an estimate of the average atlas, and then adjusting the atlas such that the average of all the deformations is closer to zero. In Section 5.5.1 we use this approach with our deformable OCT registration algorithm to construct an average atlas of the macular using OCT from 40 healthy volunteers.

### 5.2.4 Regional Analysis of Volumes Examined in Normalized Space

The ability to construct a normalized space opens up numerous existing techniques for analyzing images from a population perspective, such as voxel based morphometry [12], statistical deformation models [104], tissue density maps [4], disease classification [105], and manifold learning [106]. To demonstrate this capability, we apply our registration approach in conjunction with the tissue density based analysis known as RAVENS. This voxel-wise analysis was introduced for neuroimaging in [4], and has been used to show localized brain volume changes in Alzheimer's disease [107]. It uses a tissue

segmentation with the deformation learned from each registration to the normalized space to estimate the relative local volume changes between each subject and the atlas.

The relative local volume change is calculated by first taking each voxel in a segmentation and projecting it into the target space using the registration deformation fields. This process keeps track of how each voxel is distributed by the projection and allows the method to record the degree of compression and expansion at each voxel that the segmentations had to undergo in order to be registered into the normalized space. As a result, we obtain localized measures of volume changes for each subject relative to the average atlas. This provides the ability to locate differences in relative volume changes between control and disease populations. We use this RAVENS method in Section 5.5.3 to explore the volume differences in the macula between a healthy control cohort and a patient cohort diagnosed with MS.

## 5.3 Materials

### 5.3.1 Data

We use two pools of data for the various experiments and comparisons in the remainder of this chapter. For clarity, we will state in each section which cohort was used. All of the data was acquired using a Spectralis OCT system (Heidelberg Engineering, Heidelberg, Germany). The automatic real-time function was enabled and set to 12 averages, with all scans having SNR of at least 20 dB. Macular raster scans ( $20^\circ \times 20^\circ$ ) were acquired with 49 B-scans, each B-scan having 1024 A-scans with 496 pixels per A-scan. The B-scan resolution varied slightly between subjects and averaged  $5.8 \mu\text{m}$  laterally and  $3.9 \mu\text{m}$  axially. The through plane distance (slice separation) averaged  $123.6 \mu\text{m}$  between images, resulting in an imaging area of approximately  $6 \times 6 \text{ mm}$ . The entry position of the OCT scan was aimed towards the center of the pupil to reduce the rotation of the macula in the image. The research protocol was approved by the local Institutional Review Board, and written informed consent was obtained from all participants.

**Validation cohort** We use a *validation cohort* consisting of OCT images of the right eyes from 45 subjects. The 45 subjects consisted of 26 patients diagnosed with MS while the remaining 19 subjects were healthy controls. The 26 MS patients were screened and found to be free of microcystic macular edema [108], which our registration algorithm does not account for. An internally developed protocol was used to manually label nine layer boundaries on all B-scans for all subjects. These nine boundaries partition an OCT data set into eight regions of interest: 1) retinal nerve fiber layer (RNFL), 2) ganglion cell layer and inner plexiform layer (GCIP), 3) inner nuclear layer (INL), 4) outer plexiform layer (OPL), 5) outer nuclear layer (ONL), 6) inner segment (IS), 7) outer segment (OS), and 8) retinal pigment epithelium (RPE) complex. These retina layers are used to demonstrate the accuracy of our registration method, by comparing the algorithm's ability to use the learned deformation to transfer known labels in the source image to an unlabeled target image [109] (see Section 5.4 for details).

**General cohort** Our *general cohort* consists of retinal images from 83 subjects, which consisted entirely of right eyes with 40 scans from healthy controls and 43 scans from MS patients. Layer segmentations for this cohort was generated automatically using a boundary classification and graph based method [85], which has been shown to be highly reliable when compared to manual segmentations. This data collection is used to demonstrate several applications of our deformable registration and normalized space (see Section 5.5.1 for details). Our use of automated segmentations was motivated by the desire to demonstrate a fully automated processing pipeline. Manual segmentations, while more accurate, tend to present a bottleneck in large studies with hundreds of data sets.

## 5.4 Registration Validation

The 45 OCT images and their associated boundary labels in the validation cohort (Section 5.3.1) were used to evaluate the accuracy of our registration. This involved performing 200 registrations with each algorithm by choosing five random source images and registering each of them with the remaining 40 images as the target. The source labels were then transformed onto the target domain using the learned deformation field, and compared against the manual segmentations for each target image. This gives an evaluation of each algorithm’s ability to correctly align the retinal layers using registration.

We compared the performance of our A-OCT and D-OCT registration algorithms against SyN which was highly ranked [19] for brain MR image registration. The Dice coefficient [62] was used to evaluate the accuracy of the results relative to the manual segmentations. This was calculated for each layer  $k$  using  $d_k = \frac{2|\mathcal{T}_k \cap \mathcal{S}_k|}{|\mathcal{T}_k| + |\mathcal{S}_k|}$ , where  $\mathcal{T}_k$  and  $\mathcal{S}_k$  are the set of voxels labeled as layer  $k$  in the manual segmentation and the transferred labels, respectively. This metric is a measure of segmentation agreement and has a range of  $[0, 1]$ . A Dice coefficient of 1.0 corresponds to complete overlap between  $\mathcal{T}_k$  and  $\mathcal{S}_k$ , while a score of 0.0 represents no overlap between the two. Table 5.1 shows the average Dice results over 200 registrations, for each layer, using each of the three algorithms. We also computed the average surface error for each layer boundary for the three algorithms, shown in Table 5.2. This measured the average absolute A-scan distance between each boundary surface in the transferred segmentation and the surface in the manual segmentation for the target image.

Standard two-tailed Student’s t-tests (assuming unequal variances) at an  $\alpha$  level of 0.01 were performed to check for significant improvements in the Dice and boundary error results between the algorithms. Significant improvements in both measures were found for all eight layers (and nine boundaries) and their mean when comparing SyN against either A-OCT or D-OCT. When comparing A-OCT against D-OCT, significant improvements in Dice were found for 5 of the 8 layers and decrease in boundary error for 7 of the 9 boundaries (see Table 5.1 and 5.2 for specifics). Overall trends showed that on average D-OCT performed better than or equivalent to A-OCT for all 8 layers.

## 5.5 Applications

In this section we present three applications of our deformable registration algorithm for the purpose of studying population differences between patients with MS and healthy controls.

### 5.5.1 Average Atlas and Normalized Space

One main application of deformable registration is the ability to create a normalized space that individual subjects can be moved into for comparison. A common approach to achieve this is to construct an average atlas that defines the normalized space. This atlas can then be used as the target image for registering images from future subjects into the normalized space.

The 40 healthy control images in the general cohort were used to construct an average atlas following the approach referenced in Section 5.2.3. Two iterations of the average atlas adjustment was applied in the atlas construction. Figure 5.5 shows two views of this average atlas. In the following sections, this atlas is used as the target image for moving each subject into the normalized space.

Table 5.1 Dice overlap between segmentations transferred using a registration algorithm and the manual segmentation for eight retinal layers, averaged over 200 registrations (40 target and 5 source images) using SyN [6], A-OCT, and D-OCT. Asterisk (\*) values on the D-OCT row indicate the layers that gained significant improvements (at an  $\alpha$  level of 0.01) in Dice when comparing A-OCT against D-OCT.

	Layers								Mean
	RNFL	GCIP	INL	OPL	ONL	IS	OS	RPE	
<b>SyN</b>	0.51	0.56	0.35	0.37	0.49	0.25	0.27	0.42	0.40
<b>A-OCT</b>	0.83	0.80	0.55	0.63	0.83	0.63	0.71	0.85	0.73
<b>D-OCT</b>	0.84	0.82	0.61*	0.69*	0.85*	0.72*	0.76*	0.85	0.77*

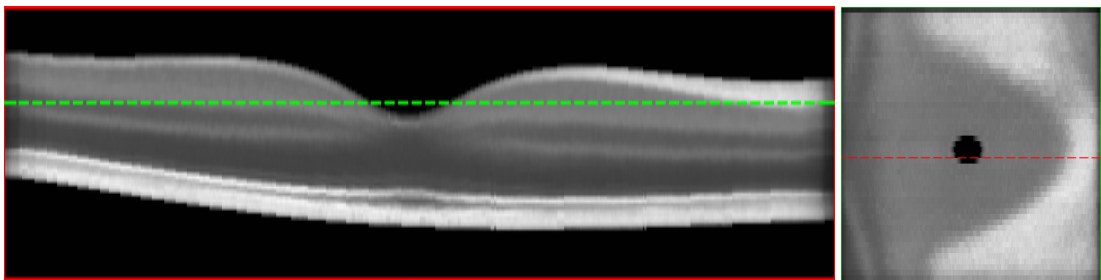


Figure 5.5 B-scan (left) and en-face (right) views of an average atlas created from macular OCT images from 40 healthy control subjects. The green and red lines show the location of each view relative to the other. The vertical scale in the B-scan view is tripled to better show the details of the atlas.



Table 5.2 Average layer boundary surface errors ( $\mu\text{m}$ ) between segmentations transferred using a registration algorithm and the manual segmentation for nine retinal layer boundaries, averaged over 200 registrations (40 target and 5 source images) using SyN [6], A-OCT, and D-OCT. Asterisk (\*) values on the D-OCT row indicate the layers that gained significant improvements (at an  $\alpha$  level of 0.01) in Dice when comparing A-OCT against D-OCT.

	Layer Boundaries				
	ILM	RNFL GCIP	GCIP INL	INL OPL	OPL ONL
<b>SyN</b>	30.3	34.4	38.9	37.9	40.5
<b>A-OCT</b>	4.3	11.6	13.5	12.4	11.3
<b>D-OCT</b>	4.1*	10.3*	11.9*	10.6*	9.79*
	ONL IS	IS OS	OS RPE	BrM	Mean
<b>SyN</b>	38.0	37.1	36.2	31.3	36.8
<b>A-OCT</b>	6.9	6.4	7.2	5.1	9.3
<b>D-OCT</b>	5.8*	4.0*	6.9	4.9	8.0*

### 5.5.2 Statistical Atlas

One useful application of a normalized macular OCT space is the ability to construct a statistical representation of spatial locations of retinal layers in the macula. By moving the retinal layer segmentations for each healthy control in the general cohort into this common space, we can empirically estimate the probability of a voxel belonging to a particular layer. Figure 5.6 shows each layer in a statistical atlas computed in this manner. Since everything is calculated in the average atlas space, the probabilities correspond spatially with the average atlas. Hence, if the average atlas is registered to a new image (or vice-verse), then the statistical atlas can be directly carried over using the same deformation. This provides a statistical estimate of the location of each layer in the new image, which can be used with other segmentation and analysis methods by providing a prior probability of each layer in the new image.

### 5.5.3 RAVENS Analysis of Multiple Sclerosis

For our final application, we evaluated RAVENS maps constructed by registering the entire general cohort (controls and MS patients) into our normalized atlas space. Figure 5.7 shows an example of a RAVENS map created between a subject's image and the average atlas, using the approach described in Section 5.2.4. For our analysis, the registration was performed using the D-OCT registration and the segmentation of the retinal layers were automatically found using a boundary classification and graph based method [85].

The goal of this experiment was to perform a pilot study looking for significant differences in layer volume changes (relative to the normalized space) between the healthy control and MS cohorts. The RAVENS map for each subject was used with SPM [110] to perform a Student's T-test at each voxel in the image. False discovery rate (FDR) was used to correct for multiple hypothesis testing. This created a

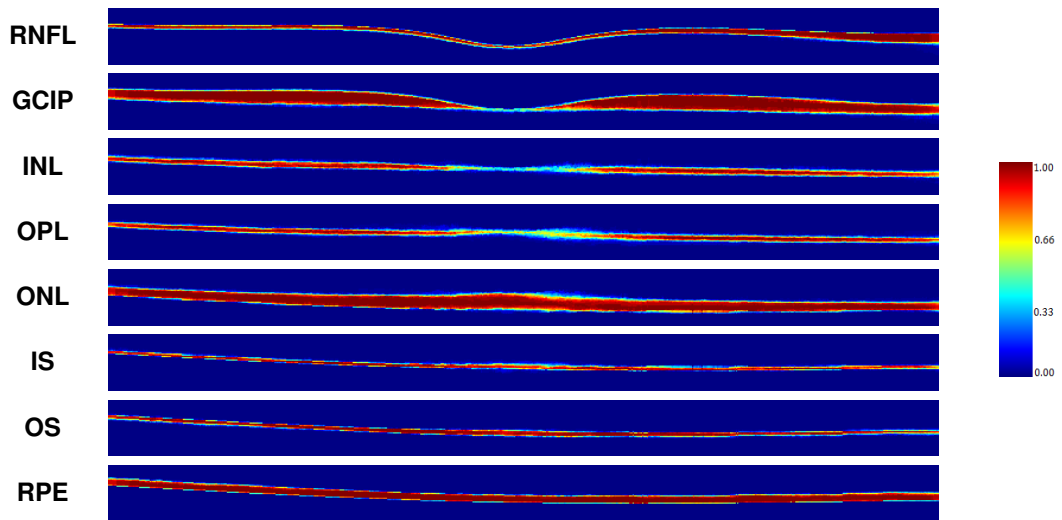


Figure 5.6 Statistical atlases of the 8 retinal layers constructed from 40 healthy control subjects registered into a normalized space.

$p$ -value map, where each voxel represents whether there is significant differences in volume changes between the control and MS cohorts at that location. Figure 5.8 shows a snapshot of this significance map (at an  $\alpha$  level of 0.05) for all 8 layers combined. We see from the figure that this type of analysis shows better localization of differences between the two cohorts, in comparison to standard thickness measurements evaluated over a segmentation.

## 5.6 Discussion

### 5.6.1 Evaluation Against Existing Methods

To our knowledge, there has been no other openly available deformable registration algorithm designed and validated on macular OCT volumes. Hence, our method could only be compared against currently available generic registration algorithms that have been used with success in various other anatomical locations. Our results in Table 5.1 and 5.2 show that on average our D-OCT algorithm produced the most accurate and robust results for aligning retinal layers when comparing segmentations transferred by the registration against manual segmentations. Relative to SyN, both A-OCT and D-OCT performed significantly better when registering retinal layers, which is expected given that SyN was not designed for macular OCT.

Independent of the comparisons to SyN, our method was able to produce high levels of layer alignment relative to manual segmentations. The Dice coefficient tends to heavily penalize small errors in the segmentation when comparing thin structures such as retinal layers, because small shifts between thin objects can dramatically reduce their overlap. Hence, an overall mean Dice overlap of 0.77 for the layers is considered fairly high, given that each of the retinal layers is only around 10-20 voxels thick. The

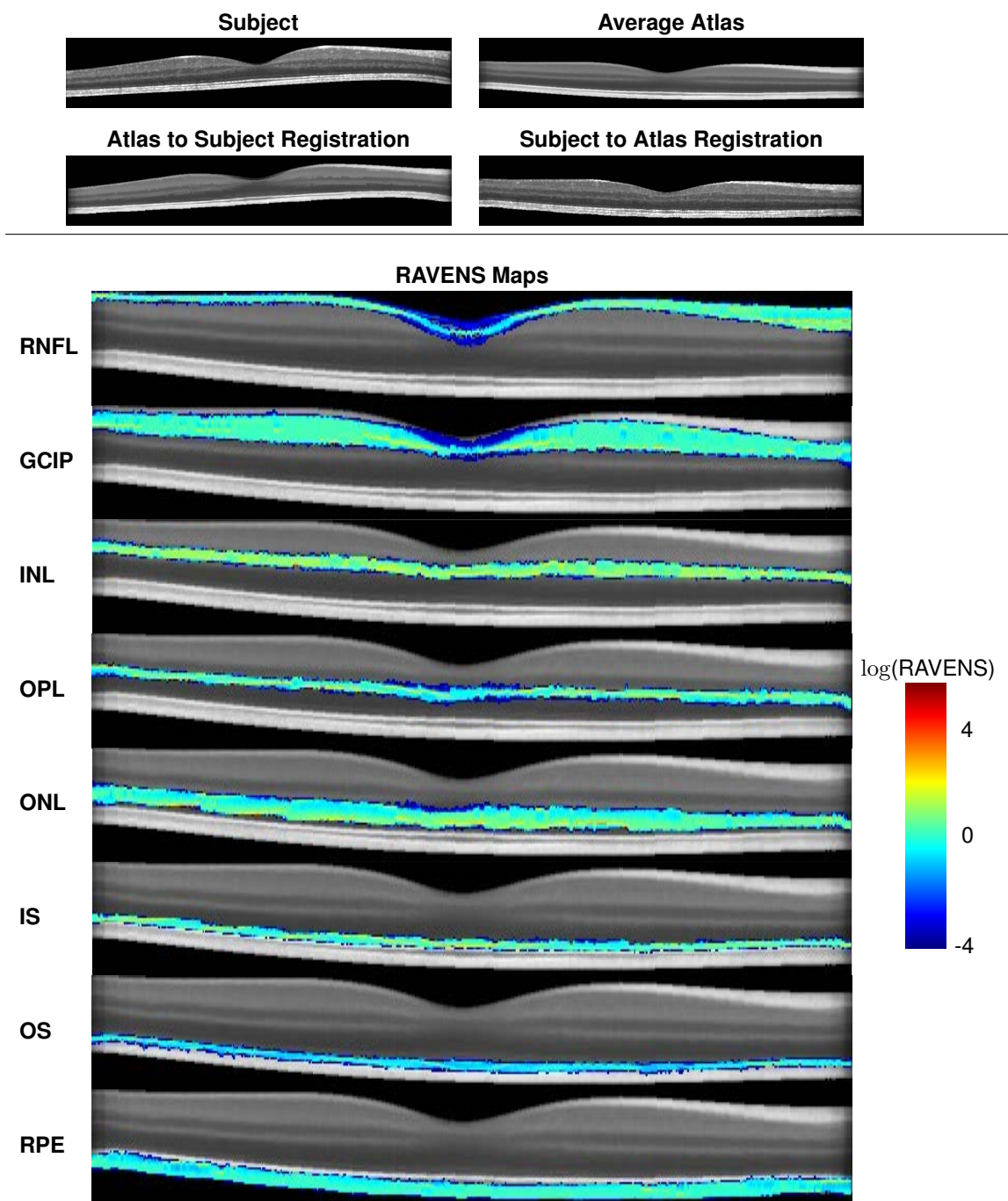


Figure 5.7 Shown are an image from a healthy control subject and an average atlas, their registrations to each other, and the subject's RAVENS maps for each layer, overlaid on the average atlas. Each RAVENS map is shown in log scale to better illustrate where the tissue is expanding (blue) or compressing (red) relative to the average atlas. The vertical scale of the B-scan is doubled to better show the details of the maps.

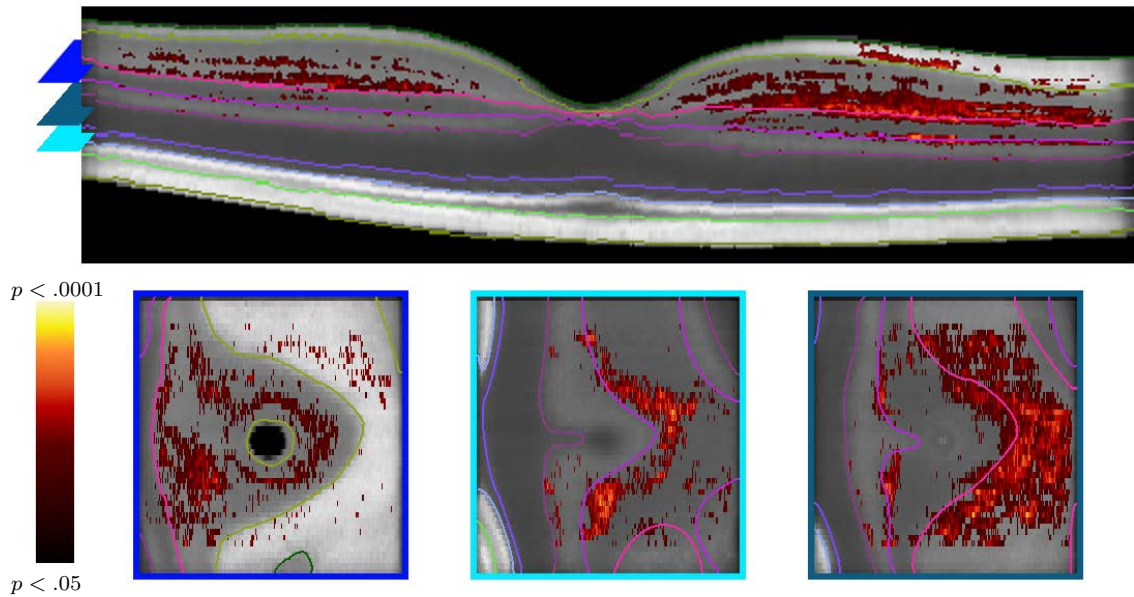


Figure 5.8 SPM significance map (at an  $\alpha$  level of 0.05) of RAVENS differences between the control and MS cohorts overlaid on the average atlas. Shown are a B-scan view (top) and three en-face views at different depths (bottom). The colored markers on the left side of the B-scan show the depth location of each en-face view. Colored lines indicate the boundaries between each layer. The vertical scale of the B-scan view is tripled to better show the significant areas respective to the average atlas.

average surface errors for the layer boundaries were also fairly low for our algorithm, with an average of  $8\mu\text{m}$  across all nine boundaries. We do note that this error is higher than state of the art segmentation algorithms [85], which is expected since the registration algorithm must learn a deformation between the images and is restricted by the regularization necessary to keep the deformation sensible.

Lastly, since A-OCT is solved directly and D-OCT is only optimized in a single direction at each A-scan, our registration approach is computationally very efficient. On a single 2.73 GHz processor with 8 GB of RAM, running the A-OCT registration on  $1024 \times 496 \times 49$  images took on average 3 minutes per registration (including pre-processing time). The D-OCT registration, which includes both pre-processing and A-OCT, had an average runtime of 106 minutes. This is a considerable improvement over SyN which had an average runtime of 9 hours on the same images using the same machine.

## 5.6.2 Clinical Relevance

Using our registration approach, we have constructed a normalized space and average atlas for macular OCT, which enables a number of population based analyses. In this work, we have shown two such applications. First, we have created a set of statistical atlases, which can be used as prior information for future segmentation and registration approaches. This allows such algorithms to improve its accuracy by comparing unknown images to these atlases in order to create robust initializations for the solution. These atlases can also potentially be used to develop more advanced atlases for comparison

against normal anatomy, similar to standard growth charts. Second, we used the normalized space to perform population analysis by constructing RAVENS maps to analyze local volume differences between controls and patients with MS. Our results found significant clusters of volume change difference between healthy and MS patients in the RNFL and GCIP layer. This result corresponds with existing reports that suggest patients with MS undergo significant atrophy of the RNFL and GCIP [111, 112]. Our results also found much smaller clusters of differences in the INL, which is consistent with reports suggesting that INL atrophy is also present in MS, but only in about 40% of patients [108, 112]. However, one major advantage provided by our analysis is the ability to detect specifically in 3D where such changes are occurring, whereas previous methods relied on average OCT thickness analysis across 2D regions of the macula or post-mortem histological analysis. We see from Figure 5.8 that the significant voxels are strongly localized towards the medial (nasal) side of the fovea. In addition we see that the highly significant differences are concentrated in the deeper areas of the GCIP layer. This type of analysis is unavailable when using standard approaches, such as thickness measurements, for evaluating macular OCT.

### 5.6.3 Algorithm Limitations

There are several limitations to our registration algorithm. First, a common limitation of most registration algorithms is that correspondences are inconsistent between the source and target images. In retinal OCT, this can occur when particular layer structures are not visible in either the target or source image. An example of this is shown in Figure 2, where the hypo-intense region in the RPE is visible in the source image, but not in the target image. Since there is no correspondence between the images, the algorithm relies on regularization for alignment, creating errors.

These errors can potentially be avoided by using better OCT acquisitions with higher resolution or SNR such that the same structures always appear in both images. Alternatively, if the problem is isolated to a few A-scans, such as in this case, then it might be possible to address it by increasing the weight of  $E_m^{\text{Reg}}$  relative to  $E_m^{\text{SSD}}$  in the final cost function. However, this is a trade-off that can force too much regularization across A-scans and result in lower overall accuracy.

Another example of inconsistent correspondences in retinal OCT is disrupted or missing layers due to pathology (retinal detachment, edema, etc.). The locations of such pathology are often unpredictable, and may not be present in both the target and source images. As a result, the algorithm may attempt to align layers with similar intensities to these pathologies, creating errors in the registration. To address these problems, further development of the algorithm will be necessary to detect and regularize the transformations in these situations.

Second, data limitations can directly affect the performance of the algorithm. For example, due to the sparse sampling of the B-scans in our Spectralis data, we are limited by the type of regularization and interpolation allowed in the algorithm. Given data with higher resolutions and denser sampling, we can potentially improve the accuracy of the registration and provide better acuity in the types of analyses we have demonstrated.

Third, errors during the data acquisition can affect the accuracy of the registration. One example of this is the appearance of a rotation of the retina, often caused by the OCT scan not being centered on the pupil during the acquisition [113]. When the retina is tilted in the OCT, our discrete translation of the A-scans becomes a less valid model for rigidly aligning the macula, which lowers our registration accuracy. In general, our algorithm cannot correct for this rotation, because rotating the OCT would cause the  $z$ -axis in the OCT to no longer represent the A-scans. This would make it difficult to justify any transformations along this axis, since the size of each voxel along the axis would now depend on the fan-beam separation, which depends on the cornea of the subject being imaged. Care must be taken to use data that is properly centered to minimize these errors.

Fourth, intensity inhomogeneity can still be a problem for the algorithm after intensity normalization, where shifts in intensity can be seen in the OCT even after preprocessing. One potential improvement to address this is to use a similarity metric that is more robust to intensity variabilities. Our preliminary results suggest that the cross-correlation measure may be a good replacement for SSD in future versions of the algorithm.

Lastly, since the detected ILM and BrM locations are used in the affine registration step, errors in their detection can cause poor initialization for the deformable registration step. This might cause the optimization to get caught in a local minima, resulting in errors in the final registration. Although the retinal mask is generally found very accurately and robustly in our experiments, certain pathology can make these boundaries difficult to detect. In such cases, the boundary detection algorithm may need to be modified.

## 5.7 Summary

In this chapter we have presented both an affine and deformable registration method designed specifically for OCT images of the macula, which respect the acquisition physics of the imaging modality. Our validation using manual segmentations showed that our algorithm is considerably more accurate and robust for aligning retinal layers than existing generic registration algorithms. Our method opens up a number of applications for analysis of OCT that were previously not available. We have demonstrated three such examples through the creation of an average atlas, a statistical atlas, and a pilot study of local volume differences in the macula between healthy controls and MS patients. In our RAVENS analysis we found differences that corresponded with existing literature on retinal changes in MS, and provided information regarding the 3D location of these differences which were not available in previous studies. The applications we provided in this chapter are but a small example of the existing methods and techniques that utilize deformable registration and normalized spaces to perform population based analysis of disease, many of which can potentially benefit our study and understanding of MS. The work described in this chapter has been presented in conference [92] and journal [114] form.

## Chapter 6

# Multi-channel Registration of Brain MRI

### 6.1 Introduction

The human brain is the central processing structure in the CNS. It plays a vital role in almost all functions in the body, including sensory and motor control, learning, memory, and cognition. In MS, pathology in the brain can lead to deterioration or disabilities in any of these functions, which has led to extensive studies of the structure in relation to the disease [115, 116, 117, 118]. Currently, MR imaging is the gold standard for analyzing MS in the brain. This is primarily due to its ability to provide contrast between *white matter* (heavily myelinated) and *grey matter* (lightly myelinated or unmyelinated) tissue. Since MS is characterized by inflammatory attacks that demyelinate axons, MR images can provide direct insight on MS pathology and disease processes. In addition, unlike CT, MR imaging does not use ionizing radiation; hence, it is generally considered safe and noninvasive. This allows for larger studies and more regular acquisitions.

In recent years, brain MRI acquisition and analysis has steadily moved towards multi-modal imaging, where multiple MR sequences are used to acquire different contrasts of the same subject. This provides additional information on brain structure and pathology that may not be present in any particular contrast. In this work, we refer to these different contrast images as MR *modalities*. Figure 6.1 shows an example of a pair of aligned T1-weighted (T1w) and T2-weighted (T2w) MR brain image from the same subject. We can see that the two modalities show different sets of features and contrast for the same brain. In MS, the benefits of multi-modal MRI analysis is already evident. Fluid-attenuated inversion recovery (FLAIR) [119] and susceptibility weighted [120] sequences have both been used to perform better detection and analysis of MS lesions (sites of demyelination) in the brain. Magnetization transfer images have been shown to predict the onset of MS lesions in normal appearing white matter [121].

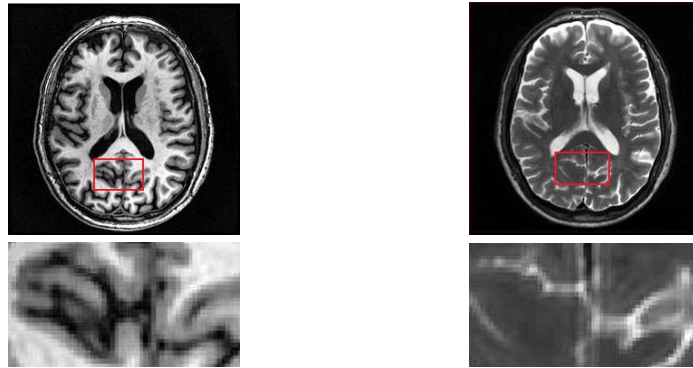


Figure 6.1 Shown in the top row are a pair of aligned T1w and T2w brain images from the same subject, demonstrating the different contrasts and features that can be seen in different MR modalities. The red boxes indicate the zoomed in regions shown in the bottom row.

For image registration, the emergence of multi-modal MR imaging has promoted the development of *multivariate* registration algorithms. Unlike traditional registration techniques which only registers a single source image to a single target image, multivariate algorithms use multiple modalities for the source and target simultaneously during the registration. In such frameworks, the extra modalities are used to evaluate a combined cost function that optimizes a transformation to best align all the image modalities. These techniques have been shown to be more accurate and robust than their univariate counterparts [122, 123, 124, 125].

In this chapter we first present a *multi-channel* enhancement to the ABA registration algorithm (Section 2.3.1). In a multi-channel framework, analogous modalities for the source and target images are matched up into multiple channels, where each channel evaluates a separate similarity function for that modality. The cost for the individual channels are then weighted and summed to create the final cost for the algorithm. This improvement allows ABA to use multiple modalities simultaneously to solve for the transformation between the source and target images.

Using this multi-channel framework, we present two methods that uses the extra channels to improve brain MR registration. In the first method, we use distance transforms of tissue segmentations to incorporate spatial information into the registration. The approach is used with mutual information to account for areas in the image where there is a lack of information, such as regions in the white matter where the intensity is homogeneous. The second method is an approach for performing multi-channel registration when modalities are not analogous between the source and target image. Our approach fills in the incomplete channels by using image synthesis to creating the missing modalities from existing ones. This allows single channel cross modality registrations to be converted into a multi-channel registration with mono-modal channels.



## 6.2 Vectorized Adaptive Bases Registration Algorithm (VABRA)

### 6.2.1 Introduction

In this section, we present our multi-channel enhancement to the ABA registration algorithm. Our improvement allows the registration algorithm to take in multiple modalities for the source and target, and solve for a more accurate transformation that best aligns all the modalities. We validate our approach by comparing between single and multi-channel ABA results from a series of deformation recovery experiment using both phantom and real data.

The primary reason that we developed ABA into a multi-channel framework is that the algorithm was originally designed for modal-modal image registration. It was one of the first deformable registration algorithms designed specifically to use the mutual information cost function. Hence, it has been used successfully for addressing many multi-modal problems [126, 127, 128]. However, while mutual information has proven to be a robust metric for such applications, under certain conditions its probabilistic nature can be a drawback that greatly reduces its effectiveness as a cost function [17].

By extending ABA into a multi-channel registration, not only are we able to build upon the algorithm’s success for solving multi-modal registration problems, but also address the inherent limitations to the mutual information cost function used in the algorithm (Sections 6.3 and 6.4).

### 6.2.2 Methods

#### 6.2.2.1 Multi-Channel Cost Function

We begin with the general single-channel registration framework presented in Section 2.2.1, where we register a source image  $\mathcal{S}(\mathbf{x})$  to a target image  $\mathcal{T}(\mathbf{x})$  by solving for a transformation  $v$ , such that the transformed source image  $\mathcal{S}(v(\mathbf{x}))$  is in the same space as  $\mathcal{T}(\mathbf{x})$ . In ABA this transformation is modeled as a summation of RBFs, which is optimized using an energy cost function,

$$E_{\text{Single Channel}} = \mathcal{C}(\mathcal{S} \circ v, \mathcal{T}), \quad (6.1)$$

where  $\mathcal{C}$  is the similarity metric that describe how alike the two images are. This cost function was originally restricted to mutual information, however our implementation also includes the option to use SSD.

Our multi-channel enhancement for the algorithm allows additional modalities of the source and target images to be included in the registration. The algorithm first takes each modality and separates them into channels with its own cost function. These individual costs are then weighted and summed to create the total multi-channel cost function. Suppose we have a source image set with  $N$  modalities of the same subject,  $\{\mathcal{S}_1, \mathcal{S}_2, \dots, \mathcal{S}_N\}$ , and a target image set with analogous modalities,  $\{\mathcal{T}_1, \mathcal{T}_2, \dots, \mathcal{T}_N\}$ ,

then this multi-channel energy cost function can be described by,

$$E_{\text{Multi-Channel}} = w_1 \mathcal{C}(\mathcal{S}_1 \circ v, \mathcal{T}_1) + w_2 \mathcal{C}(\mathcal{S}_2 \circ v, \mathcal{T}_2) + \dots + w_N \mathcal{C}(\mathcal{S}_N \circ v, \mathcal{T}_N), \quad (6.2)$$

where  $w_1, w_2, \dots, w_N$  are weights that determine the contribution of each modality to the final energy function. Likewise, this modifies the local gradient computation for the cost function (Eq. 2.19) into

$$G(\boldsymbol{\alpha}) = \sum_n w_n \nabla_{\boldsymbol{\alpha}} \mathcal{C}(\mathcal{S}_n \circ v, \mathcal{T}_n). \quad (6.3)$$

These modifications improve the registration algorithm in two ways. The first improvement is at the misregistered regions identification stage of the algorithm. Since the final gradient is now a weighted sum of the gradients from each channel, we see that if the gradient for all the channels have a local maximum at a specific region, then the final gradient at that region will also be a local maximum. Likewise, if the gradient at that region is at a minimum for all the channels, then the final gradient there will also be at a minimum. Since ABA identifies the misregistered regions by order of gradient magnitude, this modification allows it to first identify the regions where there is misregistration in all the channels. Then it will address regions where only particular channels indicate misregistration, for example regions where some channels have strong contrast while the others do not. Lastly, the areas where none of the channels exhibit a strong gradient will be ignored.

The second improvement occurs at the local optimization stage of the algorithm. As described in Sec 2.3.1, after identifying the misregistered regions the local optimization is performed via a standard line search algorithm. By incorporating the information from multiple channels, the final coefficients for the RBFs placed at those locations will be optimized using all the image channels rather than a single channel. This allows the final deformation to be optimized using the information from every image modality, thus combining and detecting features with different contrast that may not have been present in any given single channel.

## 6.2.3 Experiments and Results

### 6.2.3.1 Toy Image Simulation

In our first experiment we ran the single channel and multi-channel algorithm on a toy image created by taking the distance transform of a cube, shown in Figure 6.2. For the source image we deformed the distance transform with a 3x3x3 magnitude sinusoid, and for the target images we separated the original image into two halves, and replaced the missing half of each image with a constant value. The goal of the experiment was to show that the multi-channel algorithm is capable of using asymmetric information from both channels to recover the original image.

From the single channel result in Figure 6.2 we see that the registration was unable to correctly recover the original image. This was expected since information for half of the original image was missing.

From the multi-channel result we see that the original image could be recovered if each channel used a different half of the original image as the target. Information from both channels were used together to successfully perform the registration. In addition, we see that the multi-channel registration also performed better in the half of the image that was available to the single channel experiment. The intensity ramp in the multi-channel result was better aligned with the original image, and the intensity did not expand outwards as seen in the single channel result. However, one error we do observe in the multi-channel result is at the mid-line where there is a noticeable divide between the two halves. This was likely caused by the boundary effects introduced by replacing half of the target image with a block of constant intensity.

This experiment demonstrated the utility of the multi-channel registration and its ability to use different information in each channel together in the registration. In real MR images, we expect the different modalities to contain these different information. Hence, by using the modalities together in a multi-channel framework we can produce a more accurate registration.

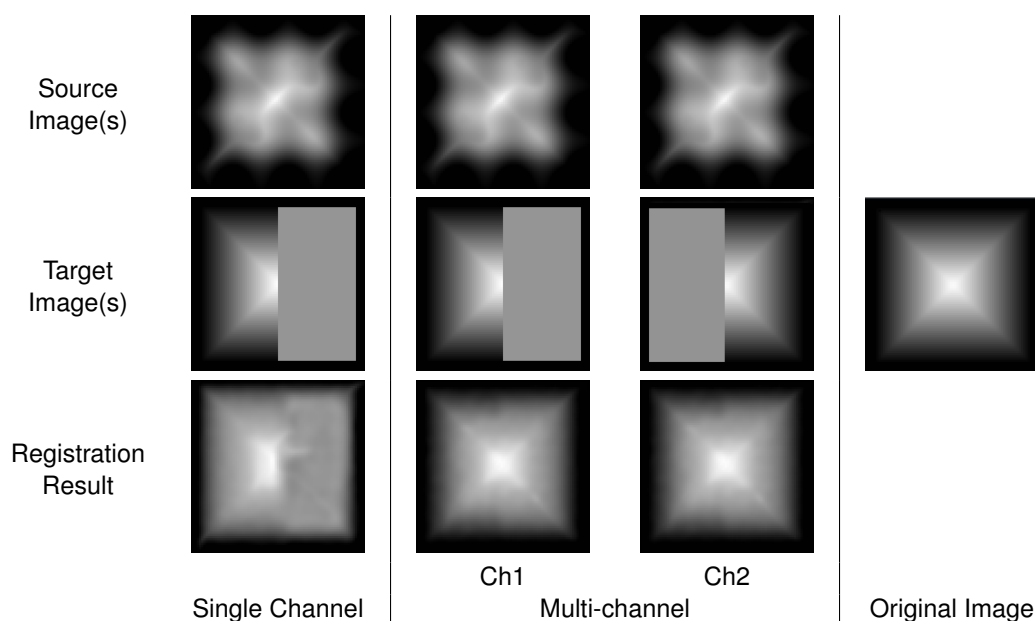


Figure 6.2 Toy example of single channel and multi-channel ABA registration results using a distance transform of a cube (rightmost column). The source images were constructed by deforming the distance transform with a  $3 \times 3 \times 3$  magnitude sinusoid. The target images were constructed by taking the distance transform and replacing half of it with a constant value.

### 6.2.3.2 Deformation Recovery Using Phantom and Real MR Data

To evaluate the accuracy of our multi-channel improvement to ABA, we performed a number of deformation recovery experiments where a known deformation was applied to an image and the deformed image was registered to the original image in order to recover the deformation. In each experiment we calculated the average error (in voxels) between the recovered deformation and the known deformation over the union of the non-background regions of the subject, target, and the registration result. These

experiments were ran on phantom and real data using both single and multi-channel ABA, and with two different simulated deformations. The first deformation was a low magnitude, two-dimensional sinusoid ranging from  $-2$  to  $2$  voxels, while the second was a high magnitude, three-dimensional sinusoid ranging from  $-9$  to  $9$  voxels displacement.

**Phantom MR Data** Our phantom data experiment used the T1-weighted (T1w) and T2-weighted (T2w) phantom brain images from the Brainweb Simulated Brain Database [129]. The experiment was performed on 15 available variations of the phantom brain image, containing five different levels of noise (0%, 3%, 5%, 7%, 9%) and three different levels of field inhomogeneity (0%, 20%, 40%). Table 6.1 shows the average deformation recovery error over the 15 datasets when using the two modalities separately in single channel registrations, and together in a multi-channel registration.

We see from the single channel results that the T1w and T2w images produced different levels of performance depending on the magnitude of the deformation applied to the image. The T1w images allowed for better deformation recovery when the applied deformation was low magnitude, while the T2w images performed better when the deformation was high magnitude. This suggests that the two modalities had different features that was beneficial for recovering different sizes of deformations.

From the multi-channel result, we see that using the two modalities together helped produced consistently low recovery errors, regardless of the deformation magnitude. In both the high and low magnitude case, the multi-channel error was in the same range as the best modality for that magnitude (T1w for low, and T2w for high). This indicates that the multi-channel registration was able to take the best features from each modality to perform the best registration given the size of the deformation being recovered. This represents a considerable improvement in registration robustness, since in real world applications we do not always know the size of the deformation that need to be recovered.

Table 6.1 Shown are the average absolute errors (in voxels) between a known deformation applied to the Brainweb phantom and the deformation recovered using single channel (“T1w” and “T2w”) and multi-channel (“T1w+T2w”) registration, for low and high deformation magnitudes.

Phantom Data	T1w	T2w	T1w + T2w
Low Magnitude	0.0914	0.1075	0.0895
High Magnitude	0.4560	0.4322	0.4361

**Real MR Data** We repeated the phantom data experiments described above using real brain MR datasets from 11 subjects. For each subject we used a T1w, magnetization-prepared, rapid gradient echo (MPRAGE) sequence and a T2w spin echo sequence as the two different modalities. The experiments were ran on both the original full head scans and on a skull stripped [130] version of the data where non-brain tissues were removed from the image. Table 6.2 shows the results of these experiments averaged over all 11 subjects.

We see from the low deformation magnitude results that using the T1w images by themselves produced the best results, while using the T2w images by themselves produced the worst results. Using both modalities together with multi-channel generally produced results in between the single channel experiments. However, the average difference in performance between the T1w single channel case and the multi-channel case was only one to three thousandth of a voxel. Overall, using the T2w image together with the T1w image had very little effect on registration accuracy when the deformation was small.

The more interesting result was when a high magnitude deformation needed to be recovered. We see from the table that using T1w images by themselves was again better than using T2w image by themselves. However, the multi-channel experiment results was considerably better than either single channel experiments. By adding in the T2w images as a second channel, the registration was able to dramatically improve over the T1w single channel registration. This result is consistent with the phantom data experiments, where the T2 weight image allowed for better deformation recovery when the deformation was large.

One important observation from these results is that the T2w images performed very poorly when used by themselves. This suggests that the T2w images contain information that is only useful for registration when used together with the information provided by the T1w image. These results support the idea that multi-channel registration can be used to combine features and information from multiple modalities to improve the overall registration.

Table 6.2 Shown are the average absolute errors (in voxels) between known deformations applied to 11 MR brain images and the deformations recovered using single channel (“T1w” and “T2w”) and multi-channel (“T1w + T2w”) registration, for low and high deformation magnitudes, and when performed on full head images or images with non-brain tissues masked out.

<b>Whole Head Data</b>	<b>T1w</b>	<b>T2w</b>	<b>T1w + T2w</b>
<b>Low Magnitude</b>	0.3846	0.3911	0.3883
<b>High Magnitude</b>	0.7462	0.9163	0.7052

<b>Brain Only Data</b>	<b>T1w</b>	<b>T2w</b>	<b>T1w + T2w</b>
<b>Low Magnitude</b>	0.0988	0.1188	0.0996
<b>High Magnitude</b>	0.1873	0.3071	0.1704

## 6.3 Distance Transforms as Second Channel

### 6.3.1 Introduction

In recent years, mutual information (Sec 2.2.2.2) has become one of the most prominent cost functions used in medical image registration, with widespread presence in both academic and clinical applications [3]. The strength of mutual information comes primarily from its lack of dependence on

explicit intensity relationships between the images. As a result it is highly robust and applicable for a large number of image modalities. However, despite its many advantages in matching mono- and multi-modal images, there are still several major drawbacks that affects its performance [3, 131, 132]. One of these drawbacks is its loss of effectiveness as a matching criterion when working within areas of an image that has poor statistical consistency and a lack of clear structure [17]. Examples of this includes cases where there is overwhelming noise or conversely, when the area has very homogeneous intensity and provide very little information.

To demonstrate this problem, take for example a patch of an image where there is only a single intensity. In this case the total entropy of that patch is zero, and the joint entropy with any other patch is equivalent to the entropy of the compared patch. Hence, in this case the mutual information is always zero regardless of what the homogeneous patch is compared to. This causes algorithms that use local optimization to maximize mutual information to have problems when directing the deformation of these areas, since they can be effectively matched with any other patch. As a result, this makes these areas less reliable in the final registration.

This problem can be best observed when using mutual information to register two binary images, as shown in Figure 6.3. The example shows the registration between two white matter masks, which, due to the lack of intensity information present, produced poor alignment and overall noisy boundaries in the registration result. However, when the same registration was performed on the the distance transform of the segmentation, the alignment was significantly sharper and incorporated finer details. In this case, the distance transform of the segmentation populated the image with strong structural features that allowed mutual information to find a more accurate alignment.

In this section we present an approach that uses these distance transform with our multi-channel framework to provide features in areas of brain MRI that lack enough intensity information for mutual information to be effective. Our results show that by adding the distance transforms we can improve the overall accuracy of the registration in all areas of the brain.

## **6.3.2 Methods**

### **6.3.2.1 Integrating Distance Transform of Anatomical Segmentation**

In our method we use distance transforms of anatomical structures to assist the registration in areas that lack intensity information. For our experiments, we identified three areas in brain magnetic resonance (MR) images where this is true: the white matter, the gray matter, and the combination of the putamen and caudate. The segmentations for these areas were performed by using the TOpology-preserving, Anatomy-Driven Segmentation (TOADS) [57, 60] algorithm, which is capable of automatically producing topologically accurate segmentation of these structures.

TOADS was chosen for its high level of accuracy and robustness when compared to manual segmentation of cortical structures, and for its ability to automatically produce topologically correct results. The latter is particularly important when performing distance transforms, since small topology defects

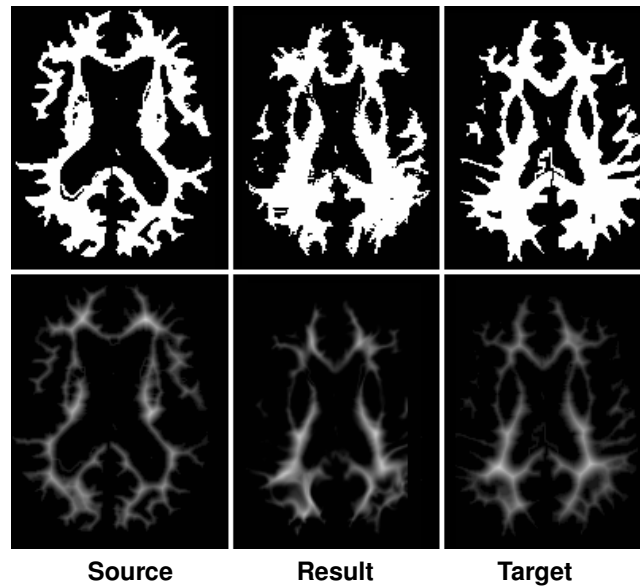


Figure 6.3 Registration results between two white matter segmentation masks (top row) and the same registration between their distance transforms (bottom row).

within the segmentation, such as a hole or handle, can produce relatively large artifacts in its distance transform. Once the segmentation was produced, its distance transform was calculated, where every point inside the segmentation is mapped as its minimum distance to the boundary of the segmentation.

The additional information provided by the distance transform was integrated into the mutual information framework using our multi-channel adaptation of ABA. In our approach, the original source and target images are treated as one channel, and their distance transforms are treated as a second channel. Since the distance transform overlaps the white matter directly, this setup allowed it to drive the registration in areas where the image is too homogeneous for mutual information to be effective. For the purpose of this study, the weights were treated as equal for both channels.

### 6.3.2.2 Data

The data used to evaluate our method consisted of 20 MPRAGE MR images of the brain from the OASIS data set (<http://www.oasis-brains.org/>). The images were skull stripped using the SPECTRE algorithm.

## 6.3.3 Experiments and Results

### 6.3.3.1 Mutual Information With Regard to Rotation

To evaluate the value of using distance transforms in the registration we performed an experiment to observe the behavior of mutual information when using an intensity, mask or distance transform image. We plotted the change in mutual information between each image and itself rotated in 5 degree

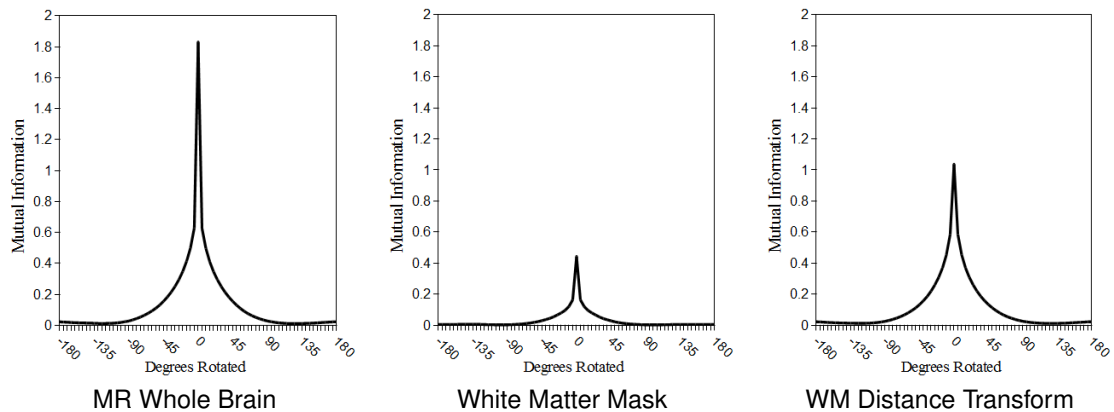


Figure 6.4 Plots of mutual information as a function of rotation for an MR brain image, its white matter mask and distance transform.

increments. Figure 6.4 shows these plots when using a MR brain image, and its white matter mask and distance transform. From the plots we can see that while all three images maintained the same overall trend, the range and rate of change differed significantly. In particular, the distance transform produced a much higher maximum and a smoother drop off when compared to the WM mask. These two qualities play an important role in optimization, since a larger maximum makes it easier to avoid local extremas, and smooth transitions into the maximum provides an easier search space. This is particularly true for algorithms that use gradient descent type methods for optimization. The MR image of the whole brain provided the best characteristics for optimization, since it contained the strongest features and the most information.

### 6.3.3.2 Single-Channel Known Deformation Recovery

Table 6.3 shows the average absolute error from a known deformation recovery experiment using brain MR images and their respective white matter masks and distance transforms in single channel registrations. The applied known deformation was a three-dimensional sinusoid ranging from -9 to 9 voxels displacement.

The result show that the white matter mask performed significantly worse for recovering the known deformation when compared to the distance transform or MR image. The primary reason for this is due to a lack of features in the white matter mask that would allow various parts of the image to be differentiated. Since the entire mask is one intensity, a voxel can be deformed from almost any direction

Table 6.3 Average error of the recovered deformation field, when using the whole MR image, the white matter mask, and the distance transform of the white matter mask.

	MR Whole Brain	White Matter Mask	WM Distance Transform
Average Error (Voxels)	1.07	2.94	1.09



in order to match with the target. This result demonstrates why distance transforms should be used as the second channel in our multi-channel framework, instead of the binary mask.

### 6.3.3.3 Segmentation Comparison of Multi-Channel Results

To evaluate the performance of our multi-channel approach using the distance transforms, 10 separate registrations were performed using different pairs of source and target brain MR images. Each registration result was then segmented by TOADS, and the overlap between the result segmentation and the target image segmentation was considered using Dice's coefficient,  $\text{Dice}(A, B) = \frac{2|A \cap B|}{|A| + |B|}$ . This value ranges from zero to one, with one indicating a perfect overlap. Table 6.4 shows the Dice's coefficient between various structures from the segmentations. This experiment was repeated using just the MR images, the white matter mask as a second channel, and the white matter mask distance transform as a second channel.

From the results, we see that using the distance transform as a second channel improved the overall overlap for the resulting anatomical segmentations. Figure 6.5 shows an example of the registration results, where we can see that using the distance transform allowed the white matter boundary to be much more sharply aligned. However, from the table we also see that using the white matter mask as the second channel significantly decreased the performance of the algorithm. This result was as expected, since the lack of intensity information in the white matter is the problem being addressed by our method. Adding the white matter mask as a second channel elevated this problem by effectively weighting the influence of these areas even more.

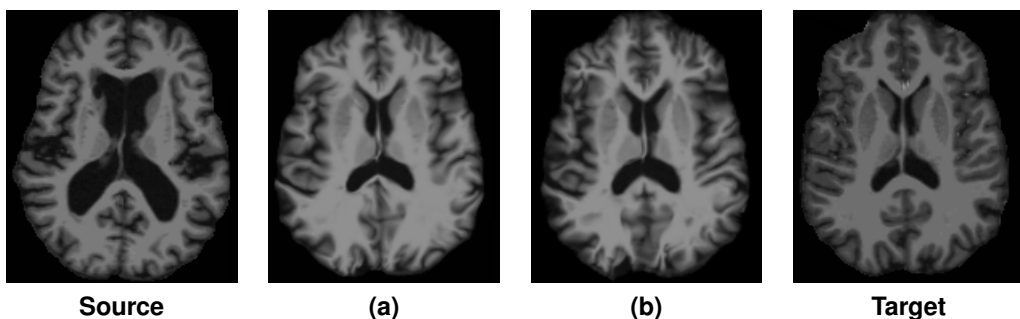


Figure 6.5 Single and multi-channel registration results between a source and target image. Shown are **(a)** the result when only using the MR images and **(b)** the result when using the distance transform of the white matter segmentation as a second channel.

## 6.4 Using Image Synthesis for Multi-modal Registration

### 6.4.1 Introduction

One primary restriction of multi-channel registration is that analogous modalities must be available for both the source and target image. This prevents such algorithms from being used in cases

Table 6.4 Average Dice’s coefficient between brain structure segmentations for the registration results and for the target images. The columns indicate when the registration was performed with just a the MR image, and when the white matter mask or its distance transform were used as second channels. Shown in parentheses are the percentage increase or decrease from adding the second channel.

Region	MR Image Only	MR Image + WM Mask	MR Image + WM Distance Transform
Grey Matter	0.759	0.603 (-20.6%)	0.770 (+1.45%)
White Matter	0.830	0.640 (-22.9%)	0.841 (+1.33%)
Putamen and Caudate	0.804	0.671 (-16.5%)	0.830 (+3.23%)

where the data is missing modalities for specific subjects, or the modalities do not match between the source and target images (i.e., in the case of cross modality registration). In this section, we address this limitation by applying an image synthesis technique [133] to provide the missing modalities for the multi-channel registration. The synthesis technique is able to create an image of one modality from another by using aligned atlases of both modalities to learn the intensity and structural transform between the modalities.

Our proposed method is related to existing registration approaches that rely on modality reduction [134, 135], where both the source and target images are converted into a single modality before registration. However, our approach has an advantage over these methods in that information is not lost during the conversion. By using a multi-channel registration, the algorithm can take advantage of the features and properties of both modalities to improve its performance.

The image synthesis allows the single channel cross modality registration problem to be converted into a multi-channel registration with mono-modal channels. This provides two main advantages: first, it removes the necessity of using a multi-modal similarity metric, such as mutual information, which is non-local and often less accurate than their mono-modal alternatives [17]. Second, it gains the benefits of using the multi-modal information in the registration, which has been showing to provide more accurate and robust registrations [124].

## 6.4.2 Methods and Materials

### 6.4.2.1 Data

The Multi-modal MRI Reproducibility (MMR) dataset [136] was used for the evaluation of our algorithm. The dataset consist of magnetic resonance (MR) images from 21 healthy volunteers, with 16 MR image modalities for each subject. T1-weighted MPRAGE (T1w) images from 10 randomly chosen subjects from the dataset were designated as the “Source” cohort, and T2-weighted dual echoes (T2w) images from 10 of the remaining subjects were designated as the “Target” cohort. The T1w and T2w image from the remaining unassigned subject was used as the training atlas for the image synthesis method. Cross-validation registrations were performed between each Source subject and each Target subject, resulting in a total of 100 registrations for each experiment.

### 6.4.2.2 MRI Contrast Synthesis and Normalization

For each Source subject, the T1w image is used to create a synthetic T2w (sT2w) image using a patch-based random forest regression method [133]. The training atlas for the algorithm is constructed from the T1w and T2w images from the single unassigned subject in the MMR dataset. To generate the sT2w image from the T1w image, the method extracts 3D patches from the T1w image as features which are used to predict the corresponding T2w voxel intensity. This can be formulated as a nonlinear regression problem, where a mapping is learned from a training atlas using random forests classifiers. The mapping can then be applied to patches at each voxel in a T1w image, allowing the algorithm to predict a T2w value for each voxel, creating the sT2w image. Using the same approach, synthetic T1w (sT1w) images were created from the T2w image for each Target subject. Figure 6.6 shows a diagram illustrating this conversion from a single channel multi-channel registration between T1w and T2w, into a multi-channel registration using synthetic images, sT2w and sT1w, respectively.

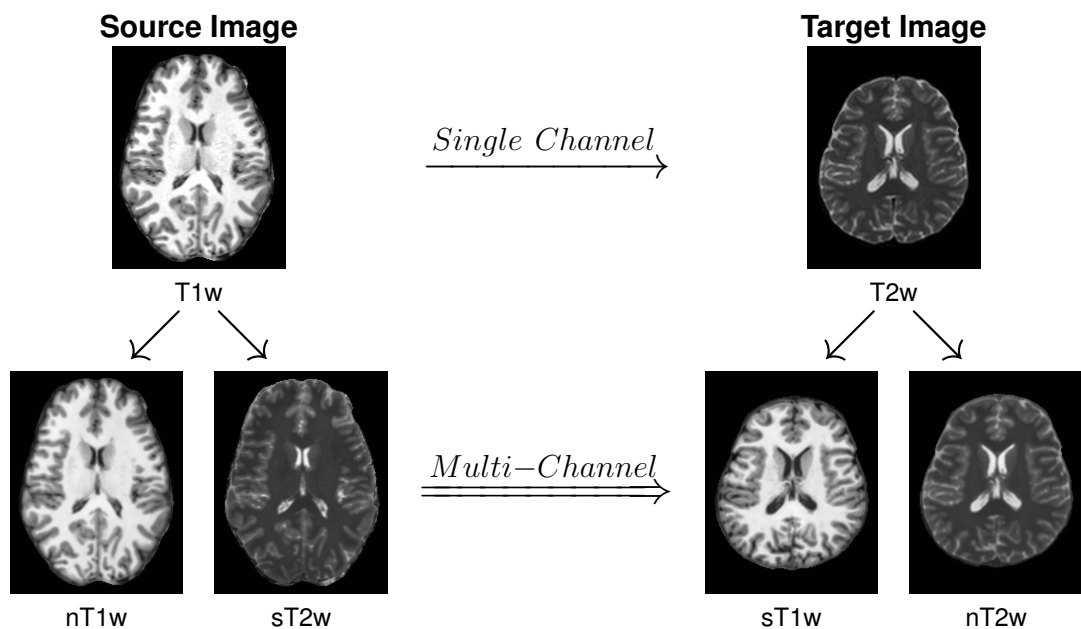


Figure 6.6 Shown is a diagram of our method for using image synthesis to convert a single channel multi-modal registration with a source T1w and a target T2w image (top row) into a multi-channel registration using normalized (nT1w, nT2w) and synthetic (sT2w, sT1w) images created from the T1w and T2w images (bottom row).

In addition to synthesizing different modalities, we also use the same algorithm to perform within-modality synthesis to create “normalized” T1w (nT1w) images by learning the mapping between T1w and sT1w images, and likewise for normalized T2w (nT2w) images. The advantage of these normalized images is that they are created from the same atlas as the synthetic images, which gives them intensities that are comparable to the synthetic images. Using these normalized images in place of the original images allows mono-modal cost functions, such as SSD, to perform better when registered with the

synthetic images. Figure 6.6 shows these normalized images next to the synthetic images as part of our multi-channel approach.

### 6.4.2.3 Using Synthesized Images in the Multi-channel Framework

Once the synthesized images are created, their use in a multi-channel framework is fairly straightforward. Using Equation 6.1, we can represent a standard MI-based multi-modal registration between a source T1w image and a target T2w image as,

$$E_{\text{Single Channel}} = \text{MI}(S_{\text{T1w}} \circ v, T_{\text{T2w}}). \quad (6.4)$$

By using image synthesis to create a sT2w from the T1w image, and a sT1w from the T2w image, we can complete the channels in Equation 6.2, which allows the energy function to be converted to,

$$E_{\text{Multi-Channel}} = w_1 \mathcal{C}(S_{\text{T1w}} \circ v, T_{\text{sT1w}}) + w_2 \mathcal{C}(S_{\text{sT2w}} \circ v, T_{\text{T2w}}). \quad (6.5)$$

Since the channels are mono-modal,  $\mathcal{C}$  is no longer restricted to MI after the conversion, and can be replaced with a mono-modal similarity metric such as SSD or CC. For our experiments, the channel weights are set to be equal.

### 6.4.2.4 Registration Algorithms

From Equation 6.5, we see that the proposed technique is independent of the registration choice. Our method operates solely on the images entering the registration algorithm, and therefore, it functions as a pre-processing step that fills all the incomplete channels in the multi-channel algorithm. To demonstrate this, we validated our method using both our multi-channel ABA approach and also a multi-channel implementation of the SyN [124] algorithm.

## 6.4.3 Experiments

### 6.4.3.1 Intra-subject Deformation Recovery

In our first experiment we evaluated our method's ability to help recover intra-subject cross modality distortion. We used the Brainweb dataset, and set the T1w image as the source and the T2w image as the target. Eight 2x2x2 three-dimensional sinusoidal deformations (each shifted by permutations of  $\pi/2$  in the x, y, and z directions) were applied to the T1w data, and the distorted images were registered to the T2w image so that the recovered deformations could be compared to the known deformations. The goal of the experiment was to evaluate if our multi-channel synthesis approach was more accurate than a standard mutual information registration between the two modalities. Table 6.5 shows the average error (in voxels) when using a single channel T1w to T2w NMI registration and our multi-channel synthesis approach, with and without the normalization for the original images. We see from the result that our

Table 6.5 Shown are the average error (in voxels) and standard deviation of known deformation recovery experiments using T1w and T2w images from the Brainweb dataset with a single channel multi-modal registration (“T1w→T2w”), and multi-channel registrations using the synthesized images with (“[nT1w, sT2w]⇒[sT1w, nT2w]”) and without (“[T1w, sT2w]⇒[sT1w, T2w]”) the normalized images.

Experiment Type	NMI	SSD
<b>T1w→T2w</b>	0.2471 (0.2130)	22.250 (0.4261)
<b>[T1w, sT2w]⇒[sT1w, T2w]</b>	0.1449 (0.0634)	0.0861 (0.0019)
<b>[nT1w, sT2w]⇒[sT1w, nT2w]</b>	0.0843 (0.0019)	0.0897 (0.0022)

multi-channel result on average performed much better than a standard NMI registration for recovering the deformation.

### 6.4.3.2 Intra-subject Qualitative Boundary Analysis

One challenge with evaluating intra-subject registrations in real data is that the ground truth is usually unknown. In general, we cannot determine if the recovered distortion is correct. Hence, often the best reference we have is the target image and the visible structures in the image. In this experiment we performed a qualitative analysis of intra-subject registration between T1w and T2w images. Using 10 subjects from the MMR dataset, we performed three intra-subject registrations between the T1w and T2w image for each subject. First we used a simple rigid registration with NMI, which is the current standard practice for intra-subject registration and serves as our baseline. We then looked at how the registration performed using a NMI with a single channel deformable registration. Lastly we looked at the result from our multi-channel synthesis approach. For each registration we performed a standard Laplacian edge detection algorithm on the registered T1w results, and evaluated how closely the these boundaries overlapped the T2w target.

Figure 6.7 shows an example of this analysis. We see from the figure that our multi-channel approach aligned the boundaries in the T1w images much closer to the T2w target than the rigid or single channel NMI result. In general, the registered boundaries fitted more tightly around the sulci and ventricles in the target brain image. This was particularly evident in the anterior of the ventricles (zoomed in the figure), where the rigid and single channel results had boundaries that clearly protruded into the white matter. The red arrows in the figure show several other regions where there are noticeable visual improvements to alignment when using our multi-channel approach.

### 6.4.3.3 Inter-subject Label Transfer Validation

To evaluate the advantages of using image synthesis to aid inter-subject cross modality registration, the Source and Target cohorts were used in label transfer experiments, which evaluates a registration algorithm’s ability to accurately transform anatomical segmentations between different subject images, using the learned deformation field from each registration. The two label sets used were the Mindboggle (<http://www.mindboggle.info/>) manual cortical labels available for each subject in the MMR

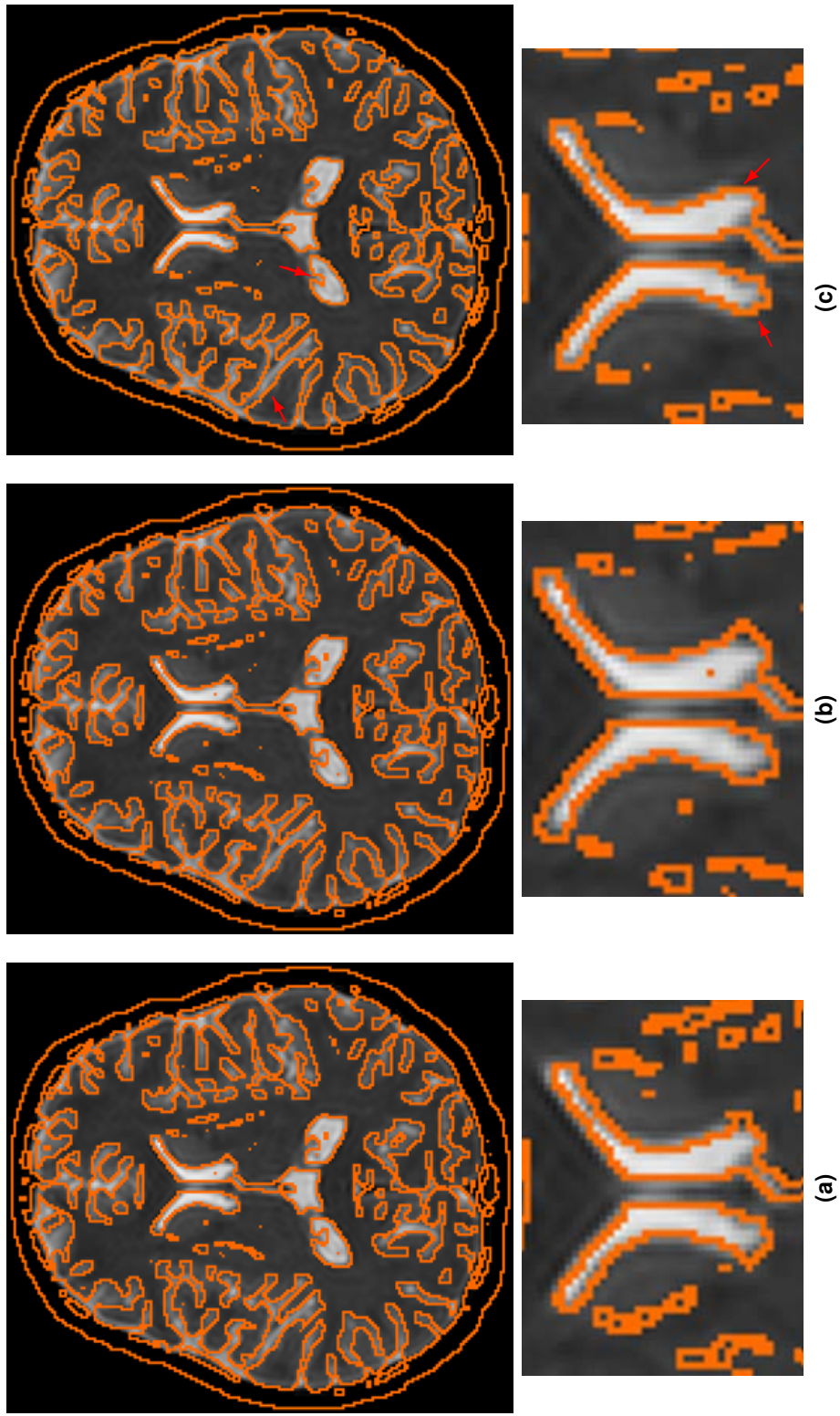


Figure 6.7 Qualitative comparison of intra-subject registrations between a T1w source image and a T2w target image. The first row shows edge maps of the T1w registered results (in orange) overlaid on the T2w target, when using (a) rigid registration with NMI, (b) single channel ABA with NMI, or (c) multi-channel ABA with synthetic and normalized images. The second row shows the ventricles zoomed in for each image to better show the alignment differences. The red arrows on (c) indicate areas where there are visual improvements to alignment when using the multi-channel approach.

dataset, and tissue classifications of cerebrum structures for each subject, generated automatically using the TOADS [60] algorithm. For each registration, and for each label set, Dice coefficients were calculated between the transformed Source image labels and the labels for the Target image, individually for each label. The Dice scores are then averaged across all labels within each label set, creating two average Dice scores for each of the 100 Source/Target registration pairs in each experiment setup.

The baseline registration setup, which we compared our method to, was a standard single-channel multi-modal registration between a Source T1w image and a Target T2w image using mutual information. We compared this against multi-channel registrations using the synthesized images with and without the normalized images. Since our approach expands the multi-modal setup into two separate mono-modal channels, we also evaluated different mono-modal similarity metrics for the multi-channel experiments. The metrics evaluated were normalized mutual information (NMI) and sum of square difference (SSD) for ABA, and mutual information (MI), cross correlation (CC), and mean square error (MSE) for SyN. Table 6.6 shows the mean and standard deviation for each setup.

We see from the results shown in Table 6.6 that regardless of the registration algorithm or cost function used, both the normalized and non-normalized synthesized multi-channel registration performed better than the single channel multi-modal registration using mutual information. This remained true for both the MindBoggle cortical labels and the cerebrum structural labels from TOADS. Standard single-tail, paired, Student's t-tests performed on these Dice results showed statistically significant improvements (at an  $\alpha$  level of 0.001) when comparing any of the multi-channel results against the single channel mutual information results. In addition, from the bold values in the table, we see that switching to a mono-modal cost function and using the normalized images for the multi-channel setup provided the best results for a given algorithm and label set. For ABA, using multi-channel with SDD produced the best result for both label sets. While for SyN, using multi-channel with CC gave the best result for the Mindboggle labels, and multi-channel with MSE gave the best result for the TOADS labels. However, the differences between the CC and MSE results were marginal relative to their improvement on using MI.

## 6.5 Summary

In this chapter we have presented a multi-channel registration algorithm that is able to simultaneously register multiple modalities for the source and target images. Our results showed that the algorithm is capable of taking information from the different modalities to improve registration accuracy and robustness, particularly when the deformation is large. In addition, we introduced two approaches that use this multi-channel framework to improve registration accuracy.

First, we presented an approach that integrates distance transforms of anatomical segmentation to assist mutual information based registrations in areas of images that lack significant intensity information. We have shown how homogeneous regions can negatively impact the effectiveness of mutual information as a similarity metric when recovering a known deformation. In addition, our results show that our

Table 6.6 Mean (and standard deviation) of Mindboggle and TOADS label transfer Dice results, when using ABA and SyN, with different similarity metrics, for the single channel multi-modal registration (“T1w→T2w”), and multi-channel registrations using the synthesized images with (“[nT1, sT2w]⇒[sT1w, nT2w]”) and without (“[T1w, sT2w]⇒[sT1w, T2w]”) the normalized images. . The bolded values show the best results for each algorithm for a given label set.

	ABA		SyN	
	NMI	SSD	MI	C
Mindboggle	T1w→T2w	–	0.266 (0.06)	0.181 (0.06)
	[T1w, sT2w]⇒[sT1w, T2w]	0.344 (0.01)	0.276 (0.07)	0.308 (0.08)
	[nT1w, sT2w]⇒[sT1w, nT2w]	0.335 (0.01)	<b>0.350 (0.01)</b>	<b>0.311 (0.07)</b>
TOADS	T1→T2	–	0.674 (0.04)	0.601 (0.07)
	[T1w, sT2w]⇒[sT1w, T2w]	0.743 (0.03)	0.705 (0.04)	0.730 (0.03)
	[nT1w, sT2w]⇒[sT1w, nT2w]	0.743 (0.03)	<b>0.752 (0.03)</b>	<b>0.734 (0.03)</b>



adaptations improved the accuracy of MR brain registrations when comparing the segmentation of the results to the segmentation of the target image. This suggests that our method is capable of improving registration in areas of the image where there is not enough information provided for mutual information to effectively align the source image to the target image.

Second, we have demonstrated an approach for multi-modal registration using image synthesis with our multi-channel framework. Our results showed that the approach can be used to improve both intra-subject and inter-subject multi-modality registrations. Our validation showed that, independent of the registration algorithm used, our approach produced more accurate registrations relative to a standard single channel cross modal registration using mutual information. This suggests that our approach is applicable beyond the multi-channel framework presented in this chapter, and can be used as a general preprocessing step for any multi-channel registration to perform cross modality registration. The methods described in this chapter have been presented in conference form [137, 138].

## Chapter 7

# Conclusion and Future Work

### 7.1 Introduction

A key challenge in the study of MS is that the disease can affect all areas of the central nervous system, and therefore requires the ability to perform analysis over multiple anatomical structures. Deformable registration is well suited for addressing this challenge because it is highly adaptable for new images and anatomical structures, and is robust when aligning structures with high variability in shape and position in the image.

In this dissertation we presented four methods that use deformable registration to improve our ability to analyze the three regions in the central nervous system that are most studied for MS—the spinal cord, the retina, and the brain. In the spinal cord we improved our ability to calculate clinically relevant imaging metrics by first developing a fully automatic segmentation approach to evaluate spinal cord volume, and then developing a pipeline for computing distortion corrected diffusion tensor metrics to analyze spinal cord microstructure through diffusion. In the retina we developed a deformable registration algorithm designed specifically for aligning macular OCT. This algorithm opened up a number of deformation and atlas based analysis techniques for studying the retina in MS. One such example is RAVENS [4] analysis which we demonstrated with a pilot study using macular OCT from healthy volunteers and MS patients. Lastly, for brain MRI, we presented a multi-channel registration framework that can use multiple MR modalities, distance transforms, or synthesized modalities to inform the registration to make more accurate alignments, and account for deficiencies in the mutual information similarity cost function.

In this chapter we summarize the main results from each of the previous chapters, we discuss their relevance to the study of MS, and we suggest potential future directions that can further improve the state of the art.

## 7.2 Segmentation of Spinal Cord MRI Using Deformable Initializations

### 7.2.1 Main Results

1. We developed a fully automatic segmentation algorithm for spinal cord MRI. Our algorithm uses deformable image registration to account for the variability of the curvature and position of the spinal cord in the MR image, and a topology preserving segmentation model to address intensity inhomogeneities in the images.
2. The accuracy of our segmentation algorithm was evaluated by comparing against two manual raters using a MT-weighted and a T1-weighted dataset each with different fields of view. For the MT-weighted dataset our result showed an average Dice overlap of 0.63 for the CSF and 0.79 for the spinal cord. For the T1-weighted dataset our algorithm showed an average Dice of 0.85 for the CSF and 0.91 for the spinal cord. These values indicate high levels of segmentation accuracy compared to the manual segmentations.
3. The robustness of our algorithm was evaluated by using the algorithm to segment a large MT-weighted dataset consisting of 238 images. The results were manually inspected for failures produced by our algorithm. Only 8 significant failures were found in the results—7 due to motion artifacts in the images, and one due to a very strong intensity inhomogeneity in the image. This result indicates that our segmentation algorithm is highly reliable in the absence of clear errors during the image acquisition.
4. Using our segmentation algorithm we performed a study on normalized spinal cord area with 146 MT-weighted cervical spinal cord images from healthy controls subjects and patients with MS. Statistically significant differences were found when comparing healthy controls against the entire MS group ( $p$ -value = 0.042), and when comparing secondary progressive patients against relapsing-remitting ( $p$ -value = 0.005) and primary progressive ( $p$ -value = 0.011) patients. These results are consistent with reports in existing literature, which used a semi-automatic or manual approach for their analysis. This suggests that our method can provide a viable fully automatic alternative for performing such analysis.
5. We evaluated Pearson's correlation coefficients between normalized spinal cord area and clinical measures of disability (EDSS) and disease duration by using semi-partial correlation to adjust for age and sex. Moderately weak, but significant relationships were found for normalized spinal cord area with both EDSS ( $r = -0.19$ ,  $p$ -value = 0.03) and disease duration ( $r = -0.23$ ,  $p$ -value = 0.01) when observing the whole MS group together. These result indicate that normalize spinal cord area measured using our algorithm can have potential clinical relevance as quantitative markers of disease progression and duration.

6. Using the CSF segmentations from our algorithm, we performed an exploratory analysis of normalized CSF area in MS. Our analysis showed a considerable trend of higher CSF in the progressive MS subtypes (SP and PP), with significant differences being found after adjusting for age and sex when compared against the RR subtype (p-value < 0.001 and p-value = 0.003, respectively), and between healthy controls and SP (p-value = 0.040). To our knowledge, normalized CSF area has never been analyzed in depth for MS, and our results suggest further investigation should be conducted to better understand how it is affected by the disease.

### **7.2.2 Relevance to MS Analysis**

Our automatic spinal cord MRI segmentation algorithm has improved the analysis of MS in two ways. First, our method is a fully automatic approach for acquiring spinal cord volumes and areas from MR images. Previous studies of such measures have relied on manual or semi-automatic approaches for segmenting the spinal cord. By removing the manual dependency, our method allows for much larger studies of spinal cord atrophy in MS, and provides a consistent quantitative measure that can potentially be used for clinical or therapeutic evaluation. Second, our algorithm is able to provide a segmentation of the CSF, which generally have not been segmented or analyzed in existing studies of MS. Measures using our CSF segmentation can potentially be a new avenue of exploration for studying the disease.

### **7.2.3 Future Work**

One main drawback of our segmentation approach is that a new set of atlases has to be constructed when facing new modalities or fields of view. While we have introduced a rapid approach for creating such atlases, the algorithm can be improved by removing this requirement. Ideally, we would use a single atlas that encompasses the entire spinal cord, and then use a registration algorithm that is very robust to modality and field of view changes to align the atlas. This improvement would allow our algorithm to be more accessible for new studies with different types of spinal cord data.

Another potential improvement to the algorithm is to extend the segmentation to include additional spinal cord structures. In our algorithm the spinal cord is segmented as a single structure. However, there is great interest in studying the white and grey matter columns in the spinal cord individually, since they serve different functions. In addition, the spinal cord can be segmented axially using the vertebral levels of the spine. These levels correspond with different areas of motor function (e.g., arms, legs, etc.); hence, the ability to perform analysis on the levels separately would enable studies to focus on specific areas of disability in the body.

## 7.3 Spinal Cord DTI Pipeline With Distortion Correction

### 7.3.1 Main Result

1. We developed a pipeline for performing diffusion tensor calculations using spinal cord diffusion weighted (DW) images. Our pipeline addressed one of the key challenges of working with spinal cord diffusion data, which is the presence of strong susceptibility distortion in the images. By using deformable registration and field of view matching to correct for this distortion, we have allowed more reliable diffusion tensor metrics to be produced for studying the microstructure of the spinal cord through diffusion.
2. Our pipeline was used to process DW images of the cervical spinal cord from 138 subjects. The accuracy and effectiveness of the distortion correction was qualitatively evaluated by a trained clinician by observing the accuracy of the field of view matching, the alignment of the registration, and the expected directions of diffusion anisotropy in the spinal cord.

### 7.3.2 Relevance to MS Analysis

The diffusion tensor metrics (FA, MD,  $\lambda_{\perp}, \lambda_{\parallel}$ ) calculated using our pipeline has directly enabled two studies of MS by our clinical collaborators, which explored differences in diffusion metrics between healthy control subjects and patients with MS [74], and their utility for discriminating between different levels of disability in MS patients [75]. These results suggest that the spinal cord DTI metrics calculated by our pipeline provide a useful tool for analyzing MS in the spinal cord.

### 7.3.3 Future Work

One aspect of susceptibility distortions that is not currently corrected by our pipeline is the “signal pile-up” in the distorted regions of the image. When multiple voxels are read into the same spatial location due to the susceptibility distortion, the scanner accumulates the signal from all these voxels. This causes the locations where the voxels are compressed to exhibit higher intensities, and the original locations of the distorted voxels to exhibit lower intensities. One potential improvement to the pipeline is to correct the image intensities by using the degree of compression and expansion in the deformation fields to rescale the intensity values.

## 7.4 Deformable Registration for Retinal OCT

### 7.4.1 Main Result

1. We developed a deformable registration approach for aligning retinal OCT. Our algorithm was designed to respect the scan geometry of the OCT by imposing strict constraints that only allows rigid translations of the A-scans and transformations parallel to the A-scan directions.
2. Our OCT registration algorithm was validated by using manual segmentations of the retinal layers to evaluate the algorithm's ability to correctly align the layers between different subjects. Calculated over 200 registrations, our algorithm produced an average Dice overlap of 0.77 over the eight retinal layers. This was significantly better than using a generic registration algorithm such as SyN, which had an average Dice of 0.40 over the eight retinal layers.
3. The manual segmentations were also used to evaluate the average layer boundary surface errors after registration. Our algorithm produced an average error of  $8 \mu m$  across the eight retinal layers. Again, this was significantly better than SyN which produced an average error of  $36.8 \mu m$ .
4. Using our registration algorithm, we constructed an average atlas of the macular using OCT images from 40 healthy volunteers. To our knowledge, this is the first time a 3D atlas space has been constructed for the human macula. Such a space is useful for normalization and making comparisons of the macula between different individuals and populations.
5. Using the macular average atlas and the manual retinal layer segmentations for each of the healthy volunteers, we constructed a statistical atlas of the eight retinal layers in our segmentations. Such an atlas is useful for understanding the relative spatial distribution of the retinal layers, and can be used as prior information to help initialize segmentation algorithms.
6. Using the macular average atlas space, we performed a RAVENS analysis between 40 healthy control subjects and 43 MS patients. SPM was used to detect the voxels in the average atlas where the two cohorts had statistically significant differences in RAVENS measures. The analysis showed significant differences in regions of the retina that is consistent with previous findings on retinal layer changes in MS. The advantage of our analysis is the ability to detect where specifically in the 3D image such changes are occurring, whereas previous analysis relied on average OCT thickness calculated across 2D regions of the macula or post-mortem histology.

### 7.4.2 Relevance to MS Analysis

Our deformable registration algorithm opens up a number of deformation and atlas based techniques for retinal OCT that can be used to study MS, as demonstrated by our RAVENS analysis. In addition, the average atlas space allows us to compare and evaluate morphological differences between

individuals and populations, as oppose to being limited to layer thickness or volume comparisons. Lastly, our statistical atlas provides a valuable tool that can be used to improve the accuracy and robustness of retinal layer segmentation approaches that are currently used to study MS.

### **7.4.3 Future Work**

One limitation of our registration algorithm is that the constraints do not account for possible shifts of the entry point on the pupil during the OCT scan. Hence, if the scan is acquired off-centered, then the fovea translation used in the algorithm is a very poor approximation for rigidly aligning the A-scans.

A major improvement for the registration algorithm would be to correct for the actual OCT geometry in the image. This would allow the registration to be performed in physical space, and remove the need for it to be constrained to the A-scan direction. Unfortunately, this is a difficult problem to solve using just the OCT image, because the scan geometry depends on each individual's eye. However, we can potentially use external measurements such as the axial length or the curvature of the eye to perform this correction.

## **7.5 Multi-channel Registration of Brain MRI**

### **7.5.1 Main Results**

1. We developed a multi-channel registration framework based on the ABA registration algorithm. The framework allows the algorithm to use multiple modalities for the source and target images simultaneously to better align the brain in MR images.
2. Our multi-channel framework was validated by applying a known deformation to T1w and T2w phantom MR brain data, and using the registration to recover the deformations. The results showed that when performing only single channel registrations, T1w images performed better when the applied deformation was small, while the T2w registrations performed better when the deformation was large. However, when using both T1w and T2w in a multi-channel registration, the algorithm performed on par with single channel T1w for small deformations, but also on par with single channel T2w for large deformations.
3. The known deformation recovery experiment was repeated for real T1w and T2w MR brain data. In this case, the T1w single channel registrations performed better than the T2w single channel registration regardless of the deformation size. However, when a large deformation was applied, the multi-channel result using both T1w and T2w images was better than the single channel T1w result. This supports the idea that our multi-channel registration can be used to combine features and information from multiple modalities to improve the overall registration.

4. Using the multi-channel framework we addressed two challenges in image registration. First, we used the multi-channel registration with distance transforms to address the limitations of the mutual information cost function in areas with homogeneous intensities. We then used the framework with image synthesis to fill in incomplete channels when facing registration problems where there are missing data, such as when the source and target images are different modalities.
5. The effectiveness of using white matter distance transforms as a second channel was evaluated by calculating Dice overlap on the grey matter, white matter, and “putamen+caudate” segmentations between a registered image and a target image. Averaged over 10 registrations, the three structures increased in average Dice by 1.45%, 1.33% and 3.23%, respectively, after adding the white matter distance transforms to the MR registration.
6. To evaluate using image synthesis with our multi-channel framework to perform multi-modal registration, we performed 10 deformation recovery experiments using different sinusoidal deformation fields on phantom brain data. Results showed that using synthetic images with SSD in our multi-channel ABA framework performed significantly better ( $p < 0.01$ ) intra-subject cross-modal registrations than single channel ABA with mutual information. The average recovery error for the multi-channel result was 0.09 voxels, while the average recovery error for the single channel result was 0.25 voxels.
7. Using qualitative comparisons with edge map boundaries, we showed that using our multi-channel framework with synthetic images produced better registrations between T1w and T2w images from the same subject than single channel rigid or deformable registration with NMI. This was particularly evident in the ventricles where the single channel registrations showed clear errors in alignment.
8. One hundred inter-subject registrations were performed using both single channel ABA with NMI and multi-channel ABA with synthetic images and SDD. MindBoggle cortical labels and TOADS cerebrum labels were used to evaluate the label transfer capabilities of both methods. Dice overlap calculated between the transferred labels and the target label showed that the multi-channel approach was significantly better ( $p < 0.001$ ) at aligning both label sets than the single channel approach. For the MindBoggle labels the single channel approach produced an average Dice of 0.312 over all the labels while the multi-channel approach produced an average Dice of 0.350. For the TOADS labels the single channel approach produced an average Dice of 0.702 while the multi-channel approach produced an average Dice of 0.752.

## 7.5.2 Relevance to MS Analysis

Currently, deformable registration based analysis of the brain is being used to study grey matter atrophy [139, 140] and to observe longitudinal changes [141] in MS. In addition, non-standard MR modalities, such as FLAIR [119] or susceptibility weighted [120] sequences, have been shown to be useful for observing MS pathology. Our multi-channel registration framework provides a logical next step for



improving existing deformation based analysis of MS by including these alternate modalities as additional channels in the registration. This allows the algorithm to use their features to improve registration accuracy and provide finer detection of MS related changes in the brain.

### **7.5.3 Future work**

In our experiments, we have relied on using only two channels during the registrations. However, the multi-channel framework is designed to be generalizable for any number of channels. This means that the registration can potentially include distance transforms from multiple structures in the brain, or synthetic images of additional external modalities, or a combination of both in the same registration. One potential future direction for this work is to evaluate the benefits of using more than two channels of information in the registration, and establishing when additional channels are no longer useful.

## **7.6 Conclusion**

Deformable image registration is a valuable tool for the analysis of disease. In this dissertation, we have shown its application for solving a wide array of problems, including segmentation, distortion correction, atlas construction, and population analysis. We were able to adapt the same general registration framework to work with images of three different anatomical structures, each with their own imaging characteristics and challenges. Using deformable image registration, we have developed several advanced techniques that have enable previously unavailable analysis of multiple sclerosis. It is our hope that these techniques will lead to larger studies of MS that can improve our understanding of the disease.

# Bibliography

- [1] P. E. Anuta, "Spatial registration of multispectral and multitemporal digital imagery using fast Fourier transform techniques," *Geoscience Electronics, IEEE Transactions on*, vol. 8, no. 4, pp. 353–368, 1970.
- [2] A. Sotiras, C. Davatzikos, and N. Paragios, "Deformable medical image registration: A survey," *Medical Imaging, IEEE Transactions on*, vol. 32, no. 7, pp. 1153–1190, 2013.
- [3] J. P. Pluim, J. A. Maintz, and M. A. Viergever, "Mutual-information-based registration of medical images: A survey," *Medical Imaging, IEEE Transactions on*, vol. 22, no. 8, pp. 986–1004, 2003.
- [4] A. F. Goldszal, C. Davatzikos, D. L. Pham, M. X. Yan, R. N. Bryan, and S. M. Resnick, "An image-processing system for qualitative and quantitative volumetric analysis of brain images," *Journal of Computer Assisted Tomography*, vol. 22, no. 5, pp. 827–837, 1998.
- [5] G. K. Rohde, A. Aldroubi, and B. M. Dawant, "The adaptive bases algorithm for intensity-based nonrigid image registration," *Medical Imaging, IEEE Transactions on*, vol. 22, no. 11, pp. 1470–1479, 2003.
- [6] B. B. Avants, C. L. Epstein, M. Grossman, and J. C. Gee, "Symmetric diffeomorphic image registration with cross-correlation: Evaluating automated labeling of elderly and neurodegenerative brain," *Medical Image Analysis*, vol. 12, no. 1, pp. 26–41, 2008.
- [7] F. L. Bookstein, "Principal warps: Thin-plate splines and the decomposition of deformations," *Pattern Analysis and Machine Intelligence, IEEE Transactions on*, vol. 11, no. 6, pp. 567–585, 1989.
- [8] J. C. Gee and R. K. Bajcsy, "Elastic matching: Continuum mechanical and probabilistic analysis," *Brain Warping*, vol. 2, 1998.
- [9] G. E. Christensen, R. D. Rabbitt, and M. I. Miller, "Deformable templates using large deformation kinematics," *Image Processing, IEEE Transactions on*, vol. 5, no. 10, pp. 1435–1447, 1996.
- [10] J.-P. Thirion, "Image matching as a diffusion process: An analogy with Maxwell's demons," *Medical Image Analysis*, vol. 2, no. 3, pp. 243–260, 1998.

- [11] M. F. Beg, M. I. Miller, A. Trouvé, and L. Younes, “Computing large deformation metric mappings via geodesic flows of diffeomorphisms,” *International Journal of Computer Vision*, vol. 61, no. 2, pp. 139–157, 2005.
- [12] J. Ashburner and K. J. Friston, “Voxel-based morphometry—the methods,” *NeuroImage*, vol. 11, no. 6, pp. 805–821, 2000.
- [13] C. Davatzikos, A. Genc, D. Xu, and S. M. Resnick, “Voxel-based morphometry using the RAVENS maps: Methods and validation using simulated longitudinal atrophy,” *NeuroImage*, vol. 14, no. 6, pp. 1361–1369, 2001.
- [14] W. M. Wells III, P. Viola, H. Atsumi, S. Nakajima, and R. Kikinis, “Multi-modal volume registration by maximization of mutual information,” *Medical Image Analysis*, vol. 1, no. 1, pp. 35–51, 1996.
- [15] C. E. Shannon, “A mathematical theory of communication,” *Bell System Technical Journal*, vol. 27, no. 379-423, 1948.
- [16] C. Studholme, D. L. Hill, and D. J. Hawkes, “An overlap invariant entropy measure of 3D medical image alignment,” *Pattern Recognition*, vol. 32, no. 1, pp. 71–86, 1999.
- [17] A. Andronache, M. von Siebenthal, G. Székely, and P. Cattin, “Non-rigid registration of multi-modal images using both mutual information and cross-correlation,” *Medical Image Analysis*, vol. 12, no. 1, pp. 3–15, 2008.
- [18] F. Maes, D. Vandermeulen, and P. Suetens, “Medical image registration using mutual information,” *Proceedings of the IEEE*, vol. 91, no. 10, pp. 1699–1722, 2003.
- [19] A. Klein, S. S. Ghosh, B. Avants, B. T. Yeo, B. Fischl, B. Ardekani, J. C. Gee, J. J. Mann, and R. V. Parsey, “Evaluation of volume-based and surface-based brain image registration methods,” *NeuroImage*, vol. 51, no. 1, pp. 214–220, 2010.
- [20] A. Klein, J. Andersson, B. A. Ardekani, J. Ashburner, B. Avants, M.-C. Chiang, G. E. Christensen, D. L. Collins, J. Gee, P. Hellier *et al.*, “Evaluation of 14 nonlinear deformation algorithms applied to human brain MRI registration,” *NeuroImage*, vol. 46, no. 3, pp. 786–802, 2009.
- [21] K. Murphy, B. Van Ginneken, J. M. Reinhardt, S. Kabus, K. Ding, X. Deng, K. Cao, K. Du, G. E. Christensen, V. Garcia *et al.*, “Evaluation of registration methods on thoracic CT: The EMPIRE10 challenge,” *Medical Imaging, IEEE Transactions on*, vol. 30, no. 11, pp. 1901–1920, 2011.
- [22] M. Trisolini, A. Honeycutt, J. Wiener, and S. Lesesne, “Global economic impact of multiple sclerosis,” *London (United Kingdom): Multiple Sclerosis International Federation*, 2010.
- [23] J. D. Campbell, V. Ghushchyan, R. Brett McQueen, S. Cahoon-Metzger, T. Livingston, T. Vollmer, J. Corboy, A. Miravalle, T. Schreiner, V. Porter *et al.*, “Burden of multiple sclerosis on direct, indirect

- costs and quality of life: National US estimates,” *Multiple Sclerosis and Related Disorders*, vol. 3, no. 2, pp. 227–236, 2014.
- [24] N. Losseff, S. Webb, J. O’riordan, R. Page, L. Wang, G. Barker, P. Tofts, W. McDonald, D. Miller, and A. Thompson, “Spinal cord atrophy and disability in multiple sclerosis: A new reproducible and sensitive MRI method with potential to monitor disease progression,” *Brain*, vol. 119, no. 3, pp. 701–708, 1996.
- [25] E. M. Haacke, R. W. Brown, M. R. Thompson, and R. Venkatesan, “Magnetic resonance imaging,” *Physical Principles and Sequence Design*, 1999.
- [26] J. F. Kurtzke, “Rating neurologic impairment in multiple sclerosis an expanded disability status scale (EDSS),” *Neurology*, vol. 33, no. 11, pp. 1444–1444, 1983.
- [27] N. Kalkers, F. Barkhof, E. v. Bergers, R. Van Schijndel, and C. Polman, “The effect of the neuroprotective agent riluzole on MRI parameters in primary progressive multiple sclerosis: A pilot study,” *Multiple Sclerosis*, vol. 8, no. 6, pp. 532–533, 2002.
- [28] X. Lin, C. Tench, B. Turner, L. Blumhardt, and C. Constantinescu, “Spinal cord atrophy and disability in multiple sclerosis over four years: Application of a reproducible automated technique in monitoring disease progression in a cohort of the interferon  $\beta$ -1a (Rebif) treatment trial,” *Journal of Neurology, Neurosurgery & Psychiatry*, vol. 74, no. 8, pp. 1090–1094, 2003.
- [29] X. Lin, C. R. Tench, N. Evangelou, T. Jaspan, and C. S. Constantinescu, “Measurement of spinal cord atrophy in multiple sclerosis,” *Journal of Neuroimaging*, vol. 14, no. s3, pp. 20S–26S, 2004.
- [30] K. M. Zackowski, S. A. Smith, D. S. Reich, E. Gordon-Lipkin, B. A. Chodkowski, D. R. Sambandan, M. Shteyman, A. J. Bastian, P. C. van Zijl, and P. A. Calabresi, “Sensorimotor dysfunction in multiple sclerosis and column-specific magnetization transfer-imaging abnormalities in the spinal cord,” *Brain*, vol. 132, pp. 1200–1209, 2009.
- [31] M. Rocca, M. Horsfield, S. Sala, M. Copetti, P. Valsasina, S. Mesaros, V. Martinelli, D. Caputo, T. Stosic-Opincal, J. Drulovic *et al.*, “A multicenter assessment of cervical cord atrophy among MS clinical phenotypes,” *Neurology*, vol. 76, no. 24, pp. 2096–2102, 2011.
- [32] P. Freund, N. Weiskopf, N. S. Ward, C. Hutton, A. Gall, O. Ciccarelli, M. Craggs, K. Friston, and A. J. Thompson, “Disability, atrophy and cortical reorganization following spinal cord injury,” *Brain*, vol. 134, pp. 1610–1622, 2011.
- [33] N. Archip, P.-J. Erard, M. Egmont-Petersen, J.-M. Haefliger, and J.-F. Germond, “A knowledge-based approach to automatic detection of the spinal cord in CT images,” *Medical Imaging, IEEE Transactions on*, vol. 21, no. 12, pp. 1504–1516, 2002.

- [34] G. Karangelis and S. Zimeras, "An accurate 3D segmentation method of the spinal canal applied to CT data," in *Bildverarbeitung für die Medizin 2002*. Springer, 2002, pp. 370–373.
- [35] S. S. Burnett, G. Starkschall, C. W. Stevens, and Z. Liao, "A deformable-model approach to semi-automatic segmentation of CT images demonstrated by application to the spinal canal," *Medical physics*, vol. 31, no. 2, pp. 251–263, 2004.
- [36] L. G. Nyúl, J. Kanyó, E. Máté, G. Makay, E. Balogh, M. Fidrich, and A. Kuba, "Method for automatically segmenting the spinal cord and canal from 3D CT images," in *Computer Analysis of Images and Patterns*, 2005, pp. 456–463.
- [37] J. C. McGowan and R. S. Patel, "Technical issues for MRI examination of the posterior fossa," *Journal of the Neurological Sciences*, vol. 172, pp. S40–S42, 2000.
- [38] L. F. Czervionke, J. M. Czervionke, D. L. Daniels, and V. M. Houghton, "Characteristic features of MR truncation artifacts," *American Journal of Neuroradiology*, vol. 9, no. 5, pp. 815–824, 1988.
- [39] M. Bronskill, E. McVeigh, W. Kucharczyk, and R. Henkelman, "Syrinx-like artifacts on MR images of the spinal cord," *Radiology*, vol. 166, no. 2, pp. 485–488, 1988.
- [40] A. J. Curtin, D. W. Chakeres, R. Bulas, C. P. Boesel, M. Finneran, and E. Flint, "MR imaging artifacts of the axial internal anatomy of the cervical spinal cord," *American Journal of Neuroradiology*, vol. 10, no. 1, pp. 19–26, 1989.
- [41] R. Hinks and R. Quencer, "Motion artifacts in brain and spine MR," *Radiologic Clinics of North America*, vol. 26, no. 4, pp. 737–753, 1988.
- [42] L. M. Levy, G. Di Chiro, R. A. Brooks, A. Dwyer, L. Wener, and J. Frank, "Spinal cord artifacts from truncation errors during MR imaging," *Radiology*, vol. 166, no. 2, pp. 479–483, 1988.
- [43] G. Lycklama, A. Thompson, M. Filippi, D. Miller, C. Polman, F. Fazekas, and F. Barkhof, "Spinal-cord MRI in multiple sclerosis," *The Lancet Neurology*, vol. 2, no. 9, pp. 555–562, 2003.
- [44] O. Coulon, S. Hickman, G. Parker, G. Barker, D. Miller, and S. Arridge, "Quantification of spinal cord atrophy from magnetic resonance images via a b-spline active surface model," *Magnetic Resonance in Medicine*, vol. 47, no. 6, pp. 1176–1185, 2002.
- [45] R. Van Uitert, I. Bitter, and J. A. Butman, "Semi-automatic spinal cord segmentation and quantification," in *International Congress Series*, vol. 1281, 2005, pp. 224–229.
- [46] M. A. Horsfield, S. Sala, M. Neema, M. Absinta, A. Bakshi, M. P. Sormani, M. A. Rocca, R. Bakshi, and M. Filippi, "Rapid semi-automatic segmentation of the spinal cord from magnetic resonance images: Application in multiple sclerosis," *NeuroImage*, vol. 50, no. 2, pp. 446–455, 2010.

- [47] M. Nieniewski and R. Serneels, "Segmentation of spinal cord images by means of watershed and region merging together with inhomogeneity correction," *Machine Graphics and Vision*, vol. 11, no. 1, pp. 101–122, 2002.
- [48] C. McIntosh and G. Hamarneh, "Spinal crawlers: Deformable organisms for spinal cord segmentation and analysis," in *Medical Image Computing and Computer-Assisted Intervention—MICCAI 2006*, 2006, pp. 808–815.
- [49] J. Koh, T. Kim, V. Chaudhary, and G. Dhillon, "Automatic segmentation of the spinal cord and the dural sac in lumbar MR images using gradient vector flow field," in *Engineering in Medicine and Biology Society (EMBC), 2010 Annual International Conference of the IEEE*, 2010, pp. 3117–3120.
- [50] J. Koh, P. D. Scott, V. Chaudhary, and G. Dhillon, "An automatic segmentation method of the spinal canal from clinical MR images based on an attention model and an active contour model," in *Biomedical Imaging: From Nano to Macro, 8th IEEE International Symposium on*, 2011, pp. 1467–1471.
- [51] D. P. Mukherjee, I. Cheng, N. Ray, V. Mushahwar, M. Lebel, and A. Basu, "Automatic segmentation of spinal cord MRI using symmetric boundary tracing," *Information Technology in Biomedicine, IEEE transactions on*, vol. 14, no. 5, p. 1275, 2010.
- [52] C. Xu and J. L. Prince, "Snakes, shapes, and gradient vector flow," *Image Processing, IEEE Transactions on*, vol. 7, no. 3, pp. 359–369, 1998.
- [53] M. Kass, A. Witkin, and D. Terzopoulos, "Snakes: Active contour models," *International Journal of Computer Vision*, vol. 1, no. 4, pp. 321–331, 1988.
- [54] J. C. Bezdek, "A convergence theorem for the fuzzy ISODATA clustering algorithms," *Pattern Analysis and Machine Intelligence, IEEE Transactions on*, vol. 2, no. 1, pp. 1–8, 1980.
- [55] D. L. Pham, "Spatial models for fuzzy clustering," *Computer Vision and Image Understanding*, vol. 84, no. 2, pp. 285–297, 2001.
- [56] J. G. Sled, A. P. Zijdenbos, and A. C. Evans, "A nonparametric method for automatic correction of intensity nonuniformity in MRI data," *Medical Imaging, IEEE Transactions on*, vol. 17, no. 1, pp. 87–97, 1998.
- [57] P.-L. Bazin and D. L. Pham, "Homeomorphic brain image segmentation with topological and statistical atlases," *Medical Image Analysis*, vol. 12, no. 5, pp. 616–625, 2008.
- [58] A. Carass, J. Cuzzocreo, M. B. Wheeler, P.-L. Bazin, S. M. Resnick, and J. L. Prince, "Simple paradigm for extra-cerebral tissue removal: Algorithm and analysis," *NeuroImage*, vol. 56, no. 4, pp. 1982–1992, 2011.

- [59] M. Chen, A. Carass, J. Cuzzocreo, P.-L. Bazin, D. S. Reich, and J. L. Prince, "Topology preserving automatic segmentation of the spinal cord in magnetic resonance images," in *Biomedical Imaging: From Nano to Macro, 8th IEEE International Symposium on*, 2011, pp. 1737–1740.
- [60] P.-L. Bazin and D. L. Pham, "Topology-preserving tissue classification of magnetic resonance brain images," *Medical Imaging, IEEE Transactions on*, vol. 26, no. 4, pp. 487–496, 2007.
- [61] S. A. Smith, C. K. Jones, A. Gifford, V. Belegu, B. Chodkowski, J. A. Farrell, B. A. Landman, D. S. Reich, P. A. Calabresi, J. W. McDonald *et al.*, "Reproducibility of tract-specific magnetization transfer and diffusion tensor imaging in the cervical spinal cord at 3 tesla," *NMR in Biomedicine*, vol. 23, no. 2, pp. 207–217, 2010.
- [62] L. R. Dice, "Measures of the amount of ecologic association between species," *Ecology*, vol. 26, no. 3, pp. 297–302, 1945.
- [63] B. C. Healy, A. Arora, D. L. Hayden, A. Ceccarelli, S. S. Tauhid, M. Neema, and R. Bakshi, "Approaches to normalization of spinal cord volume: Application to multiple sclerosis," *Journal of Neuroimaging*, vol. 22, no. 3, pp. e12–e19, 2012.
- [64] M. Chen, A. Carass, J. Oh, G. Nair, D. L. Pham, D. S. Reich, and J. L. Prince, "Automatic magnetic resonance spinal cord segmentation with topology constraints for variable fields of view," *NeuroImage*, vol. 83, pp. 1051–1062, 2013.
- [65] E. O. Stejskal and J. E. Tanner, "Spin diffusion measurements: Spin echoes in the presence of a time-dependent field gradient," *The Journal of Chemical Physics*, vol. 42, no. 1, pp. 288–292, 1965.
- [66] M. A. Horsfield and D. K. Jones, "Applications of diffusion-weighted and diffusion tensor MRI to white matter diseases—a review," *NMR in Biomedicine*, vol. 15, no. 7-8, pp. 570–577, 2002.
- [67] P. J. Basser, J. Mattiello, and D. LeBihan, "MR diffusion tensor spectroscopy and imaging," *Biophysical Journal*, vol. 66, no. 1, pp. 259–267, 1994.
- [68] B. A. Landman, J. A. Farrell, N. Patel, S. Mori, and J. L. Prince, "DTI fiber tracking: The importance of adjusting DTI gradient tables for motion correction. CATNAP—A tool to simplify and accelerate DTI analysis," in *Proc. Org Human Brain Mapping 13th Annual Meeting*, vol. 138, 2007.
- [69] P. J. Basser and D. K. Jones, "Diffusion-tensor MRI: Theory, experimental design and data analysis—a technical review," *NMR in Biomedicine*, vol. 15, no. 7-8, pp. 456–467, 2002.
- [70] P. Jezzard and R. S. Balaban, "Correction for geometric distortion in echo planar images from b0 field variations," *Magnetic Resonance in Medicine*, vol. 34, no. 1, pp. 65–73, 1995.
- [71] J. Kybic, P. Thévenaz, A. Nirkko, and M. Unser, "Unwarping of unidirectionally distorted EPI images," *Medical Imaging, IEEE Transactions on*, vol. 19, no. 2, pp. 80–93, 2000.

- [72] Y. Li, N. Xu, J. M. Fitzpatrick, V. L. Morgan, D. R. Pickens, and B. M. Dawant, "Accounting for signal loss due to dephasing in the correction of distortions in gradient-echo EPI via nonrigid registration," *Medical Imaging, IEEE Transactions on*, vol. 26, no. 12, pp. 1698–1707, 2007.
- [73] B. C. Lucas, J. A. Bogovic, A. Carass, P.-L. Bazin, J. L. Prince, D. L. Pham, and B. A. Landman, "The Java Image Science Toolkit (JIST) for rapid prototyping and publishing of neuroimaging software," *Neuroinformatics*, vol. 8, no. 1, pp. 5–17, 2010.
- [74] J. Oh, K. Zackowski, M. Chen, S. Newsome, S. Saidha, S. A. Smith, M. Diener-West, J. Prince, C. K. Jones, P. C. Van Zijl *et al.*, "Multiparametric MRI correlates of sensorimotor function in the spinal cord in multiple sclerosis," *Multiple Sclerosis Journal*, vol. 19, no. 4, pp. 427–435, 2013.
- [75] J. Oh, S. Saidha, M. Chen, S. A. Smith, J. Prince, C. Jones, M. Diener-West, P. C. van Zijl, D. S. Reich, and P. A. Calabresi, "Spinal cord quantitative MRI discriminates between disability levels in multiple sclerosis," *Neurology*, vol. 80, no. 6, pp. 540–547, 2013.
- [76] E. M. Frohman, J. G. Fujimoto, T. C. Frohman, P. A. Calabresi, G. Cutter, and L. J. Balcer, "Optical coherence tomography: A window into the mechanisms of multiple sclerosis," *Nature Clinical Practice Neurology*, vol. 4, no. 12, pp. 664–675, 2008.
- [77] J. N. Ratchford, S. Saidha, E. S. Sotirchos, J. A. Oh, M. A. Seigo, C. Eckstein, M. K. Durbin, J. D. Oakley, S. A. Meyer, A. Conger *et al.*, "Active MS is associated with accelerated retinal ganglion cell/inner plexiform layer thinning," *Neurology*, vol. 80, no. 1, pp. 47–54, 2013.
- [78] S. Saidha, E. S. Sotirchos, J. Oh, S. B. Syc, M. A. Seigo, N. Shiee, C. Eckstein, M. K. Durbin, J. D. Oakley, S. A. Meyer *et al.*, "Relationships between retinal axonal and neuronal measures and global central nervous system pathology in multiple sclerosis," *JAMA Neurology*, vol. 70, no. 1, pp. 34–43, 2013.
- [79] J. M. Gelfand, R. Nolan, D. M. Schwartz, J. Graves, and A. J. Green, "Microcystic macular oedema in multiple sclerosis is associated with disease severity," *Brain*, vol. 135, no. 6, pp. 1786–1793, 2012.
- [80] D. Koozekanani, K. Boyer, and C. Roberts, "Retinal thickness measurements from optical coherence tomography using a Markov boundary model," *Medical Imaging, IEEE Transactions on*, vol. 20, no. 9, pp. 900–916, 2001.
- [81] H. Ishikawa, D. M. Stein, G. Wollstein, S. Beaton, J. G. Fujimoto, and J. S. Schuman, "Macular segmentation with optical coherence tomography," *Investigative Ophthalmology & Visual Science*, vol. 46, no. 6, pp. 2012–2017, 2005.
- [82] M. K. Garvin, M. D. Abramoff, R. Kardon, S. R. Russell, X. Wu, and M. Sonka, "Intraretinal layer segmentation of macular optical coherence tomography images using optimal 3-D graph search," *Medical Imaging, IEEE Transactions on*, vol. 27, no. 10, pp. 1495–1505, 2008.



- [83] S. J. Chiu, X. T. Li, P. Nicholas, C. A. Toth, J. A. Izatt, and S. Farsiu, "Automatic segmentation of seven retinal layers in SDOCT images congruent with expert manual segmentation," *Optics Express*, vol. 18, no. 18, pp. 19413–19428, 2010.
- [84] A. Lang, A. Carass, E. Sotirchos, P. Calabresi, and J. L. Prince, "Segmentation of retinal OCT images using a random forest classifier," in *Proceedings of SPIE Medical Imaging 2013*, 2013, p. 86690R.
- [85] A. Lang, A. Carass, M. Hauser, E. S. Sotirchos, P. A. Calabresi, H. S. Ying, and J. L. Prince, "Retinal layer segmentation of macular OCT images using boundary classification," *Biomedical Optics Express*, vol. 4, no. 7, pp. 1133–1152, 2013.
- [86] T. M. Jørgensen, U. Christensen, W. Soliman, J. Thomadsen, and B. Sander, "Enhancing the signal-to-noise ratio in ophthalmic optical coherence tomography by image registration—method and clinical examples," *Journal of Biomedical Optics*, vol. 12, no. 4, pp. 041208–041208, 2007.
- [87] J. Xu, H. Ishikawa, G. Wollstein, L. Kagemann, and J. S. Schuman, "Alignment of 3-D optical coherence tomography scans to correct eye movement using a particle filtering," *Medical Imaging, IEEE Transactions on*, vol. 31, no. 7, pp. 1337–1345, 2012.
- [88] Y. M. Liew, R. A. McLaughlin, F. M. Wood, and D. D. Sampson, "Motion correction of in vivo three-dimensional optical coherence tomography of human skin using a fiducial marker," *Biomedical Optics Express*, vol. 3, no. 8, pp. 1774–1786, 2012.
- [89] A. Giani, M. Pellegrini, A. Invernizzi, M. Cigada, and G. Staurenghi, "Aligning scan locations from consecutive spectral-domain optical coherence tomography examinations: A comparison among different strategies," *Investigative Ophthalmology & Visual Science*, vol. 53, no. 12, pp. 7637–7643, 2012.
- [90] M. Niemeijer, M. K. Garvin, K. Lee, B. van Ginneken, M. D. Abramoff, and M. Sonka, "Registration of 3D spectral OCT volumes using 3D SIFT feature point matching," in *Proceedings of SPIE Medical Imaging 2009*, 2009, p. 72591I.
- [91] M. Niemeijer, K. Lee, M. K. Garvin, M. D. Abramoff, and M. Sonka, "Registration of 3D spectral OCT volumes combining ICP with a graph-based approach," in *Proceedings of SPIE Medical Imaging 2012*, 2012, p. 83141A.
- [92] M. Chen, A. Lang, E. Sotirchos, H. S. Ying, P. A. Calabresi, J. L. Prince, and A. Carass, "Deformable registration of macular OCT using A-mode scan similarity," in *Biomedical Imaging: From Nano to Macro, 10th International Symposium on*, 2013, pp. 476–479.
- [93] E. Gibson, M. Young, M. V. Sarunic, and M. F. Beg, "Optic nerve head registration via hemispherical surface and volume registration," *Biomedical Engineering, IEEE Transactions on*, vol. 57, no. 10, pp. 2592–2595, 2010.

- [94] B. Antony, M. D. Abramoff, L. Tang, W. D. Ramdas, J. R. Vingerling, N. M. Jansonius, K. Lee, Y. H. Kwon, M. Sonka, and M. K. Garvin, "Automated 3-D method for the correction of axial artifacts in spectral-domain optical coherence tomography images," *Biomedical Optics Express*, vol. 2, no. 8, pp. 2403–2416, 2011.
- [95] Y. Zheng, R. Xiao, Y. Wang, and J. C. Gee, "A generative model for OCT retinal layer segmentation by integrating graph-based multi-surface searching and image registration," in *Medical Image Computing and Computer-Assisted Intervention—MICCAI 2013*, 2013, pp. 428–435.
- [96] Y. Ou, A. Sotiras, N. Paragios, and C. Davatzikos, "DRAMMS: Deformable registration via attribute matching and mutual-saliency weighting," *Medical Image Analysis*, vol. 15, no. 4, pp. 622–639, 2011.
- [97] A. N. Kuo, R. P. McNabb, S. J. Chiu, M. A. El-Dairi, S. Farsiu, C. A. Toth, and J. A. Izatt, "Correction of ocular shape in retinal optical coherence tomography and effect on current clinical measures," *American Journal of Ophthalmology*, vol. 156, no. 2, pp. 304–311, 2013.
- [98] E. A. Maguire, D. G. Gadian, I. S. Johnsrude, C. D. Good, J. Ashburner, R. S. Frackowiak, and C. D. Frith, "Navigation-related structural change in the hippocampi of taxi drivers," *Proceedings of the National Academy of Sciences*, vol. 97, no. 8, pp. 4398–4403, 2000.
- [99] C. D. Good, I. S. Johnsrude, J. Ashburner, R. N. Henson, K. Fristen, and R. S. Frackowiak, "A voxel-based morphometric study of ageing in 465 normal adult human brains," in *Biomedical Imaging, 5th IEEE EMBS International Summer School on*, 2002, p. 16.
- [100] R. P. Brent, "An algorithm with guaranteed convergence for finding a zero of a function," *The Computer Journal*, vol. 14, no. 4, pp. 422–425, 1971.
- [101] A. Guimond, J. Meunier, and J.-P. Thirion, "Average brain models: A convergence study," *Computer Vision and Image Understanding*, vol. 77, no. 2, pp. 192–210, 2000.
- [102] B. Avants and J. C. Gee, "Geodesic estimation for large deformation anatomical shape averaging and interpolation," *NeuroImage*, vol. 23, pp. S139–S150, 2004.
- [103] S. Khullar, A. M. Michael, N. D. Cahill, K. A. Kiehl, G. Pearlson, S. A. Baum, and V. D. Calhoun, "ICA-fNORM: Spatial normalization of fMRI data using intrinsic group-ICA networks," *Frontiers in Systems Neuroscience*, vol. 5, 2011.
- [104] D. Rueckert, A. F. Frangi, and J. A. Schnabel, "Automatic construction of 3D statistical deformation models using non-rigid registration," in *Medical Image Computing and Computer-Assisted Intervention—MICCAI 2001*, 2001, pp. 77–84.

- [105] M. Chen, A. Carass, D. S. Reich, P. A. Calabresi, D. Pham, and J. L. Prince, "Voxel-wise displacement as independent features in classification of multiple sclerosis," in *Proceedings of SPIE Medical Imaging 2013*, 2013, p. 86690K.
- [106] S. Gerber, T. Tasdizen, P. Thomas Fletcher, S. Joshi, and R. Whitaker, "Manifold modeling for brain population analysis," *Medical Image Analysis*, vol. 14, no. 5, pp. 643–653, 2010.
- [107] Y. Fan, S. M. Resnick, X. Wu, and C. Davatzikos, "Structural and functional biomarkers of prodromal alzheimer's disease: A high-dimensional pattern classification study," *NeuroImage*, vol. 41, no. 2, pp. 277–285, 2008.
- [108] S. Saidha, E. S. Sotirchos, M. A. Ibrahim, C. M. Crainiceanu, J. M. Gelfand, Y. J. Sepah, J. N. Ratchford, J. Oh, M. A. Seigo, S. D. Newsome *et al.*, "Microcystic macular oedema, thickness of the inner nuclear layer of the retina, and disease characteristics in multiple sclerosis: A retrospective study," *The Lancet Neurology*, vol. 11, no. 11, pp. 963–972, 2012.
- [109] M. I. Miller, G. E. Christensen, Y. Amit, and U. Grenander, "Mathematical textbook of deformable neuroanatomies," *Proceedings of the National Academy of Sciences*, vol. 90, no. 24, pp. 11 944–11 948, 1993.
- [110] K. J. Friston, W. D. Penny, J. Ashburner, S. J. Kiebel, and T. E. Nichols, *Statistical parametric mapping: The analysis of functional brain images*. Academic Press, 2006.
- [111] J. B. Kerrison, T. Flynn, and W. R. Green, "Retinal pathologic changes in multiple sclerosis," *Retina*, vol. 14, no. 5, pp. 445–451, 1994.
- [112] A. J. Green, S. McQuaid, S. L. Hauser, I. V. Allen, and R. Lyness, "Ocular pathology in multiple sclerosis: Retinal atrophy and inflammation irrespective of disease duration," *Brain*, vol. 133, no. 6, pp. 1591–1601, 2010.
- [113] B. J. Lujan, A. Roorda, R. W. Knighton, and J. Carroll, "Revealing Henle's fiber layer using spectral domain optical coherence tomography," *Investigative Ophthalmology & Visual Science*, vol. 52, no. 3, pp. 1486–1492, 2011.
- [114] M. Chen, A. Lang, H. S. Ying, P. A. Calabresi, J. L. Prince, and A. Carass, "Analysis of macular OCT images using deformable registration," *Biomedical Optics Express*, vol. 5, no. 7, pp. 2196–2214, 2014.
- [115] C. Confavreux, S. Vukusic, T. Moreau, and P. Adeleine, "Relapses and progression of disability in multiple sclerosis," *New England Journal of Medicine*, vol. 343, no. 20, pp. 1430–1438, 2000.
- [116] N. S. Namerow, "Somatosensory evoked responses in multiple sclerosis patients with varying sensory loss," *Neurology*, vol. 18, no. 12, pp. 1197–1197, 1968.

- [117] S. M. Rao, T. A. Hammeke, M. P. McQuillen, B. Khatri, and D. Lloyd, "Memory disturbance in chronic progressive multiple sclerosis," *Archives of Neurology*, vol. 41, no. 6, pp. 625–631, 1984.
- [118] S. M. Rao, G. J. Leo, L. Bernardin, and F. Unverzagt, "Cognitive dysfunction in multiple sclerosis I: Frequency, patterns, and prediction," *Neurology*, vol. 41, no. 5, pp. 685–691, 1991.
- [119] R. H. Hashemi, W. G. Bradley Jr, D.-Y. Chen, J. E. Jordan, J. A. Queralt, A. E. Cheng, and J. N. Henrie, "Suspected multiple sclerosis: MR imaging with a thin-section fast FLAIR pulse sequence," *Radiology*, vol. 196, no. 2, pp. 505–510, 1995.
- [120] E. M. Haacke, M. Makki, Y. Ge, M. Maheshwari, V. Sehgal, J. Hu, M. Selvan, Z. Wu, Z. Latif, Y. Xuan *et al.*, "Characterizing iron deposition in multiple sclerosis lesions using susceptibility weighted imaging," *Journal of Magnetic Resonance Imaging*, vol. 29, no. 3, pp. 537–544, 2009.
- [121] M. Filippi, M. A. Rocca, G. Martino, M. A. Horsfield, and G. Comi, "Magnetization transfer changes in the normal appearing white matter precede the appearance of enhancing lesions in patients with multiple sclerosis," *Annals of Neurology*, vol. 43, no. 6, pp. 809–814, 1998.
- [122] H.-J. Park, M. Kubicki, M. E. Shenton, A. Guimond, R. W. McCarley, S. E. Maier, R. Kikinis, F. A. Jolesz, and C.-F. Westin, "Spatial normalization of diffusion tensor MRI using multiple channels," *NeuroImage*, vol. 20, no. 4, pp. 1995–2009, 2003.
- [123] G. K. Rohde, S. Pajevic, C. Pierpaoli, and P. J. Basser, "A comprehensive approach for multi-channel image registration," in *2nd International Workshop on Biomedical Image Registration*, 2003, pp. 214–223.
- [124] B. Avants, J. T. Duda, H. Zhang, and J. C. Gee, "Multivariate normalization with symmetric diffeomorphisms for multivariate studies," in *Medical Image Computing and Computer-Assisted Intervention–MICCAI 2007*, 2007, pp. 359–366.
- [125] D. Forsberg, Y. Rathi, S. Bouix, D. Wassermann, H. Knutsson, and C.-F. Westin, "Improving registration using multi-channel diffeomorphic demons combined with certainty maps," in *Multimodal Brain Image Analysis–MBIA 2011*, 2011, pp. 19–26.
- [126] A. S. Choe, Y. Gao, X. Li, K. B. Compton, I. Stepniewska, and A. W. Anderson, "Accuracy of image registration between MRI and light microscopy in the ex vivo brain," *Magnetic Resonance Imaging*, vol. 29, no. 5, pp. 683–692, 2011.
- [127] J. H. Noble and B. M. Dawant, "Automatic segmentation of the optic nerves and chiasm in CT and MR using the atlas-navigated optimal medial axis and deformable-model algorithm," in *Proceedings of SPIE Medical Imaging 2009*, 2009, p. 725916.

- [128] X. Li, T. E. Yankeelov, G. D. Rosen, J. C. Gore, and B. M. Dawant, "Enhancement of histological volumes through averaging and their use for the analysis of magnetic resonance images," *Magnetic Resonance Imaging*, vol. 27, no. 3, pp. 401–416, 2009.
- [129] C. A. Cocosco, V. Kollokian, R. K.-S. Kwan, G. B. Pike, and A. C. Evans, "BrainWeb: Online interface to a 3D MRI simulated brain database," in *NeuroImage*, vol. 5, no. 4, 1997, p. S425.
- [130] A. Carass, M. B. Wheeler, J. Cuzzocreo, P.-L. Bazin, S. S. Bassett, and J. L. Prince, "A joint registration and segmentation approach to skull stripping," in *Biomedical Imaging: From Nano to Macro, 4th IEEE International Symposium on*, 2007, pp. 656–659.
- [131] B. Likar and F. Pernuš, "A hierarchical approach to elastic registration based on mutual information," *Image and Vision Computing*, vol. 19, no. 1, pp. 33–44, 2001.
- [132] F. Maes, A. Collignon, D. Vandermeulen, G. Marchal, and P. Suetens, "Multimodality image registration by maximization of mutual information," *Medical Imaging, IEEE Transactions on*, vol. 16, no. 2, pp. 187–198, 1997.
- [133] A. Jog, S. Roy, A. Carass, and J. L. Prince, "Magnetic resonance image synthesis through patch regression," in *Biomedical Imaging: From Nano to Macro, 10th IEEE International Symposium on*, 2013, pp. 350–353.
- [134] W. Wein, S. Brunke, A. Khamene, M. R. Callstrom, and N. Navab, "Automatic CT-ultrasound registration for diagnostic imaging and image-guided intervention," *Medical Image Analysis*, vol. 12, no. 5, pp. 577–585, 2008.
- [135] F. Michel and N. Paragios, "Image transport regression using mixture of experts and discrete Markov random fields," in *Biomedical Imaging: From Nano to Macro, 7th IEEE International Symposium on*, 2010, pp. 1229–1232.
- [136] B. A. Landman, A. J. Huang, A. Gifford, D. S. Vikram, I. A. L. Lim, J. A. Farrell, J. A. Bogovic, J. Hua, M. Chen, S. Jarso *et al.*, "Multi-parametric neuroimaging reproducibility: A 3-T resource study," *NeuroImage*, vol. 54, no. 4, pp. 2854–2866, 2011.
- [137] M. Chen, A. Carass, J. Bogovic, P.-L. Bazin, and J. L. Prince, "Distance transforms in multi channel MR image registration," in *Proceedings of SPIE Medical Imaging 2011*, 2011, p. 79621D.
- [138] M. Chen, A. Jog, A. Carass, and J. L. Prince, "Using image synthesis for multi-channel registration of different image modalities," in *Proceedings of SPIE Medical Imaging 2015*, 2015, p. To Appear.
- [139] A. Prinster, M. Quarantelli, G. Orefice, R. Lanzillo, A. Brunetti, C. Mollica, E. Salvatore, V. Morra, G. Coppola, G. Vacca *et al.*, "Grey matter loss in relapsing–remitting multiple sclerosis: A voxel-based morphometry study," *NeuroImage*, vol. 29, no. 3, pp. 859–867, 2006.

- [140] J. Sepulcre, J. Sastre-Garriga, M. Cercignani, G. T. Ingle, D. H. Miller, and A. J. Thompson, "Regional gray matter atrophy in early primary progressive multiple sclerosis: A voxel-based morphometry study," *Archives of Neurology*, vol. 63, no. 8, pp. 1175–1180, 2006.
- [141] G. Ettinger, W. Grimson, T. Lozano-Perez, W. Wells III, S. White, and R. Kikinis, "Automatic registration for multiple sclerosis change detection," in *Biomedical Image Analysis, Proceedings of the IEEE Workshop on*, 1994, pp. 297–306.

# Vita

Min Chen was born on June 22nd, 1986 in Nanjing, China. In 1993, he move to Logan UT, USA where he completed his primary and secondary education. After graduating from Logan High School in 2004, he attended Cornell University where he completed his Bachelor of Science in Electrical and Computer Engineering in 2008. From 2008 until 2015, he was enrolled as a graduate student at Johns Hopkins University, where he did research on medical image analysis and image registration under the advisement of Dr. Jerry L. Prince at the Image Analysis and Communications Laboratory. In 2012, he completed his Masters of Engineering in Electrical and Computer Engineering. He defended this dissertation on December 9th, 2014.